DETERMINING LOCALIZED ANODE CONDITION TO MAINTAIN EFFECTIVE CORROSION PROTECTION

Final Report

SPR 653

DETERMINING LOCALIZED ANODE CONDITION TO MAINTAIN EFFECTIVE CORROSION PROTECTION

Final Report

SPR 653

by

Vinh Nguyen, Graduate Research Assistant in Chemical Engineering
Josh Meuli, Research Assistant in Chemical Engineering
Bill Brooks, Graduate Research Assistant Chemical Engineering
Henri Jansen, Professor of Physics
John Westall, Professor of Chemistry
Milo Koretsky, Associate Professor of Chemical Engineering
Oregon State University

for

January 2010

Technical Report Documentation Page

1. Report No. FHWA-OR-RD-10-11	2. Government Accession No.	3. Recipient's Catalog No.
4. Title and Subtitle Determining Localized Anode Condition to Maintain Effective Corrosion Protection		5. Report Date January 2010
		6. Performing Organization Code
7. Author(s) Vinh Nguyen, Graduate Research Assistant in Chemical Engineering Josh Meuli, Research Assistant in Chemical Engineering Bill Brooks, Graduate Research Assistant Chemical Engineering Henri Jansen, Professor of Physics John Westall, Professor of Chemistry Milo Koretsky, Associate Professor of Chemical Engineering		8. Performing Organization Report No.
9. Performing Organization Name and Address School of Chemical, Biological & Environmental Engineering Oregon State University 103 Gleeson Hall Corvallis, OR 97331		10. Work Unit No. (TRAIS)
		11. Contract or Grant No. SPR 653
12. Sponsoring Agency Name and Address Oregon Department of Transportation Research Section and Federal Highway Administration 200 Hawthorne Ave. SE, Suite B-240 400 Seventh Street, SW Salem, OR 97301-5192 Washington, DC 20590-0003		13. Type of Report and Period Covered Final Report
		14. Sponsoring Agency Code

15. Supplementary Notes

16. Abstract

Thermal sprayed zinc anodes used for impressed current cathodic protection of reinforced concrete deteriorate over time. Two different technologies, ultrasound and electrical circuit resistance combined with water permeability, were investigated in the laboratory to determine whether they were feasible methods for estimating anode condition. The ultrasonic method was unable to detect a reflected acoustic signal from zinc-on-concrete specimens due to scattering of the signal within the samples. Circuit resistance was shown to increase with the electrochemical age of the specimens, but the resistance trend did not correlate with the bond strength trend at later ages. The aged specimens were fairly impermeable to water infiltration presumably due to build up of reaction products in the porosity. Consequently, a method of using resistance measurements combined with water infiltration to determine anode condition was not successful. It was shown that the permeability improved if the surface was mechanically perturbed such as creating a pin hole. Improving permeability by penetrating the surface could have ramifications for improving anode performance.

17. Key Words CATHODIC PROTECTION, ZINC, ANODE, ULTRASOUND, RESISTANCE, PERMEABILITY, CONCRETE	18. Distribution Statement Copies available from NTIS, and online at http://www.oregon.gov/ODOT/TD/TP_RES/		
19. Security Classification (of this report) Unclassified	20. Security Classification (of this page) Unclassified	21. No. of Pages 100 + appendices	22. Price

Technical Report Form DOT F 1700.7 (8-72)   Reproduction of completed page authorized   ♻ Printed on recycled paper

i

SI* (MODERN METRIC) CONVERSION FACTORS

APPROXIMATE CONVERSIONS TO SI UNITS

Symbol	When You Know	Multiply By	To Find	Symbol
		LENGTH		
in	inches	25.4	millimeters	mm
ft	feet	0.305	meters	m
yd	yards	0.914	meters	m
mi	miles	1.61	kilometers	km
		AREA		
in^2	square inches	645.2	millimeters squared	mm^2
ft^2	square feet	0.093	meters squared	m^2
yd^2	square yards	0.836	meters squared	m^2
ac	acres	0.405	hectares	ha
mi^2	square miles	2.59	kilometers squared	km^2
		VOLUME		
fl oz	fluid ounces	29.57	milliliters	ml
gal	gallons	3.785	liters	L
ft^3	cubic feet	0.028	meters cubed	m^3
yd^3	cubic yards	0.765	meters cubed	m^3
	NOTE: Volumes greater than 1000 L shall be shown in m^3.			
		MASS		
oz	ounces	28.35	grams	g
lb	pounds	0.454	kilograms	kg
T	short tons (2000 lb)	0.907	megagrams	Mg
		TEMPERATURE (exact)		
°F	Fahrenheit	(F-32)/1.8	Celsius	°C

APPROXIMATE CONVERSIONS FROM SI UNITS

Symbol	When You Know	Multiply By	To Find	Symbol
		LENGTH		
mm	millimeters	0.039	inches	in
m	meters	3.28	feet	ft
m	meters	1.09	yards	yd
km	kilometers	0.621	miles	mi
		AREA		
mm^2	millimeters squared	0.0016	square inches	in^2
m^2	meters squared	10.764	square feet	ft^2
m^2	meters squared	1.196	square yards	yd^2
ha	hectares	2.47	acres	ac
km^2	kilometers squared	0.386	square miles	mi^2
		VOLUME		
ml	milliliters	0.034	fluid ounces	fl oz
L	liters	0.264	gallons	gal
m^3	meters cubed	35.315	cubic feet	ft^3
m^3	meters cubed	1.308	cubic yards	yd^3
		MASS		
g	grams	0.035	ounces	oz
kg	kilograms	2.205	pounds	lb
Mg	megagrams	1.102	short tons (2000 lb)	T
		TEMPERATURE (exact)		
°C	Celsius	1.8C+32	Fahrenheit	°F

*SI is the symbol for the International System of Measurement

ii

ACKNOWLEDGEMENTS

DISCLAIMER

This document is disseminated under the sponsorship of the Oregon Department of Transportation and the United States Department of Transportation in the interest of information exchange. The State of Oregon and the United States Government assume no liability of its contents or use thereof.

The contents of this report reflect the view of the authors who are solely responsible for the facts and accuracy of the material presented. The contents do not necessarily reflect the official views of the Oregon Department of Transportation or the United States Department of Transportation.

The State of Oregon and the United States Government do not endorse products of manufacturers. Trademarks or manufacturers' names appear herein only because they are considered essential to the object of this document.

This report does not constitute a standard, specification, or regulation.

EXECUTIVE SUMMARY

The main objective of this research project was to develop a prototype device that can determine the condition of the thermal sprayed zinc anode in cathodic protection (CP) systems installed on Oregon bridges. The device needs to meet the following requirements: applicability in the field, non-destructiveness or minimal destructiveness of the zinc anode, ease of use with little to no technical background, and the ability to determine anode condition. Two different technologies, ultrasound and resistance/permeability, were explored to examine their potential in determining the localized anode condition.

Ultrasound testing was performed on three different sets of samples. Analysis using time-of-flight was able to determine the thicknesses of the zinc sheet samples. Calculated thicknesses were essentially identical to the nominal thicknesses. Similar analysis resulted in negative results when applied to electrochemically aged and unaged samples. It is believed that the ultrasonic waves were being scattered by the roughness at the zinc/concrete interface or, perhaps, in the bulk of the thermal sprayed zinc. An alternative ultrasonic configuration using surface (Lamb) waves was recommended for future studies.

Cyclic voltammetry was used to measure the resistance of the electrochemically aged samples. Dry resistance measurements were performed on five different electrochemically aged blocks. It was determined that the average resistance of the blocks increased rapidly up to approximately 5 bridge years, generally corresponding to the maximum bond strength; beyond this point the resistance then gradually increased or leveled off. Individual resistance data was seen to vary with time, but changes were consistent from block to block. The resistance was shown to be inversely related to temperature, and investigators believed it was affected by environmental factors. Open circuit potential showed less variation with time when compared to the resistance measurements. Using a three-electrode configuration, the potential of zinc generally tracked the resistance and bond strength measurements, while the potential of iron increased with age.

No dynamic changes in resistance were noticed with the addition of water. It is believed that the water was impeded due to lack of permeability in the samples. A noticeable decrease in resistance was observed when the water had a path to the zinc/concrete interface, either by a pin hole or bare concrete adjacent to the zinc. It was recommended that a simple field test be developed to monitor the response of a CP system for an applied voltage as a zone is sprayed with water, and that such a test may be aided by systematic creation of pin holes in the thermal sprayed zinc anode. It was also recommended that the created pin holes be studied in an accelerated aging environment. Preliminary data from this study suggest that not only will the creation of pin holes assist in characterization of anode condition through electrical response, but it may also increase the service life of the zinc anode by decreasing the circuit resistance of the electrochemical cell.

DETERMINING LOCALIZED ANODE CONDITION TO MAINTAIN EFFECTIVE CORROSION PROTECTION

TABLE OF CONTENTS

List of Figures

List of Tables

1.0   INTRODUCTION

The corrosion of steel in coastal reinforced concrete bridges is an ongoing problem. In Oregon alone there are over 120 coastal bridges. Most of these bridges are reinforced concrete structures. Due to the coastal environment, bridges are very susceptible to corrosion. As the reinforcing steel corrodes, a buildup of iron oxides (rust) accumulates on the surface of the reinforcing steel, which can lead to an increase in tensile force in the concrete. The force can become great enough to cause the concrete to spall, exposing the reinforcing steel to further corrosion. Figure 1.1 shows an example of reinforcing steel being exposed to the atmosphere due to spalling.

Impressed current cathodic protection (CP) is a common method to reduce corrosion of reinforcing steel in concrete structures. By reducing the corrosion rate of steel in the reinforced concrete structure, the service life can be extended. The Oregon Department of Transportation (ODOT) has been implementing impressed current CP systems on coastal bridges since 1991. Table 1.1 lists several impressed current CP systems in progress or completed by ODOT. CP is the only approach that has been proven to mitigate corrosion in high-chloride environments .

CP systems use metallic anodes that effectively distribute the current to the reinforcing steel. The majority of the CP systems on Oregon's coastal bridges use thermal-sprayed (TS) zinc. The service life of the of the zinc anode can be estimated by its consumption as it oxidizes; the system life is designed to be around 25 years. However, processes such as delamination can cause these systems to prematurely cease being effective (*Covino, et al. 2002*). This report discusses the investigation of possible technologies that may be applied in the field to determine the condition of the TS zinc anode with little to no damage to the CP system.

Figure 1.1: Accumulation of corrosion products at the surface of the reinforcing steel have caused the concrete to spall, exposing the reinforcing steel to further corrosion. This picture was taken at Big Creek Bridge prior to restoration (*Covino, et al. 2002*).

Table 1.1: Oregon DOT conductive coating anode impressed current CP projects (*ODOT 2009*)

Bridge	Year energized	Total Cost of CP System	Area, m^2 (ft^2)	Anode Material	Thickness, mm (mils)
Cape Creek	1991	$1,787,782	9,530 (102,500)	TS Zn	0.51 (20)
Yaquina Bay	1994	$8,815,613	16,215 (174,548)	TS Zn	0.50 (20)
Depoe Bay	1995	$3,073,155	5,940 (63,960)	TS Zn	0.55 (21.7)
Cape Perpetua	1997	$155,960	114 (1,227)	TS AlZnIn, Zn hydrogel	0.40 (15.8), 0.25 (10)
Big Creek	1998	$1,478,153	1,865 (20,026)	TS Zn	0.38 (15)
Cummins Creek	2001	$1,208,365	1,865 (20,000)	TS Zn	0.38 (15)
Rocky Creek	2001	$2,549,529	3,700 (40,000)	TS Zn	0.38 (15)
Rogue River	2003	$11,137,280	33,000 (350,000)	TS Zn	0.38 (15)
Tenmile Creek	2007	$2,019,975	1,372 (14,769)	TS Zn	0.38 (15)
Coos Bay	2010	$19,389,888	24,406 (263,676)	TS Zn	0.38 (15)

1.1 BACKGROUND

Reinforcing steel does not typically corrode in environments with a high pH. During the hydration process, a highly alkaline pore solution develops within cement with a pH between 12 and 13 (*Aziz and Mansur 1983*). Figure 1.2 shows the Pourbaix diagram for Fe-H_2O (*Ahmad 2006*). The diagram depicts the stable forms of iron as a function of pH and electrical potential of the steel. At high pH, this environment is thermodynamically stable for iron oxides and oxyhydroxides. Anodic reactions form a thin protective passive iron oxide film (*Hime and Erlin 1987*):

$$3Fe + 4H_2O \rightarrow Fe_3O_4 + 8H^+ + 8e^- \tag{1-1}$$

$$2Fe_3O_4 + H_2O \rightarrow 3Fe_2O_3 + 2H^+ + 2e^- \tag{1-2}$$
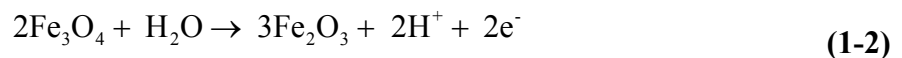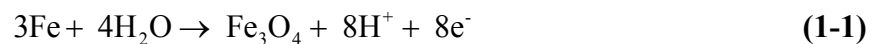
The corrosion of a reinforced structure can be separated into two distinct phases. The first phase is considered the onset of corrosion, in which the passive film is still present but can be broken down by chloride contamination or carbonation of the concrete. The second phase is propagation of corrosion, in which the passive film has been completely broken down and the reinforced steel actively corrodes.

 The overall corrosion of steel can be generically summarized by the following reaction:

$$iron + oxygen + water \rightarrow corrosion\ products \tag{1-3}$$
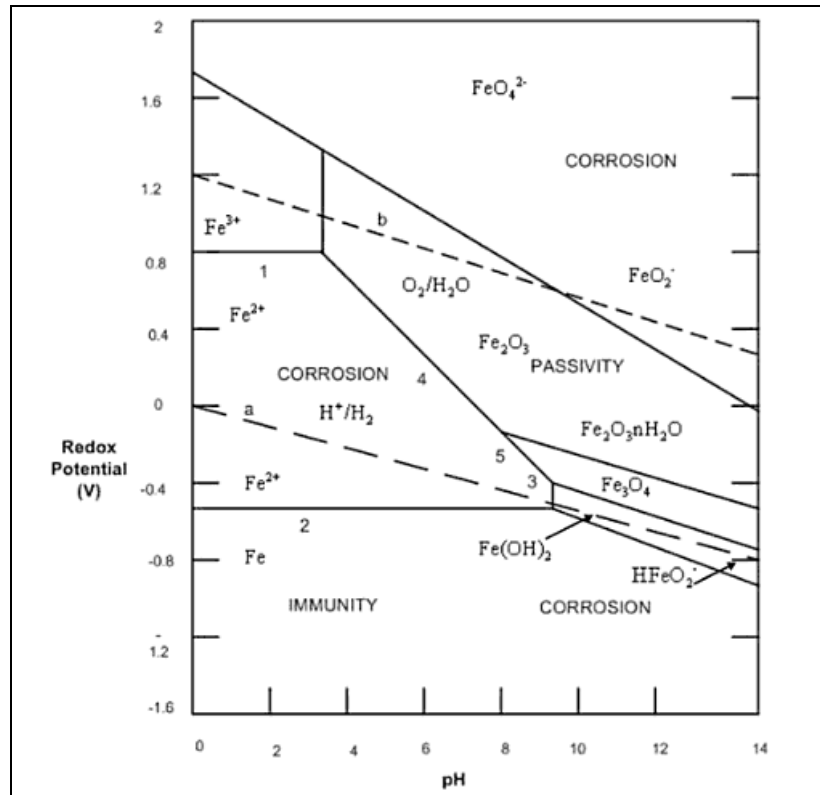
Figure 1.2: Pourbaix diagram for Fe-H$_2$0 (*Ahmad 2006*)

Contamination of chloride ions in reinforced steel structures is a frequent cause of the onset of corrosion. There are now design codes for reinforced concrete structures that regulate the amount of chloride that may be introduced from raw materials containing significant amounts of chlorides. In Europe the maximum allowed chloride content is 0.2-0.4% chloride ions by mass (*Bertolini, et al. 2004*). In the past, chloride ions have been added into the concrete mix, unknowingly or deliberately, through contaminated mixing water, aggregates, or admixtures. Concrete surfaces can also be exposed to chloride ions from external sources, such as de-icing salts applied to the concrete surface and salt water from a marine environment (*Bertolini, et al. 2004; Daily 1997; Hobbs 1996*).

Chloride ions then enter the concrete by a number of mechanisms such as diffusion, capillary suction under wetting and drying cycles, under a hydrostatic head, and through cracks or defective joints (*Hobbs 1996*). The pH of the concrete is lowered as the chloride ions travel through the concrete pores to the reinforcing steel. Corrosion commences when the concentration of chloride ions at the steel surface reaches a threshold value. Structures that are exposed to the atmosphere need relatively low levels of chloride ions to initiate corrosion. Corrosion occurs because there is an abundance of oxygen that can diffuse through the concrete to react at the steel surface. Higher concentrations of chloride ions are needed in areas that are submerged in sea water or areas where the concrete is saturated with water. The saturation of water hinders the supply of oxygen (*Bertolini, et al. 2004*).

3

It has been shown in field experience and research that a threshold chloride ion concentration of about 0.026%, by weight of concrete, is sufficient to break down the passive film on existing structures (*Daily 1997*). Once the passive film is removed, the reinforcing steel is susceptible to oxidation (*Koretsky, et al. 1999*):

$$Fe \rightleftharpoons Fe^{2+} + 2e^- \qquad \text{(1-4)}$$

The electrons formed by the anodic reaction above flow to cathodic sites, where the passive film may be still intact, and react with water and oxygen in the reduction reaction:

$$\frac{1}{2}O_2 + H_2O + 2e^- \rightleftharpoons 2(OH^-) \qquad \text{(1-5)}$$
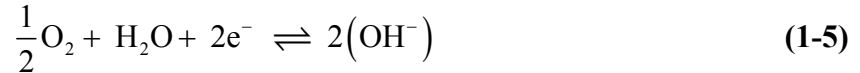
The charged ions formed in the oxidation and reduction reactions can further react to form iron products as follows (*Popovics, et al. 1983*):

$$Fe^{2+} + 2(OH^-) \rightarrow Fe(OH)_2 \qquad \text{(1-6)}$$

$$4Fe(OH)_2 + O_2 + 2H_2O \rightarrow 4Fe(OH)_3 \qquad \text{(1-7)}$$
$$\text{Red Rust}$$

$$3Fe + 8(OH^-) \rightarrow 4H_2O + Fe_3O_4 + 8e^- \qquad \text{(1-8)}$$
$$\text{Black Rust}$$
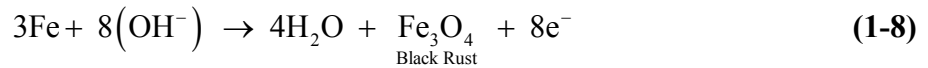
These reactions lead to a decrease in the alkalinity of the concrete adjacent to the steel. As a result the environment surrounding the reinforced steel becomes increasingly reactive and more susceptible to corrosion.

Cathodic protection of steel reinforcement is a widely utilized technique in the prevention of corrosion in concrete structures. An impressed current CP system uses an external DC current source to electrically connect a sacrificial anode to the steel reinforcement. By applying an external negative potential to the reinforcing steel, the corrosion rate decreases. As the Pourbaix diagram in Figure 1.2 illustrates, at largely negative potential the metallic phase is the more thermodynamically favorable state of iron.

Once a CP system is energized, corrosion protection for the reinforced concrete structure begins. The negative potential repels chloride ions away from the reinforced steel. Additionally, the production of hydroxyl ion creates a more alkaline environment. The pH of the concrete adjacent to the steel can increase from a value of 9 to values higher then 12, repassivating the steel (*Bertolini, et al. 2003; Mudd, et al. 1988*). If the applied potential is not large enough in magnitude, the reinforced steel is insufficiently protected. If the applied potential is too large in magnitude, the excessive current decreases the service of life of the zinc anode (*Muehlenkamp, et al. 2005*).

Examples of sacrificial anodes include the following: conductive graphite paint, catalyzed titanium, conductive polymeric wire, magnesium, aluminum, zinc/aluminum alloy, and most

commonly, zinc (*Mudd, et al. 1988; Panossian, et al. 2005; Bertolini, et al. 2003*). Thermal-sprayed (TS) zinc is commonly used by ODOT in CP systems (Table 1.1). Zinc (Zn) is a good choice for an anode material because it has a lower reduction potential than iron and because it is inexpensive and readily available. In addition it can be vaporized and sprayed to obtain a coating that adheres well to concrete. A twin wire arc process method is used to deposit the zinc anode on the surface of the concrete. This process uses an arc to melt two zinc wires. The molten zinc droplets are sprayed onto the rough concrete surface by compressed air. TS zinc does not form an oxide skin between drops, but it does leave scattered voids (*Covino, et al. 1996; Covino, et al. 2002*). TS Zn anodes can be installed on new structures as well as existing structures already affected by corrosion.

A schematic of the processes occurring in sprayed Zn CP systems is illustrated in Figure 1.3. The negative terminal of the power source is connected to the rebar and the positive side to the sprayed zinc anode. The circuit is completed by the flow of ions within the pores of the concrete. Negatively charged chloride and hydroxide ions are attracted to the zinc anode, and positively charged sodium and calcium ions are attracted to the steel cathode (*Muehlenkamp, et al. 2005*). Water and oxygen diffuse through the pores in the concrete.
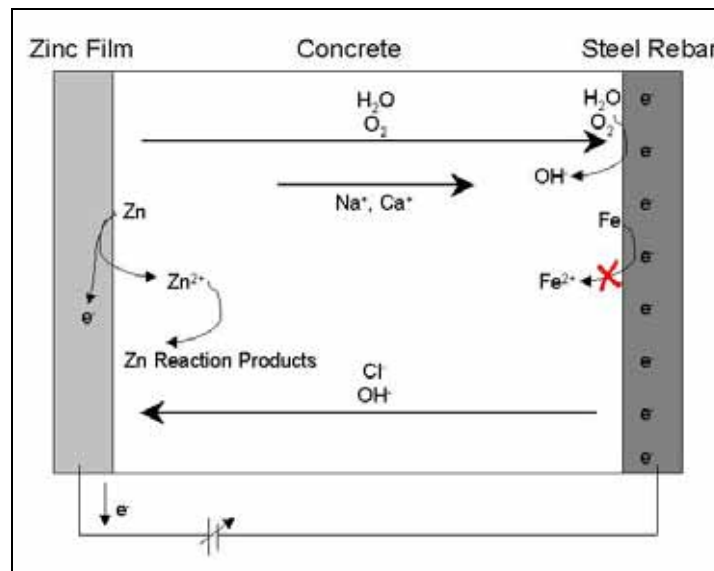
Figure 1.3: Schematic of CP system showing electrode reactions and ionic diffusion processes

In these CP systems, zinc provides an alternative path for Reaction 1.4 by undergoing an oxidation reaction to zincate in preference to iron (*Koretsky, et al. 1999*):

$$Zn \rightleftharpoons Zn^{2+} + 2e^- \qquad\qquad \textbf{(1-9)}$$

With time, the concentration of zincate increases in the pore solution adjacent to the anode-concrete interface and eventually reaches saturation. The zincate can transport into the concrete pores and undergo further reactions. Since the pH of concrete is very high (~12.0), various hydrated zinc hydroxides are formed:

$$Zn^{2+} + 2H_2O \rightarrow Zn(OH)_2 + 2H^+ \qquad \textbf{(1-10)}$$
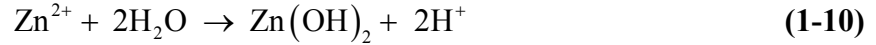
These species are not very soluble. During drying cycles, zinc hydroxides can dehydrate to form zinc oxide:

$$Zn(OH)_2 \rightarrow ZnO + H_2O \qquad \textbf{(1-11)}$$

Zincate ions can also react with other ligands that come from the pore solution such as chloride, sulfate or carbonate ions. These products can then further react with the complex minerals in the cement paste in secondary mineralization reactions (*Brousseau, et al. 1995; Covino, et al. 2002*). With "aging" of the TS Zn CP system, the interface between the sprayed metal coating and the concrete slowly accumulates a pasty layer consisting mostly of zinc oxides, hydroxides, and silicates. This layer is termed the zinc product layer, ZPL. The electrical resistance in these systems is commonly seen to increase with time (*Brousseau, et al. 1995; Covino, et al. 2002; Whiting, et al. 1996*); this increase has been attributed to processes occurring at the zinc-concrete interface.

The effect of accelerated electrochemical aging on the interfacial chemistry in the ZPL has been studied by Covino, et al. (*2002*). They report that three distinct layers or zones are formed within the ZPL. The major compounds are shown in Table 1.2, but other compounds may exist in smaller concentrations. These zones appear at different times over the lifespan of the anode and grow at different rates, as shown in Table 1.3. An SEM image of these zones is shown in Figure 1.4.

Table 1.2: TS Zn anode-concrete interfacial chemistry.
Reproduced from Covino, et al. (*2002*)

Location	Characteristics	Possible Compounds
Zn coating	metallic Zn	Zn
Zone 1	O/Zn ratio 1.4 enriched in Cl, S	ZnO $Zn(OH)_2$ $ZnSO_4$ $ZnCl_2$
Zone 2	O/Zn ratio 2.4 enriched in Cl, S substantial Si	(Ca,Zn)silicate (Ca,Zn)aluminate $ZnSO_4$ $ZnCl_2$
Zone 3	O/Zn ratio 7.5 elevated Cl increased Ca	(Ca, Zn)silicate (Ca,Zn)aluminate $ZnCl_2$
Unaltered cement paste	high Ca low Cl, S no Zn	Ca silicate Ca aluminate

Table 1.3: Reaction zone thickness for TS anodes on periodically-wetted slabs. Reproduced from Covino, et al. (*2002*)

Electrochemical Age, y @0.0022 A/m^2	Zone width, mm		
	Zone 1	Zone 2	Zone 3
0.0	0.00	0.00	0.00
0.6	<0.02	0.00	0.00
1.2	<0.02	0.18	0.00
4.1	0.11	0.41	0.00
9.4	0.15	0.40	0.21
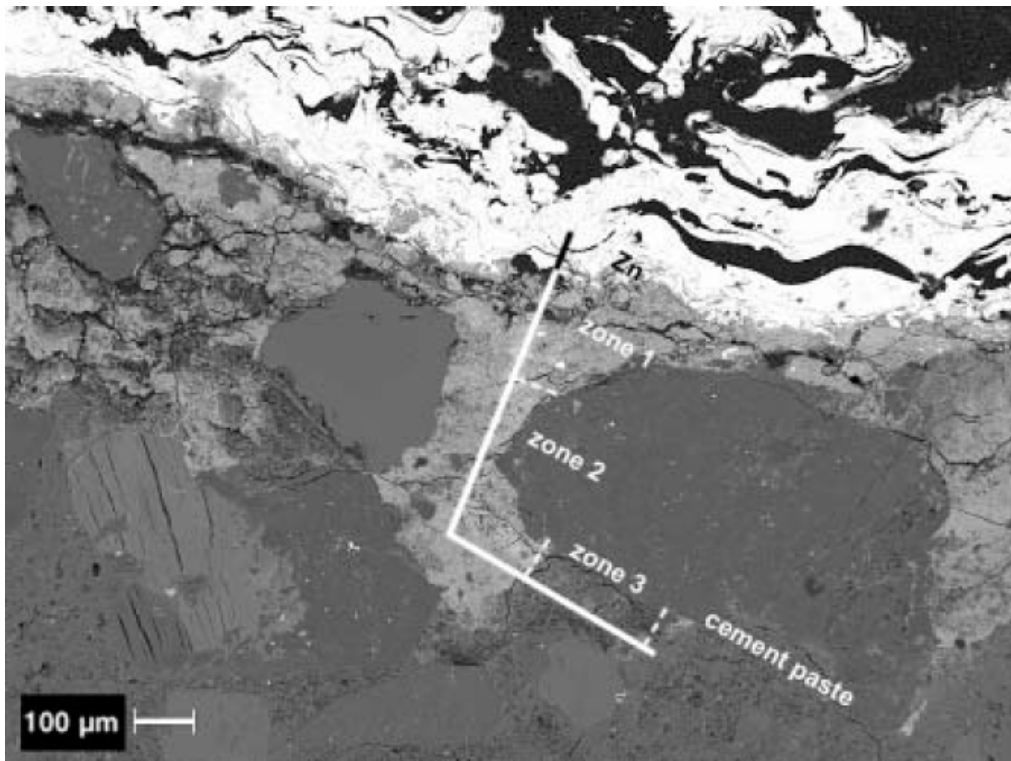
Figure 1.4: Back-scattered electron SEM photomicrograph of a cross-section of TS Zn anode on periodically-wetted concrete electrochemically aged for 640 kC/m^2, the equivalent of 9.4 years at 0.0022 A/m^2; shows reaction zones. Reproduced from Covino, et al. (*2002*).

Zone 1 consists primarily of products of electrochemical reactions of the metallic Zn. Most of these products are water-soluble. Zone 1 is the weak layer, with high concentrations of ZnO and Zn(OH)$_2$, which typically cracks in the plane parallel to the Zn anode. Compounds in zone 2 are less soluble in water than those in zone 1 and consist mainly of zinc silicates and aluminates. These compounds are formed by secondary mineralization when Zn^{2+} replaces the Ca^{2+} in the

silicates and aluminates from the cement paste. This process is limited by the slow diffusion of Zn^{2+} though the cement paste. Zone 3 is made up largely of zinc silicate and aluminates with a lower concentration of $ZnCl_2$. Zone 3 also has a greater concentration of calcium due to the excess Ca from zone 2 leaching into zone 3 (*Covino, et al. 2002*). This layer is rather insoluble in water and is the main cause of the lack of fluid permeability in samples that are electrochemically aged longer.

The relation between permeability and electrochemical age is shown in Figure 1.5a. At 312 kC/m^2 the water permeability is very close to zero. This value of charge passed (312 kC/m^2) is very near the maximum bond strength as shown in Figure 1.5b. Therefore, it can be deduced that for the duration of decreasing bond strength there is limited water permeability.
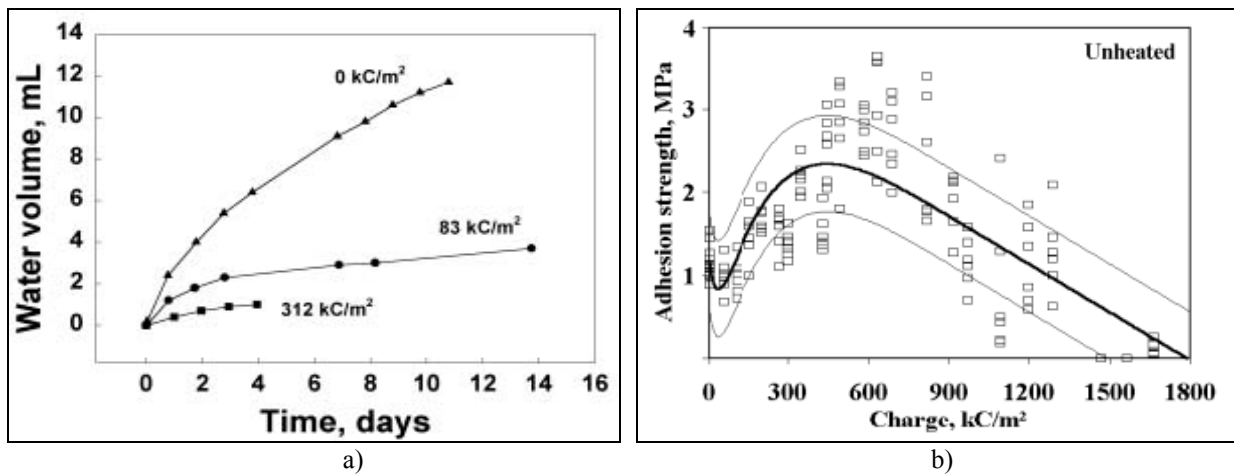
Figure 1.5: a) Permeability of water through TS Zn anode on periodically-wetted concrete slabs as a function of electrochemical age (permeability measurements are taken from the initial slope of the curves to represent unsaturated flow); b) Bond strength of the TS Zn anode on periodically-wetted, unheated concrete slabs versus electrochemical age. Reproduced from Covino, et al. (*2002*).

The distinct boundary between zone 3 and the cement paste suggests that the flux of Zn2+ or Ca2+ across this boundary is low (Covino, et al. 2002). The diffusion and migration of Zn2+ and Ca2+ cations and/or the diffusion of aluminate and silicate anions are needed to react and form zone 2. Since zone 3 is mostly insoluble in water, as the thickness of this zone increases and approaches a critical thickness, the transport of ions through zone 3 will essentially stop. Without the supply of anions, the reaction rate of zone 2 will dramatically decrease and eventually stop. It can be assumed that, at the point the diffusion of reactants becomes negligible, the fluid permeability has declined to zero, suggesting that the growth of zone 2 and 3 has essentially stopped by the time the bond strength has started decreasing.

These explanations are further supported by the pH trend at the zinc concrete interface, shown in Figure 1.6. The figure shows a noticeable decrease in pH up to an age of about 475 kC/m^2, approximately the age of maximum bond strength, and an approximately constant pH thereafter. This drop in pH would be expected from the formation of zinc hydroxides in zone 1.

8
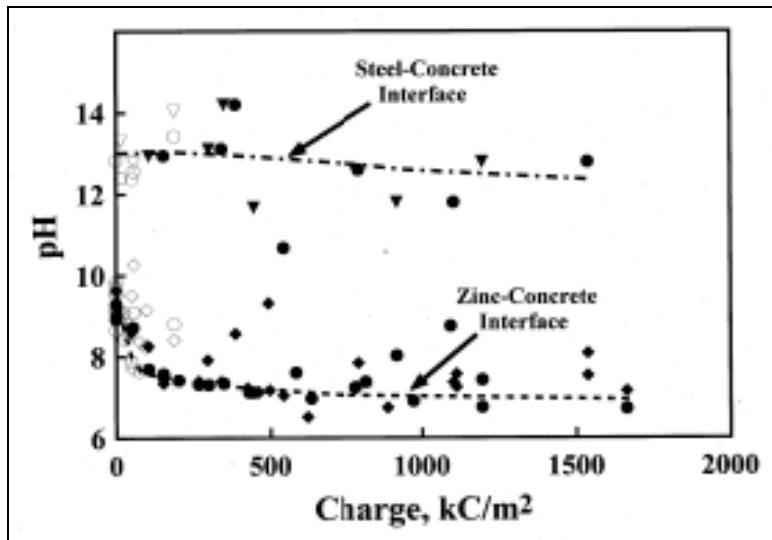
Figure 1.6: pH versus electrochemical age for TS Zn anode-concrete and steel-concrete interfaces for periodically-wetted concrete slabs. Reproduced from Covino, et al. (*2002*).

These trends in the data suggest that the loss of bond strength comes mainly from the increase in zone 1 thickness and the cracking of this layer parallel to the anode coating. Although the volume between the zinc and concrete increases from the growth of zones 2 and 3 and causes some decrease in bond strength, this effect is secondary.

The bond strength trend of un-wetted electrochemically aged slabs, which is shown in Figure 1.7a, also fits this model. Due to the lack of wetting and secondary mineralization, there is very little formation of zones 2 and 3. There is also an increased rate of formation of zone 1, since the compounds are not being dissolved and washed away or reacted into zone 2. This increased rate of bond strength degradation can be shown by the difference in the value of the slopes representing the adhesion strength after the maximum bond strength has been reached (Figure 1.7). The slope of the line on the decreasing bond strength portion for the periodically-wetted slabs is approximately 2.2 Pa*m^2/C as compared to that for the un-wetted slabs of 9.2 Pa*m^2/C. The larger slope indicates a more rapid loss in bond strength, presumably from more rapid growth of zone 1 on the un-wetted slabs.

Analysis of all of these data suggests that zone 1 thickness measurements are the most promising indicators of local anode conditions. Zone 2 and 3 production decreases to a negligible value in the periodically wetted slabs and is low in the un-wetted slabs.
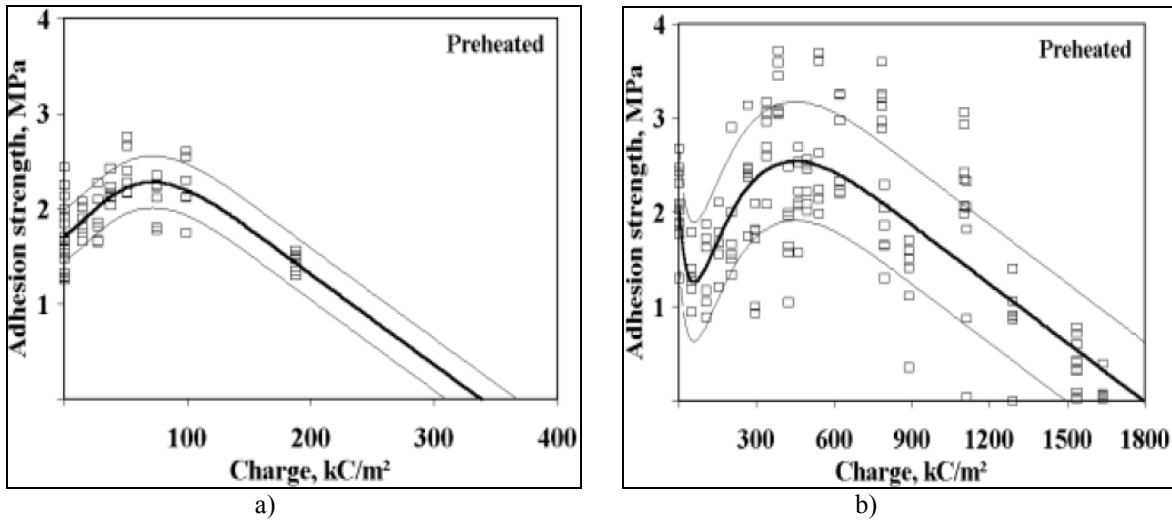
Figure 1.7: a) Bond strength of the TS Zn anode on un-wetted, preheated concrete slabs versus electrochemical age; b) Bond strength on periodically-wetted, preheated concrete slabs versus electrochemical age. Reproduced from Covino, et al. (*2002*).

Resistivity measurements have been reported using an AC measurement technique. This technique eliminates polarization effects commonly caused by DC measurements (*Covino, et al. 2002*). Figure 1.8a shows AC resistivity measurements of thermal sprayed Zn anodes aged for the equivalent of up to 20 bridge years at 0.0022A/m^2. The results indicate that the AC resistivity increases with the increase in age of the sample; however, there is considerable variability in these data. Figure 1.8b shows that the circuit resistance, in general, tracks AC resistance (*Holcomb, et al. 2002*). It has been shown that circuit resistance calculations can be used to track performance for a wide variety of CP systems, both in the laboratory and in the field, and it has been suggested that circuit resistance could be a good indication of the condition of the zinc-concrete interface (*Holcomb, et al. 2002*). In this project, we attempted to use the circuit resistance to track the condition of the interface; what we term "resistance" may be described in general electrochemical measurements as "polarization resistance".
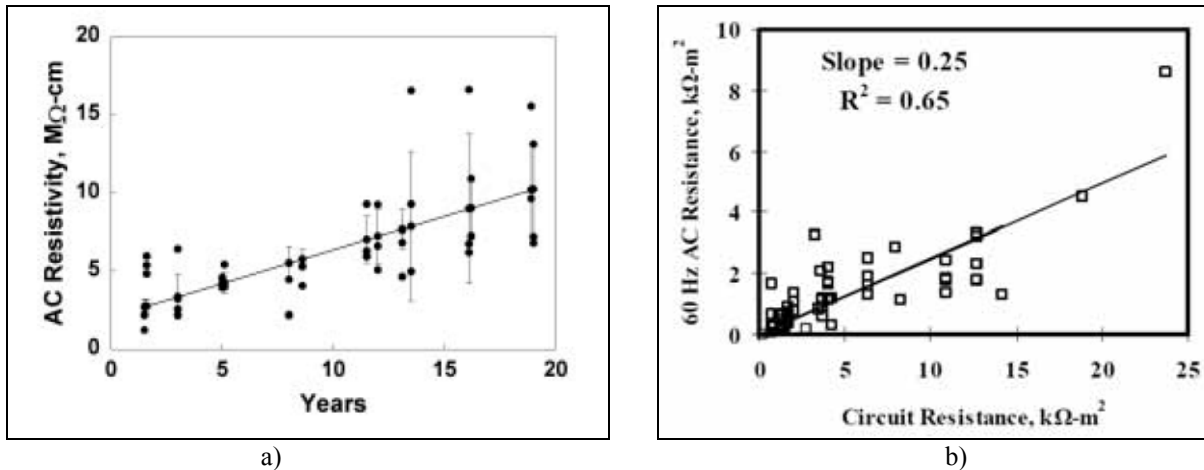
Figure 1.8: a) Volume average AC resistivity of material between the TS Zn anode and the steel as a function of electrochemical age in years at 0.0022 A/m^2 (*Covino, et al. 2002*); b) AC resistance compared with circuit resistance (*Holcomb, et al. 2002*)

Recent field studies were conducted at the Yaquina Bay Bridge in Newport, Oregon. Eight core samples were taken from CP zones and studied in detail using scanning electron microscopy, energy-dispersive X-ray analysis, image analysis, and X-ray diffraction to characterize the chemistry of the aged zinc anodes and determine the cause of delamination (*Cramer, et al. 2009*).

It was determined that the delamination was not due to the Zn anode being consumed. A 20 mil thick Zn anode operating at a current density of 2.2 mA/m^2 should last over 150 years. Although the Zn anode was installed at the same time and the same current density was used, the eight samples had a wide range of metallic zinc remaining. For the eight samples analyzed, the original amount of zinc ranged from 0 to 84% (*Cramer, et al. 2009*).

The chemistry of the thermal sprayed zinc from the eight core samples was similar to results obtained from the laboratory studies discussed above. It is believed that the Zn anode chemistry model is well understood. The analysis of the eight core samples contributed the following understanding of zinc oxidation chemistry: (1) the oxidation of zinc does not occur only at the zinc/concrete surface but within the anode itself; and (2) under local environmental conditions Zn does not always migrate into the cement paste, and Ca does not always migrate out of the cement paste.

1.2 PROBLEM DEFINITION

TS zinc anode CP systems have been applied or are being applied to bridges along the Oregon coast. The service life of the TS zinc anode is critically dependent on the environment of the bridge and the current density applied to the CP system. The service life has been estimated to be approximately 25 years, based on a specified current density of 2.2 mA/m^2; but a higher current density or drier conditions can significantly reduce the service life of the anode (*Covino, et al. 2002*). Delamination of the zinc anode is a significant problem.

The Yaquina Bay Bridge in Newport, Oregon, was first energized in 1994 with a TS zinc anode. In 2004-2005 inspectors and maintenance personnel noticed that there was an increase in delamination of the zinc anode on the Arches section (*Cramer, et al. 2006*). Figure 1.9 shows sections of the Yaquina Bay Bridge, on the south side of the bridge, that have almost completely delaminated. It can also be seen that different zones of TS zinc anode have started to delaminate, while other zones remain intact.

The condition of the anode is currently being measured by its bond strength to the concrete. The adhesion test is performed by attaching an aluminum dolly to the zinc anode and measuring the amount of forced required to detach the anode from the concrete. This method is destructive and leaves the location exposed to the environment.
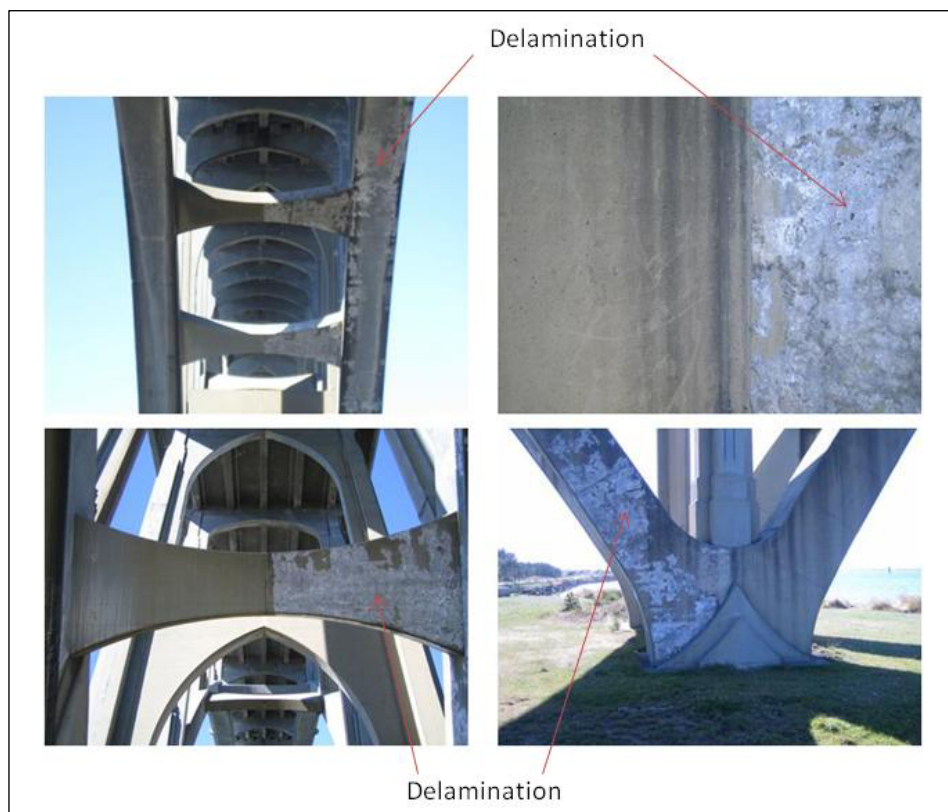
Figure 1.9: The Yaquina Bay Bridge showing the uneven condition of the TS zinc anode (photographs taken 10/10/06).

The goal of this project was to develop a different method to assess localized zinc anode conditions and time to delimitation in TS zinc anode CP systems. The criteria for this assessment included: applicability in the field, non-destructiveness or minimal destructiveness, ease of use, low cost of production, low development time, and ability to determine anode condition. The main objective of the research was to develop a non-destructive or minimally destructive method to provide information to assist ODOT in planning zinc anode repair and/or replacement.

2.0   TECHNOLOGY REVIEW AND WORK PLAN

2.1   SUMMARY OF TECHNOLOGIES CONSIDERED

The first task in the development of the prototype device was a broad review of the possible technologies to the assess the local zinc anode condition and time to delamination. This review of technologies consisted of a description of the fundamental operating principles, a comparison of the advantages and disadvantages, discussion of the devices that are commercially available (if applicable), and the modifications that would need to be made to available devices to meet the objectives of this project. Table 2.1 shows technologies that have been considered and the preliminary recommendation of the suitability for further investigation. The detailed consideration of each technology was presented as an interim report for this project and is summarized in Appendix A.

Table 2.1: Technologies considered and recommendations (for further detail see Appendix A)

Section	Technology	Recommendation
A.1	Fluid Permeability Testing	Not suitable
A.2	Resistance/Impedance	Not suitable
A.3	Near IR Testing	May be suitable
A.4	Acoustic Sensors	NA
A.5	Rebound Testing	Not suitable
A.6	Guided Wave Ultrasonic	Suitable
A.7	Bond Strength	Not suitable
A.8	pH Testing	Not suitable
A.9	Resistance/Permeability Hybrid Technology	May be suitable

The device must be capable of providing information that can assist ODOT in planning anode repair and replacement. The selection criteria, roughly in order of importance, include: ability to determine anode condition, applicability in the field, non-destructiveness of test, ease of use, low cost, and short time of development.

A summary of how each of the technology options are rated for the different criteria is shown in Table 2.2.

Table 2.2: Table of comparisons for technology options

Technologies	Criteria					
	Application in the Field	Non or Minimally Destructive	Ease of Use	Low Cost of Production	Development Time Low	Ability to Determine Anode Condition
Fluid Permeability Testing	√	+	+	√	√	-
Resistance/ Impedance	√	+	+	+	+	-
Near IR Testing	+	-	+	+	√	+
Rebound Testing	+	+	√	+	+	-
Guided Wave Ultrasonic	√	+	√	√	-	+
Bond Strength	+	-	-	+	+	√
pH Testing	√	-	√	+	+	-
Resistance/ Permeability	-	+	√	+	+	√

+ = Fits Criteria well
√ = Neither good nor bad fit
- = Fits Criteria Poorly

Ultrasonic wave testing (UT) was determined as the most likely candidate to provide a correlation between the measurements taken in the field and the local anode conditions. UT is also non-destructive and applicable in the field. More research and testing on UT, however, was necessary to determine the ability of this technology to analyze percent delamination and characterize the zinc product layer.

The resistance/permeability hybrid measuring technique showed complications for applicability in the field, while showing a promising outlook in the other categories. Determination of the resistance/permeability correlation to bond strength is obtainable in the lab setting, and must be considered useful before pursuing development of a more field use friendly prototype.

Although near-IR requires a destructive modification to the zinc anode, the destructiveness may be able to be minimized. Near-IR has a very good potential for full characterization of the local oxide layer and correlation to bond strength.

Therefore the near-IR, resistance/permeability, and the ultrasonic testing were the technology options that showed the most promise for further investigation. For the scope of this research, ultrasonic and then resistance/permeability testing were performed to determine the capabilities of each technology in determining the condition of the local zinc anode.

2.2   WORK PLAN SYNOPSIS

The ultrasonic wave experimental tests were conducted in a laboratory environment using the following materials: 1) electrochemically aged samples obtained from the National Energy Technology Laboratory (NETL) in Albany Oregon; 2) unaged samples of varying thickness sprayed by Great Western Cooperation; and 3) zinc sheet samples varying in thickness. Resistivity/permeability hybrid testing was pursued next. The project was conducted according to the decision tree in Figure 2.1. A brief description of the approach for each major technology follows.
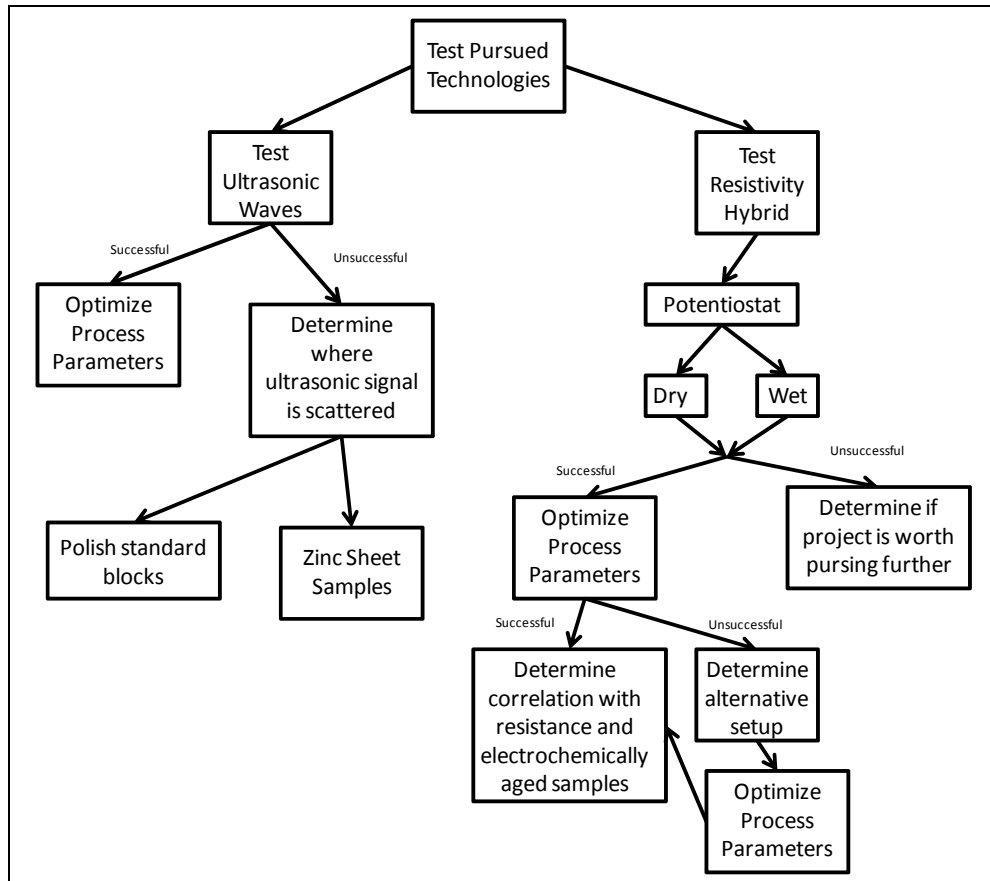
Figure 2.1: Decision tree for research plan on two technologies being pursued

2.2.1 Ultrasonic waves

Ultrasound is a widely used technique for inspecting different types of materials for defects. It has the capability of penetrating through most materials, allowing it to be used to detect internal as well as surface defects. Ultrasonic waves have a frequency usually greater than 20 kHz. Ultrasound techniques are sensitive, reproducible, and have become a critically important tool in nondestructive evaluations (NDE) (*Rose 1999; Yee and Couchman 1976*). This project examined the use of ultrasound as an NDE to determine the thickness and condition of the zinc anode and correlate it to the service life.

Ultrasound is used extensively as an NDE method by many industries worldwide, including: aerospace, medical, ship building, metal producers, chemical, transportation, and petroleum. Examples of the application of ultrasound in the medical field include obstetric ultrasound, and measuring corneal or other tissue thicknesses (*Cao, et al. 2002; Schumacher, et al. 1998*). In industry, ultrasound can be used to detect voids, cracks, and other defects that can appear due to a manufacturing process, during forging and welding, or just due to normal fatigue (*Yee and Couchman 1976*). Ultrasound is also routinely used to inspect nuclear reactors for defects from operation (*Shibata and Ishihara 2001; Pathak, et al. 1995*). The ultrasonic method is currently being researched in Japan as a possible NDE of concrete structures. In this study, ultrasound is used to locate voids and cracks embedded in concrete caused by corrosion of the reinforced steel (*Irie, et al. 2008*).

In theory, ultrasound is a simple technique. There are two modes of propagation in ultrasonic testing – bulk waves and guided waves. Bulk wave propagation, which includes longitudinal waves and transverse (shear) waves, refers to wave propagation in infinite media. Guided waves are those that require a boundary to propagate, most commonly consisting of surface waves (Lamb waves) and interface waves (*Rose 1999*). In ultrasonic testing, an ultrasonic pulse is transmitted from a probe and travels through the test material. Once the pulse hits a void, crack, or interface, the pulse is reflected back to the probe and is detected and recorded. In practice, there are several factors that must be considered when testing with ultrasound, including the following: the transducer, the condition of the test surface, the condition of the defect/interface surface, material attenuation, and material temperature (*McLaughlin 1989*).

The receiver is the ear in ultrasonic testing. After transmitting an ultrasonic signal, the receiver listens for echoes caused by imperfections in a given material and transmits them back to the data acquisition system for interpretation. Depending on the type of testing, two factors need to be considered when selecting a receiver – sensitively and resolution (*General Dynamics 1967*). The sensitivity of the receiver defines how well it is able to detect minute defects within a material. Different types of sensitivity are needed for different applications. The resolution or resolving power of a receiver refers to its ability to distinguish between noise and the desirable echoes (*General Dynamics 1967*).

The physical properties of the material under testing also need to be taken into consideration. The condition of the surface can affect how the pulse is transmitted. A rough surface can cause air gaps between the transducer and the surface. In these situations, a coupling gel can be used

to assist the travel of the ultrasonic pulse to the surface. Ultrasound travels through different materials at different speeds, referred to as wave velocity. Knowing the wave velocity of a material can be useful in determining how thick a material is. When using ultrasound to measure the thickness of a sample with multiple layers, the wave velocity becomes essential in determining the difference between layers. As long as two adjacent layers do not have similar velocities, ultrasound can be used to determine the thickness (*Rose 1999*). If two layers have similar wave velocities, the ultrasonic method may not be able to distinguish the two layers as different media.

Attenuation is another important physical property to consider in ultrasonic testing. It is the reduction in amplitude of the ultrasound pulse as a function of distance through the material. If a medium has a high attenuation, the pulse signal can be lost before it reaches the desired location. This can affect the quality of the signal received by the transducer.

A simple example of an ultrasonic test is illustrated in Figure 2.2. An ultrasonic pulse is applied to the surface of layer 1. From there the signal travels through the layer until it reaches the interface of layer 1 and 2. At the interface a portion of the pulse is reflected and the rest of the pulse is transmitted. The reflected signal travels back through layer 1 and is detected and recorded. By using the time of flight (TOF) method, the thickness of layer 1 can be calculated. A schematic of the results from this method is shown in Figure 2.2b.
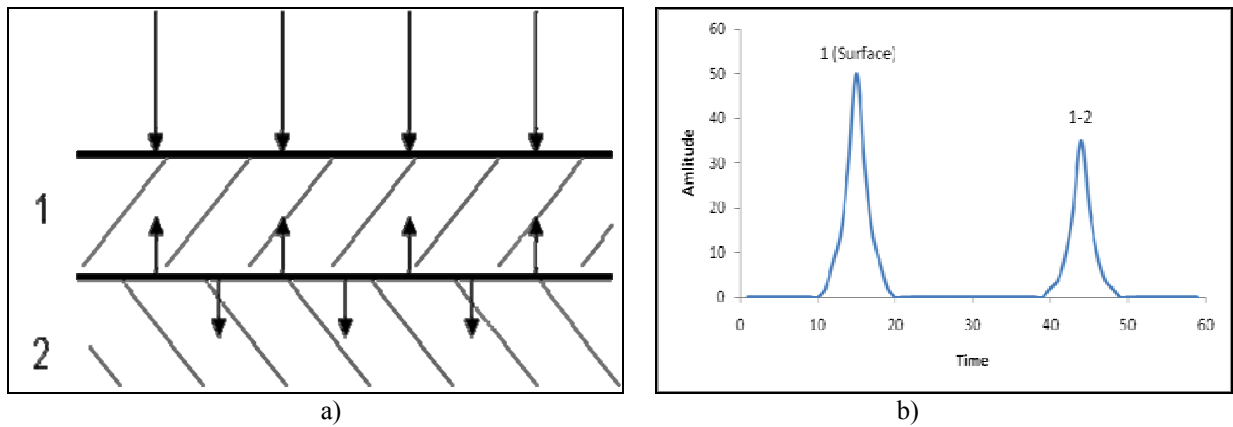
Figure 2.2: a) One-dimensional schematic of ultrasonic wave reflection and transmission between 2 media; b) pulse return of reflected wave at the interface of layer 1 and 2

This process can also be used in cases with multiple layers. It is assumed that each layer has a different wave velocity. In this scenario a third layer is added to the above example. The signal that is transmitted through the interface of layer 1 and 2 travels to the new interface between layer 2 and 3, as shown Figure 2.3a. The signal is again reflected and transmitted at the interface of layer 2 and 3. The reflected signal then travels back through layers 1 and 2 until it reaches the transducers, where the signal is then recorded (Figure 2.3b.

In this project, layer 1 may be zinc and layer 2 the zinc product layer. On the plot of signal vs. time an additional signal will be detected at a later time compared to the first signal. The time difference between the signal at the first interface and the signal at the second interface can be used to determine the thickness of the second layer. Ultrasonic testing was used in this research project to determine if this technique was capable of resolving the thicknesses of the zinc and the interfacial product layers.
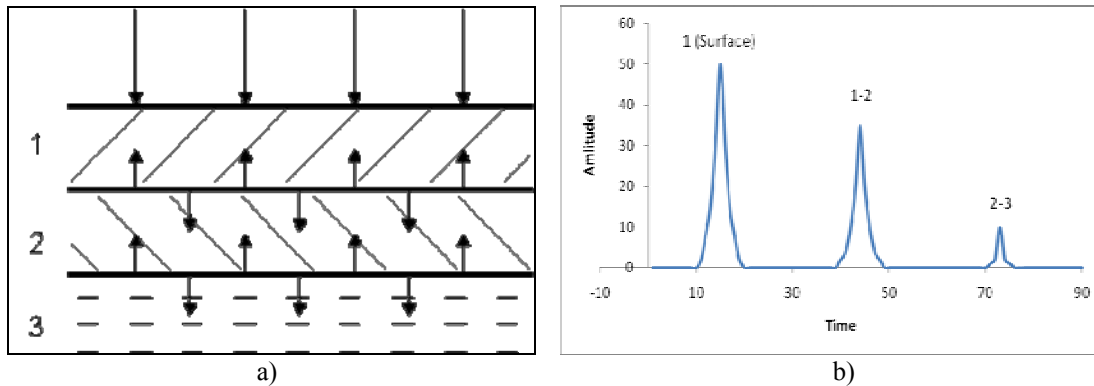
Figure 2.3: a) One-dimensional schematic of ultrasonic wave reflection and transmission between 3 layers; b) pulse return of reflected wave at the interface between 1 and 2 and the interface between 2 and 3

2.2.2 Resistance/permeability

Resistance measurements can provide an important evaluation of the condition of a steel reinforced concrete structure. The extent of metal loss from corroding steel is dependent on the ease with which the corrosion current can flow through the surrounding concrete (*Berkeley and Pathmanaban 1989*). The same consideration can be applied to the electrochemical cell in a CP system. The ease with which a current can flow will change as the anode is consumed and products are formed.

The geometry under consideration is illustrated in Figure 2.4. In this electrochemical cell current flows electronically through an external power supply, and the circuit is completed through the ionic conduction through the electrolyte in the concrete pores. This circuit is distinctly different than those that measure anode surface resistivity, e.g., using four point probe techniques.
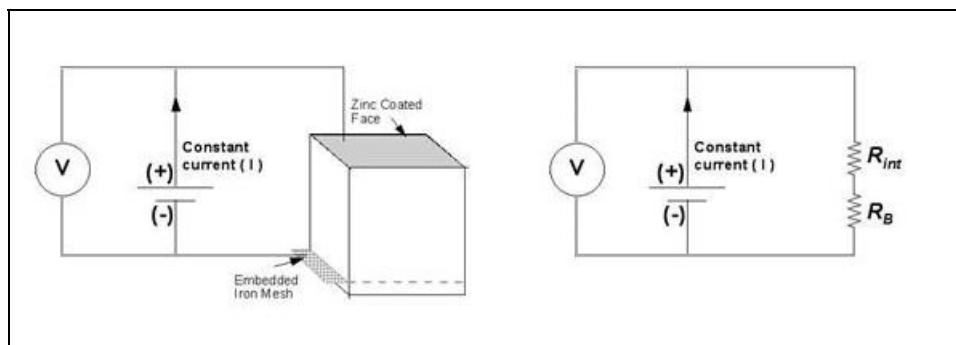
Figure 2.4: Illustration of pilot block and equivalent circuit, where R_{int} is the interfacial resistance and R_B is the bulk resistance (*Rehani 2000*)

Several researchers have reported a saw tooth pattern that correlates with wettings of the Zn surface (*Sagüés and Powers 1996; Rehani 2000; Covino, et al. 2002*). This pattern has been seen in potential difference vs. time plots with constant current, current density vs. time plots with constant potential, and resistance vs. time plots. When the surface is wetted, the curves show a decrease in potential and resistance and an increase in current. As the surface dries, the potential and resistance increases as the current decreases. The electrical behavior suggests two phases are present in the interfacial layer – a water soluble phase and an insoluble phase (*Rehani 2000*). Also the rate of decay appears to increase with age, presumably due to the buildup of the zinc product layer. These studies indicate that the zinc product layer affects the electrical response of the CP system with wetting.

For example, research at Oregon State University reported the potential difference between iron and zinc as the sample was aged (*Rehani 2000*). The applied current was set to 750 µA, and the zinc surface was periodically wetted when the potential difference reached -10 V. An illustration of the circuit is shown in Figure 2.4. It was observed that the magnitude of the potential difference (Fe vs. Zn) began to drop towards zero volts after the surface was sprayed, and the magnitude achieved a minimum value before rising towards -10 V again (Figure 2.5). A magnification of spray number 20 is shown in Figure 2.6. Here it can be seen that within a minute of spraying the surface of the sample the magnitude of the potential dropped to -0.7 V and eventually reached a minimum absolute value (or maximum value) of -0.4 V after 34 minutes (labeled by T_{dip}). This value is labeled E_{max}.

19
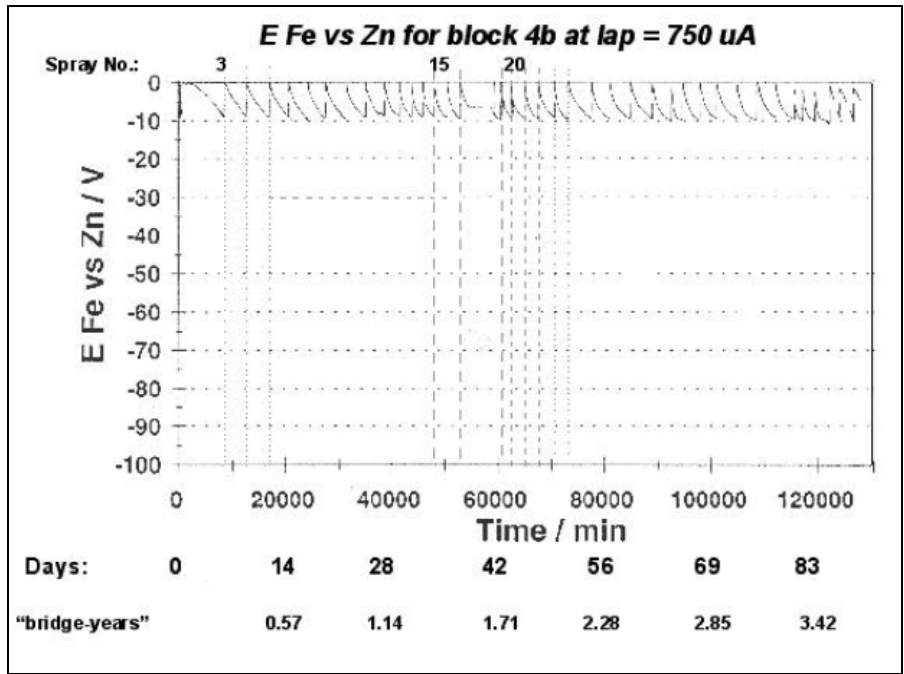
Figure 2.5: Potential difference of iron vs. zinc for periodically wetted sample (*Rehani 2000*)
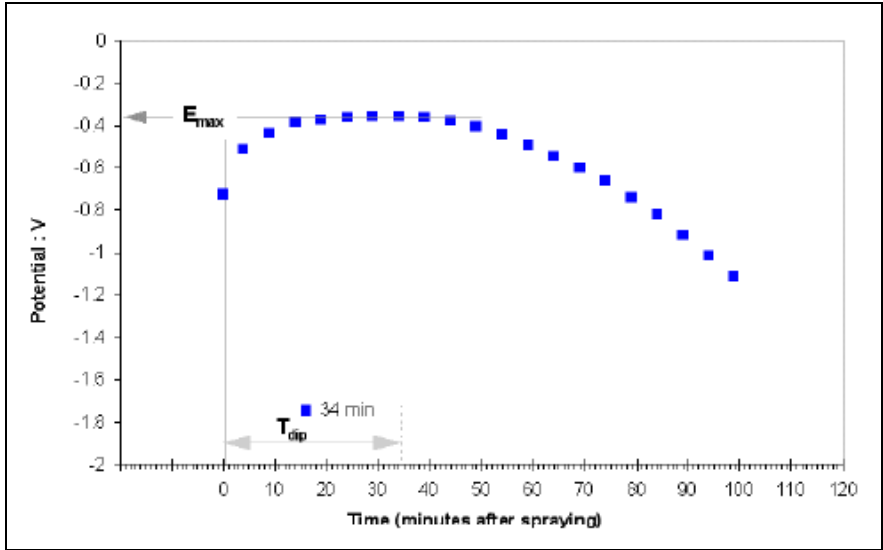
Figure 2.6: Potential difference of iron vs. zinc after spray number 20 (*Rehani 2000*)

It was observed that the time between successive sprays deceased with aging, and the value of E_{max} increased with aging. These differences were attributed to the growth of the zinc product layer at the interface as the system aged. The increase in products added to the overall resistance of the sample, thus increasing the value of E_{max} with time. Because the potential reached -10 V sooner, the time between successive sprays deceased with aging. It was postulated that the

20

products at the interfacial layer contain two phases – a water soluble phase and an insoluble phase. The value of E_{max} is reached when the soluble phase at the interfacial layer becomes solublized and increases as the soluble phase dries out over time (*Rehani 2000*). Thus the current research project was aimed at using a resistance method combined with water permeability as a possible technique to monitor the condition of the zinc anode on CP systems.

To help eliminate the effects of the water volume, a consistent finite amount of water was applied to a specific area of the zinc anode. The electrical response to this application of water was compiled and correlated to the anode condition. Electrical response can be measured in many different ways including resistance, dynamic voltage, cyclic voltage application, and others. A combination of these measurements and the permeability of the fluid were needed to develop a complete correlation of anode conditions, due to the range of interfacial chemistry and its effect on the electrical response.

3.0   EXPERIMENTAL PROCEDURES

3.1   ULTRASONIC WAVE MEASUREMENTS

3.1.1 Ultrasonic measurement system

An ultrasonic measurement system, designed with collaboration from Metis Design, was used to characterize the TS zinc anodes. The following constraints were incorporated into the design of the system: it needed to operate at a wavelength of less than 0.5 mm and have high resolution. A general schematic and laboratory setup of the system is shown in Figure 3.1.
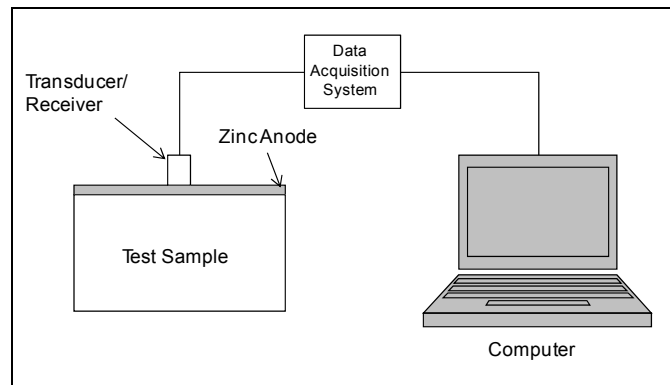
a)
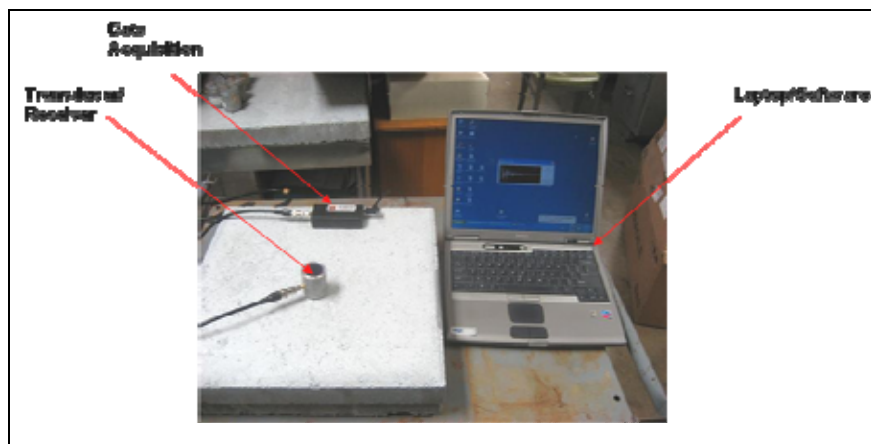
b)

Figure 3.1: a) General schematic of the ultrasonic measurement system; b) laboratory set-up of the ultrasonic measurement system

The computer was used to send, receive, and record the signal from the system. The custom software was designed to be used with the transducers and transmitted a step function actuator pulse shape with a 25 ns pulse width. The data that were collected from the receiver consisted of an average of 20 separate received signals from the 25 ns pulses. The transducer operated at a frequency of 10 - 15 MHz and had a sampling rate of 80 MHz with 14 bit resolution.

A general schematic of the transducer/receiver is shown in Figure 3.2. The transducer works by sending a signal down the signal connector to the electrode. Once the signal reaches the electrode, it causes the piezo crystals to vibrate. The vibration then transfers a signal into the titanium wear plate. From the titanium wear plate, the vibration is then transferred to the test site. The signal then travels through the material until it reaches the backside, where part of the signal is reflected back to the receiver. Upon return of the signal, the piezo crystals vibrate and the received signal is recorded by the computer.
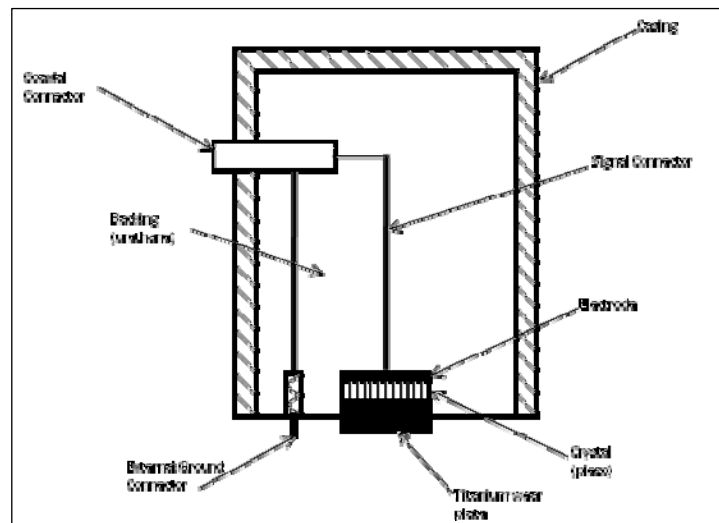
Figure 3.2: Schematic of ultrasonic transducers used during research

A total of six transducers were used in the ultrasonic measurement system. Table 3.1 shows the diameter of the piezo crystal and titanium wear plate for each transducer. The different sized diameters may cause a slight change in amplitude due to the change in capacitance.

In general, data were collected at 6 different locations on each zinc sample. Before running a test, glycerol or water was placed between the transducer and the zinc. The glycerol or water acted as a coupling gel to assist sound transmission into the test sample. Care needed to be taken on the placement of transducer when being used. To ensure that the majority of the longitudinal wave was transmitted into the sample, the transducer needed to be placed as flush with the surface as possible. Transverse waves, the part of the ultrasonic wave that travels perpendicular to the direction of energy transfer, can occur if the transducer is slightly angled.

3.1.2 Zinc samples for ultrasonic measurements

Ultrasonic measurements were performed on three different sets of samples. The first set of samples included zinc sheets and a zinc bar. Using the zinc sheet samples, lab experiments were designed to test the transducers and determine if they would be capable of differentiating different thicknesses of zinc samples. The nominal thicknesses of the samples are shown in Table 3.2.

Table 3.1: Diameter of piezo crystals in the corresponding transducer

Transducer #	Diameter (in)
1	0.050
2	0.075
3	0.100
4	0.150
5	0.200
6	0.250

Table 3.2: Zinc sheet samples

Sample #	Thickness (mils)	Thickness (mm)
1	20	0.51
2	27	0.69
3	30	0.76
4	40	1.02
5	60	1.52
6	850	21.5

The second set of zinc samples consisted of electrochemically aged concrete slabs acquired from NETL, which were constructed and aged in the study reported by *Covino, et al.* (*2002*). The samples contained a steel mesh placed 1.25 inches under the surface of the concrete slab. A steel mesh was used instead of the reinforced steel due to its size and ability to provide a uniform current density. Sodium chloride (NaCl) was added to the concrete mix prior to casting to imitate marine exposure of concrete. The concrete slabs were constructed with either 5 lb NaCl/yd^3 or 2 lb NaCl/yd^3. The slabs were allowed to cure in a moist room for three to four weeks and then air dried for one week. After the surfaces of the concrete slabs were sand blasted, an average thickness of 0.5 mm of zinc was thermally sprayed onto the slabs using an automated X-Y traversing system. The concrete slabs were then placed into a controlled temperature and constant humidity room to electrochemically age. The room was kept at a temperature of about 24°C, and the relative humidity was controlled at between 80% and 85%. The concrete slabs were then polarized at a current density of 3 mA/ft^2 to the desired equivalent bridge age. Bridge age was defined as the time it would take to pass the same amount of current on the field structure. A summary of the electrochemically aged concrete slabs used for the ultrasonic measurements is shown in Table 3.3.

Table 3.3: Aging and bond strength data of concrete blocks (*Covino, et al. 2002*)

Sample #	Charge (kC)	Uncertainty (+/- kC)	Average Adhesion Strength [MPa]	Approx. Years
7	44.0	0.6	1.81	7.0
8	83.9	1.1	1.03	13.3
9	127.6	1.7	0.21	20.2

Using previous adhesion measurements on the concrete blocks, locations for testing were chosen where the TS zinc anode was still adequately adhered to the concrete. Six different locations were chosen for each concrete block, and ten sets of data were taken at each site. This approach was used to test for repeatability as well as for the uniformity of each concrete block.

The surfaces of the concrete blocks were significantly rougher than the zinc sheet samples. The coupling gel played a key role in filling in the voids to allow the signal to transfer. Because of the roughness, however, it was not as easy to place the transducer flush with the surface. Any slight movement in the transducer could change the signal received by the receiver; the ultrasonic wave was altered by movement of the transducer. If the transducer were placed at an angle, the majority of the pulse could travel in the transverse and not longitudinal direction. This orientation would result in little to no signal at the receiver.

The final set of zinc samples consisted of specified thicknesses thermally sprayed onto unaged concrete slabs The TS zinc was applied by Great Western Corporation on 14 x 14 x 2 inch blocks using a twin wire arc process. The nominal thicknesses of the zinc coating on the unaged blocks are shown in Table 3.4. The experimental procedures for the unaged blocks were identical to the procedures for the electrochemically aged blocks.

Table 3.4: Unaged zinc standard sample thicknesses

Sample #	Thickness (mils)	Thickness (mm)
10	10	0.25
11	20	0.51
12	30	0.75
13	40	1.02

In addition, measurements were also performed on polished unaged samples. The zinc was polished in an attempt to provide a more uniform surface for the ultrasonic transducer. Polishing was accomplished by gluing a piece of sandpaper to the end of a flat drill bit. The bit was then placed into a drill press and used to sand the desired location. Slurry, an abrasive fluid commonly using in chemical mechanical planarization, was also used in conjunction with the sandpaper. After the desired location was polished, removing a small

fraction of the zinc anode, data were collected. This step was repeated several times on the same location.

3.2 RESISTANCE AND RESISTANCE/PERMEABILITY MEASUREMENTS

3.2.1 Electrochemical measurement system

Cyclic voltammetry was used to determine the resistance of the electrochemical cell depicted in Figure 1.3. A Pine Research Instrument, AFCBP1 biopotentiostat, was used as part of the laboratory resistance measuring system. A general schematic and laboratory setup of the system is shown in Figure 3.3. This system was sometimes modified from its three electrode design to allow a two electrode configuration by connecting the reference and counter electrodes.
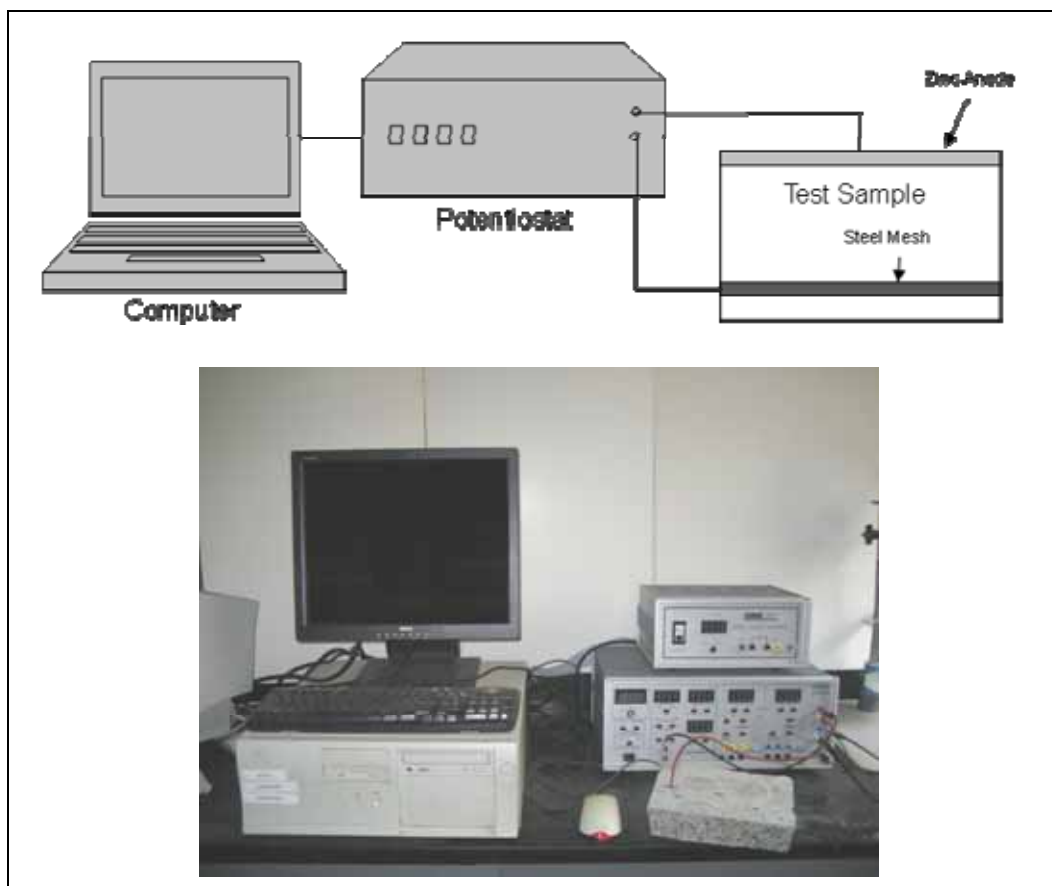
Figure 3.3: General schematic and photograph of the electrochemical measurement system

Before a resistance experiment was performed, the value of the open circuit potential (E_{ocp}, Zn vs. Fe) for a sample was determined by connecting the leads from the Zn and Fe electrodes to a high impedance multimeter. A cyclic voltammetry sweep experiment was then performed around the value of E_{ocp}. The parameters used during the sweep are shown in Table 3.5. Figure 3.4 represents the potential vs. time for the experiment. The current was recorded as the voltage was swept, and the resistance was determined by taking the inverse of the slope of the best fit line of the current vs. voltage data.

Table 3.5: Cyclic voltammetry sweep parameters

Initial Potential (mV)	E_{OCP}
Initial sweep direction (Up or Down)	Up
Sweep rate (mV/sec)	5
Number of sweeps	7
Maxium potential (mV)	E_{OCP}+ 30
Minimum potential (mV)	E_{OCP} - 30
Final Potential (mV)	E_{OCP}
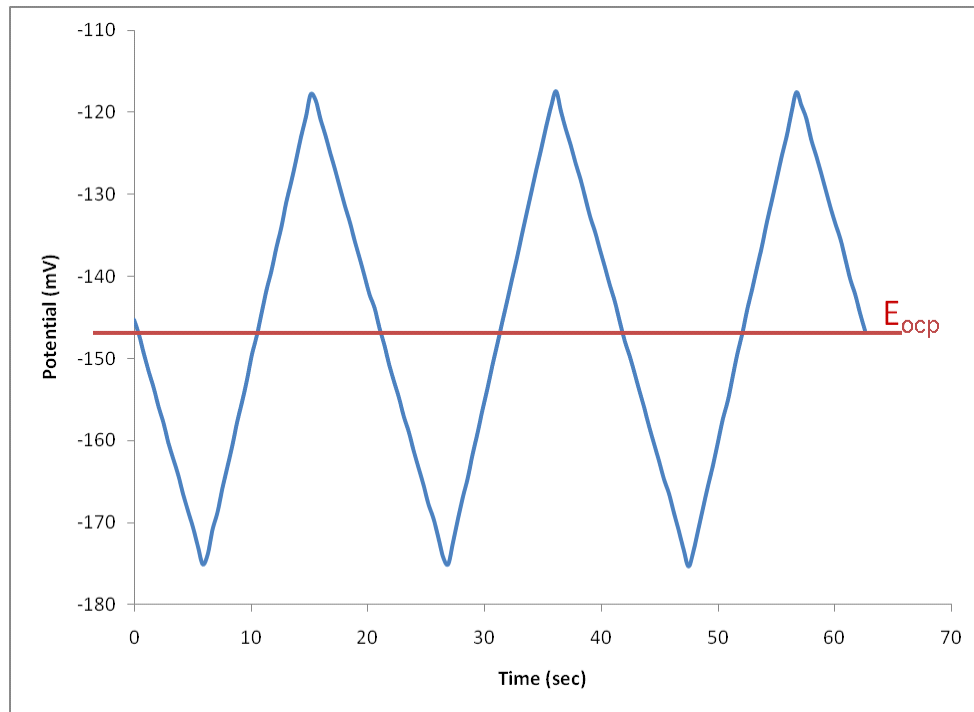
Figure 3.4: Variation of applied potential with time in cyclic voltammetry

3.2.2 Samples

Resistance measurements were taken on concrete slabs electrochemically aged by NETL, as discussed above. The steel wire attached to the steel mesh was sanded to minimize other sources of resistance. The resistance introduced by iron oxides could affect the desired resistance measurement of the zinc product layer. Cables were soldered directly to the steel wire and the zinc surface. Flux was used to prevent the formation of metal oxides and to act as a wetting agent. Figure 3.5 shows a concrete block with the wire leads soldered onto the zinc and iron wire.

Figure 3.5: Example of electrochemically aged block used for resistance measurements

Two separate resistance measurements were performed on electrochemically aged samples. The first experiment was performed on the concrete slabs in the condition that they were stored, and this was labeled the "dry" resistance measurement. The dry resistance test was performed to determine the relationship between the resistance of a concrete slab and its electrochemical age. The second experiment was designed to measure the dynamic electrical response as the block was wetted, and this was labeled the "wet" resistance measurement.

The dry resistance measurement used five different electrochemically aged concrete slabs as shown in Table 3.6. After the value of E_{ocp} was determined for a block, it was connected to the potentiostat and the voltage was swept. Experimental runs were performed on each electrochemically aged block three times a day. The multiple tests were carried out to test the repeatability of the resistance measurements. Humidity and temperature were also recorded during the experiment. To reproduce a cold environment, concrete blocks were chilled in a refrigerator for 1 day prior to the resistance measurement. This was performed to ensure that the temperature in the concrete block reached equilibrium.

Table 3.6: Electrochemically aged samples

Sample #	Charge (kC)	Uncertainty (+/- kC)	Average Adhesion Strength [Mpa]	Approx. Years
14	0.0	0.0	1.19	0.0
15	11.6	0.2	1.65	1.8
16	20.1	0.3	1.72	3.2
17	51.9	0.7	2.95	8.2
18	90.2	1.2	1.28	14.3

Two different concrete slabs were selected for wet resistance measurements – one aged approximately 1.8 years and the other 7.4 years. Previous bond strength measurements had been performed on the concrete blocks, leaving bare concrete exposed. The bare concrete would have allowed water to be easily absorbed, so a device was constructed to contain the water to the sprayed Zn anode surface while resistance measurements were taken. The device needed to be versatile and adjustable to accommodate the different sizes of the concrete blocks. The device also needed to be capable of taking measurements at different locations. The device was designed to compress a clear plastic tube onto a rubber o-ring. The o-ring was used to make a watertight seal at the zinc anode surface. The device setup is shown in Figure 3.6. It was constructed out of steel to ensure that it was strong and sturdy and would not bend

Figure 3.6: Device used in wet resistance measurements

Before any water was applied, a dry resistance test was performed to establish a baseline. Next, 1 or 4 mL of water were added directly onto the zinc anode where the lead was

soldered on. A resistance measurement was taken directly after the water had been added. Measurements were taken in increments of thirty minutes throughout the day. The cyclic voltammetry sweep was adjusted throughout the experiment to ensure that the sweep stayed within ±30mV of E_{ocp}. To increase the surface area being wetted the setup was slightly altered. Instead of applying the water directly onto the lead, it was placed in multiple spots next to the lead. This configuration allowed the sample to have a larger surface area that was wetted.

4.0   ULTRASONIC TESTING

In this chapter, results from the ultrasonic measuring system will be presented together with a mathematical model of these results. This model for the propagation of ultrasound in a solid media was developed to better interpret and understand the response signal received by the transducer. Three different sets of zinc samples were analyzed, as described in Chapter 3. Zinc sheet samples were tested to determine the capabilities of the ultrasonic system to differentiate different thicknesses of zinc. Ultrasonic testing was next performed on electrochemically aged samples to determine if a relationship between the remaining zinc anode and the electrochemical age of the sample could be established. To simplify the system, unaged samples were investigated to pinpoint characteristic changes due to thickness.

4.1 MODEL OF ULTRASONIC WAVES THROUGH SOLID MATERIAL

The equations used in the development of the model are discussed in this section. For simplicity, it is assumed that the ultrasonic waves propagate in one-dimensional geometry, as shown in Figure 4.1. The transducer is placed at the outer surface of the zinc layer. Ultrasonic waves are transmitted through the layer of sprayed zinc and the concrete. At the zinc concrete interface a portion of the ultrasonic wave is transmitted and the rest reflected.
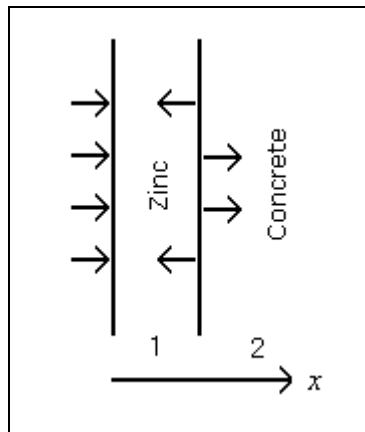
Figure 4.1: One-dimensional schematic of ultrasonic wave reflection

The governing equation for this model is the basic wave equation:

$$c^2 \frac{\partial^2 u}{\partial^2 x} = \frac{\partial^2 u}{\partial^2 t}$$

(4-1)

where u is the displacement vector along the x-axis; c is the wave velocity of sound in the material; and t is time. The x-axis represents the position of the ultrasonic wave as it is traveling through the material.

In the case of two materials in contact, the interface at which the two materials connect, specified by $x=x_{12}$, is subjected to the following boundary condition:

$$u_1(x_{12},t) = u_2(x_{12},t) \tag{4-2}$$

$$\sigma_x^1 = \sigma_x^2 \tag{4-3}$$

where σ is the stress tensor in the material. The generalized Hooke's law for a one-dimensional case is:

$$\sigma = (\lambda + 2\mu)\frac{\partial u}{\partial x} \tag{4-4}$$

where λ is the Lamé constant and μ is the shear modulus, and

$$\rho c^2 = (\lambda + 2\mu) \tag{4-5}$$

where ρ is the density of the material (*Rose 1999*). Hence Equation 4-3 can be rewritten as:

$$\rho_1 c_1^2 \frac{\partial u_1}{\partial x}(x_{12},t) = \rho_2 c_2^2 \frac{\partial u_2}{\partial x}(x_{12},t) \tag{4-6}$$

Next we consider a sound wave with a given angular frequency ω. The angular frequency is related to the regular frequency f by $\omega = 2\pi f$. The general solution for the displacement vector, u, in Equation 4-1 is:

$$u = Te^{i(kx-\omega t)} + Re^{i(-kx-\omega t)} \tag{4-7}$$

where the first term describes the wave traveling in the positive x direction (transmission) and the second term describes the wave traveling in the negative x direction (reflection).

Substituting Equation 4-7 into Equation 4-2 gives:

$$T_1 e^{i(k_1 x-\omega t)} + R_1 e^{i(-k_1 x-\omega t)} = T_2 e^{i(k_2 x-\omega t)} + R_2 e^{i(-k_2 x-\omega t)} \tag{4-8}$$

calculated at $x=x_{12}$. It is assumed that the frequency traveling left and right are the same. For Equation 4-8 to be true at all times, the frequency traveling left and right cannot be different. Since the frequency is the same, the time dependent term in Equation 4-8 drops out and Equation 4-9 is obtained.

$$T_1 e^{i(k_1 x)} + R_1 e^{i(-k_1 x)} = T_2 e^{i(k_2 x)} + R_2 e^{i(-k_2 x)} \tag{4-9}$$

34

Applying the same assumption to the second boundary condition yields:

$$\rho_1 c_1^2 i k_1 \left(T_1 e^{i(k_1 x)} - R_1 e^{i(-k_1 x)} \right) = \rho_2 c_2^2 i k_2 \left(T_2 e^{i(k_2 x)} - R_2 e^{i(-k_2 x)} \right) \tag{4-10}$$

Using the relationship between wave number k and frequency ω:

$$ck = \omega \tag{4-11}$$

Equation 4-10 can be rewritten:

$$\rho_1 c_1 \left(T_1 e^{i(k_1 x)} - R_1 e^{i(-k_1 x)} \right) = \rho_2 c_2 \left(T_2 e^{i(k_2 x)} - R_2 e^{i(-k_2 x)} \right) \tag{4-12}$$

Next, Equation 4-9 and 4-12 can be combined into a matrix form, as follows:

$$\begin{pmatrix} 1 & 1 \\ \rho_1 c_1 & -\rho_1 c_1 \end{pmatrix} \begin{pmatrix} T_1 e^{i(k_1 x)} \\ R_1 e^{i(-k_1 x)} \end{pmatrix} = \begin{pmatrix} 1 & 1 \\ \rho_2 c_2 & -\rho_2 c_2 \end{pmatrix} \begin{pmatrix} T_2 e^{i(k_2 x)} \\ R_2 e^{i(-k_2 x)} \end{pmatrix} \tag{4-13}$$

Again, this is calculated at $x=x_{12}$. To solve for the coefficients T_2 and R_2 in terms of the coefficients T_1 and R_1, the 2x2 matrix is inverted and multiplied on both sides. The coefficients T_2 and R_2 can be separated from the exponent to form two separated matrices. Multiplying the inverse of the exponent on both sides yields the following matrix:

$$\begin{pmatrix} T_2 \\ R_2 \end{pmatrix} = \frac{1}{2\rho_2 c_2} \begin{pmatrix} e^{i(-k_2 x)} & 0 \\ 0 & e^{i(k_2 x)} \end{pmatrix} \begin{pmatrix} \rho_2 c_2 & 1 \\ \rho_2 c_2 & -1 \end{pmatrix} \begin{pmatrix} 1 & 1 \\ \rho_1 c_1 & -\rho_1 c_1 \end{pmatrix} \begin{pmatrix} T_1 e^{i(k_1 x)} \\ R_1 e^{i(-k_1 x)} \end{pmatrix} \tag{4-14}$$

or

$$\begin{pmatrix} T_2 \\ R_2 \end{pmatrix} = \frac{1}{2\rho_2 c_2} \begin{pmatrix} e^{i(-k_2 x)} & 0 \\ 0 & e^{i(k_2 x)} \end{pmatrix} \begin{pmatrix} \rho_2 c_2 + \rho_1 c_1 & \rho_2 c_2 - \rho_1 c_1 \\ \rho_2 c_2 - \rho_1 c_1 & \rho_2 c_2 + \rho_1 c_1 \end{pmatrix} \begin{pmatrix} e^{i(k_1 x)} & 0 \\ 0 & e^{i(-k_1 x)} \end{pmatrix} \begin{pmatrix} T_1 \\ R_1 \end{pmatrix} \tag{4-15}$$

If a third material (zinc product layer) exists, a following layer would be added between the zinc and concrete layer shown in Figure 4.1. Then the previous calculations would be repeated for the interface where the second and third material connect. This procedure leads to Equation 4-16:

$$\begin{pmatrix} T_3 \\ R_3 \end{pmatrix} = \frac{1}{2\rho_3 c_3} \begin{pmatrix} e^{i(-k_3 x)} & 0 \\ 0 & e^{i(k_3 x)} \end{pmatrix} \begin{pmatrix} \rho_3 c_3 + \rho_2 c_2 & \rho_3 c_3 - \rho_2 c_2 \\ \rho_3 c_3 - \rho_2 c_2 & \rho_3 c_3 + \rho_2 c_2 \end{pmatrix} \begin{pmatrix} e^{i(k_2 x)} & 0 \\ 0 & e^{i(-k_2 x)} \end{pmatrix} \begin{pmatrix} T_2 \\ R_2 \end{pmatrix} \tag{4-16}$$

for $x=x_{23}$. Substituting Equation 4-15 into Equation 4-16 yields:

$$\begin{pmatrix} T_3 \\ R_3 \end{pmatrix} = \frac{1}{2\rho_3 c_3} \begin{pmatrix} e^{i(-k_3 x_{23})} & 0 \\ 0 & e^{i(k_3 x_{23})} \end{pmatrix} \begin{pmatrix} p_3 c_3 + p_2 c_2 & p_3 c_3 - p_2 c_2 \\ p_3 c_3 - p_2 c_2 & p_3 c_3 + p_2 c_2 \end{pmatrix} \begin{pmatrix} e^{i(k_2 x_{23})} & 0 \\ 0 & e^{i(-k_2 x_{23})} \end{pmatrix}$$
$$\frac{1}{2\rho_2 c_2} \begin{pmatrix} e^{i(-k_2 x_{12})} & 0 \\ 0 & e^{i(k_2 x_{12})} \end{pmatrix} \begin{pmatrix} p_2 c_2 + p_1 c_1 & p_2 c_2 - p_1 c_1 \\ p_2 c_2 - p_1 c_1 & p_2 c_2 + p_1 c_1 \end{pmatrix} \begin{pmatrix} e^{i(k_1 x_{12})} & 0 \\ 0 & e^{i(-k_1 x_{12})} \end{pmatrix} \begin{pmatrix} T_1 \\ R_1 \end{pmatrix}$$

(4-17)

where x_{12} is the interface of media 1 and 2, and x_{23} is the interface of media 2 and 3.

To solve this equation it is assumed that a wave starts from the left with an amplitude of 1, $T_1 = 1$. The last medium is infinitely long in the x-direction, so $R_3 = 0$. R_3 represents the signal that would be reflected at the back of the concrete sample. To further simplify the matrix, it is assumed that the first interface at $x = x_{12} = 0$. The second interface, $x = x_{23}$, is some distance, d, along the x-axis. Next we define:

$$D_{12} = \frac{p_2 c_2 - p_1 c_1}{p_2 c_2 + p_1 c_1}$$

(4-18)

$$D_{23} = \frac{p_3 c_3 - p_2 c_2}{p_3 c_3 + p_2 c_2}$$

(4-19)

simplifying Equation 4-16 to:

$$\begin{pmatrix} T_3 \\ 0 \end{pmatrix} = \frac{p_3 c_3 + p_2 c_2}{2\rho_3 c_3} \frac{p_2 c_2 + p_1 c_1}{2\rho_2 c_2}$$
$$\begin{pmatrix} e^{i(k_2 - k_3)d} + D_{12} D_{23} e^{-i(k_2 + k_3)d} & D_{12} e^{i(k_2 - k_3)d} + D_{23} e^{-i(k_2 + k_3)d} \\ D_{12} e^{-i(k_2 - k_3)d} + D_{23} e^{i(k_2 + k_3)d} & e^{-i(k_2 - k_3)d} + D_{12} D_{23} e^{i(k_2 + k_3)d} \end{pmatrix} \begin{pmatrix} 1 \\ R_1 \end{pmatrix}$$

(4-20)

By looking at the bottom portion of Equation 4-20, R_1 can be found:

$$R_1 = -\frac{D_{12} e^{-i(k_2 - k_3)d} + D_{23} e^{i(k_2 + k_3)d}}{e^{-i(k_2 - k_3)d} + D_{12} D_{23} e^{i(k_2 + k_3)d}}$$

(4-21)

This equation can be simplified by factoring out k_3 from each term.

$$R_1 = -\frac{D_{12} e^{-ik_2 d} + D_{23} e^{ik_2 d}}{e^{-ik_2 d} + D_{12} D_{23} e^{ik_2 d}}$$

(4-22)

A third interface can now be added at $x = x_{34} = d + D$, giving:

$$\begin{pmatrix} T_4 \\ R_4 \end{pmatrix} = \frac{1}{2\rho_4 c_4} \begin{pmatrix} e^{-ik_4(d+D)} & 0 \\ 0 & e^{ik_4(d+D)} \end{pmatrix}$$

$$\begin{pmatrix} p_4 c_4 + p_3 c_3 & p_4 c_4 - p_3 c_3 \\ p_4 c_4 - p_3 c_3 & p_4 c_4 + p_3 c_3 \end{pmatrix} \begin{pmatrix} e^{ik_3(d+D)} & 0 \\ 0 & e^{-ik_3(d+D)} \end{pmatrix} \begin{pmatrix} T_3 \\ R_3 \end{pmatrix} \tag{4-23}$$

Substituting Equation 4-17 leads to the following equation.

$$\begin{pmatrix} T_4 \\ 0 \end{pmatrix} = \frac{1}{2\rho_4 c_4} \begin{pmatrix} e^{-ik_4(d+D)} & 0 \\ 0 & e^{ik_4(d+D)} \end{pmatrix} \begin{pmatrix} p_4 c_4 + p_3 c_3 & p_4 c_4 - p_3 c_3 \\ p_4 c_4 - p_3 c_3 & p_4 c_4 + p_3 c_3 \end{pmatrix} \begin{pmatrix} e^{ik_3(d+D)} & 0 \\ 0 & e^{-ik_3(d+D)} \end{pmatrix}$$

$$\frac{1}{2\rho_3 c_3} \begin{pmatrix} e^{i(-k_3 x_{23})} & 0 \\ 0 & e^{i(k_3 x_{23})} \end{pmatrix} \begin{pmatrix} p_3 c_3 + p_2 c_2 & p_3 c_3 - p_2 c_2 \\ p_3 c_3 - p_2 c_2 & p_3 c_3 + p_2 c_2 \end{pmatrix} \begin{pmatrix} e^{i(k_2 x_{23})} & 0 \\ 0 & e^{i(-k_2 x_{23})} \end{pmatrix} \tag{4-24}$$

$$\frac{1}{2\rho_2 c_2} \begin{pmatrix} e^{i(-k_2 x_{12})} & 0 \\ 0 & e^{i(k_2 x_{12})} \end{pmatrix} \begin{pmatrix} p_2 c_2 + p_1 c_1 & p_2 c_2 - p_1 c_1 \\ p_2 c_2 - p_1 c_1 & p_2 c_2 + p_1 c_1 \end{pmatrix} \begin{pmatrix} e^{i(k_1 x_{12})} & 0 \\ 0 & e^{i(-k_1 x_{12})} \end{pmatrix} \begin{pmatrix} 0 \\ R_1 \end{pmatrix}$$

Solving for R_1, gives a final equation:

$$R_1 = -\frac{D_{34}\left[e^{i(k_2 d + k_3 D)} + D_{12} D_{23} e^{i(-k_2 d + k_3 D)} \right] + \left[D_{12} e^{-i(k_2 d + k_3 D)} + D_{23} e^{i(k_2 d - k_3 D)} \right]}{D_{34}\left[D_{12} e^{i(k_2 d + k_3 D)} + D_{23} e^{i(-k_2 d + k_3 D)} \right] + \left[e^{-i(k_2 d + k_3 D)} + D_{12} D_{23} e^{i(k_2 d - k_3 D)} \right]} \tag{4-25}$$

Matlab was used to solve these equations. The solution allowed better understanding of the response that should be received by the transducer. The code for Matlab can be found in Appendix B.

According to Equation 4-25, three variables can vary. These variables are frequency, thickness of the zinc layer, and thickness of the product layer. The density and wave velocity are all physical parameters of the media. Using Equation 4-25 two different types of plots are made. Shown in Figure 4.2 is an example of the first plot, a received signal, R_1, versus frequency, f. Recall that angular frequency is related to frequency by the following equation:

$$\omega = 2\pi f \tag{4-26}$$

It is assumed that the initial thickness of the zinc layer, d_2, is 0.5 mm ($\approx$20 mils).
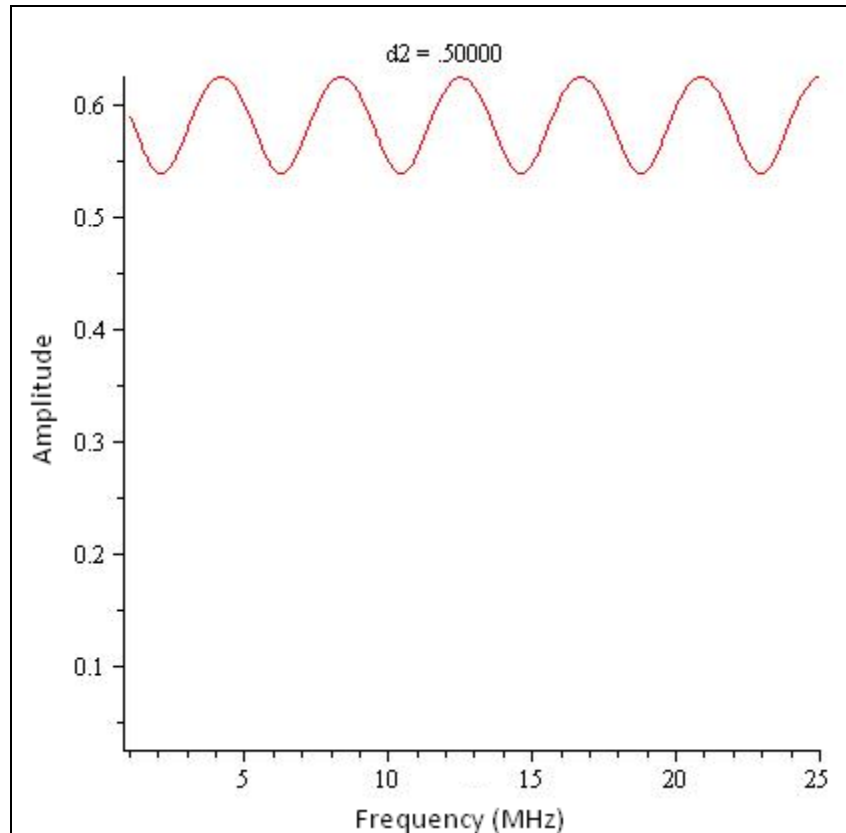
Figure 4.2: Plot of amplitude versus frequency

As the zinc anode is electrochemically aged, zinc products form at the interface. It was assumed that the thickness of the product layer increased as the thickness of the zinc layer decreased. For simplicity, it was approximated that the sum of the thicknesses of zinc and zinc products was equal to the original thickness of the zinc anode ($d_2 + d_3 = 0.5$). This approximation, however, did not account for the volume increase of the reaction products. Figures 4.3 and 4.4 show changes to the amplitude of the received wave, at values of d_2 of 0.33 and 0.25, i.e., as d_2 decreased and d_3 increased.

Based on the data in Figures 4.3 and 4.4, it was speculated that as the zinc anode is electrochemically aged and consumed, the frequency and the amplitude shifts. There was a large drop in the reflection coefficient around 13 - 16 MHz. The information gathered from analyzing the model was applied to analyze data collected from the three sets of samples. A comparison of a Fourier analysis of different electrochemically aged samples was expected to result in a difference in the received signal strengths.

38
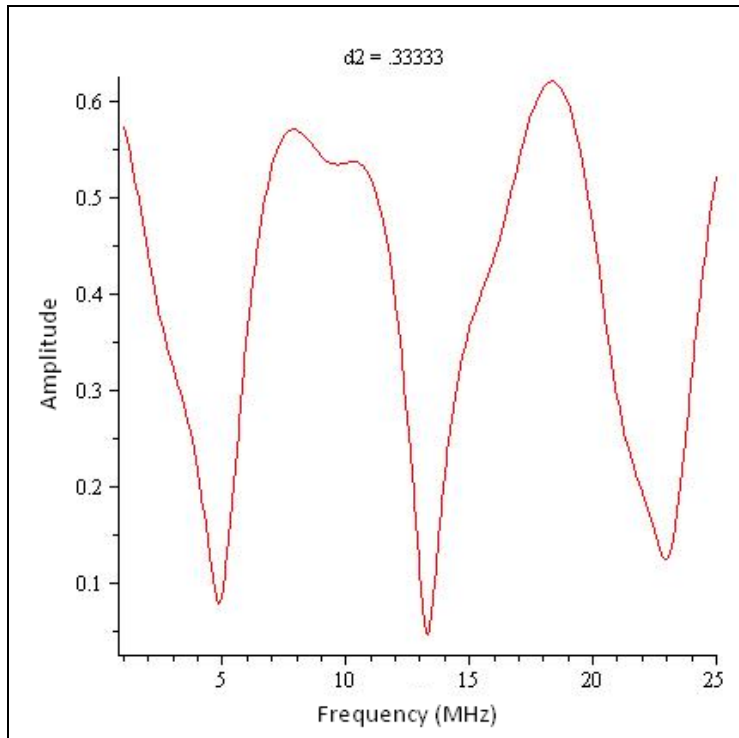
Figure 4.3: Plot of amplitude versus frequency for d2 = 0.333
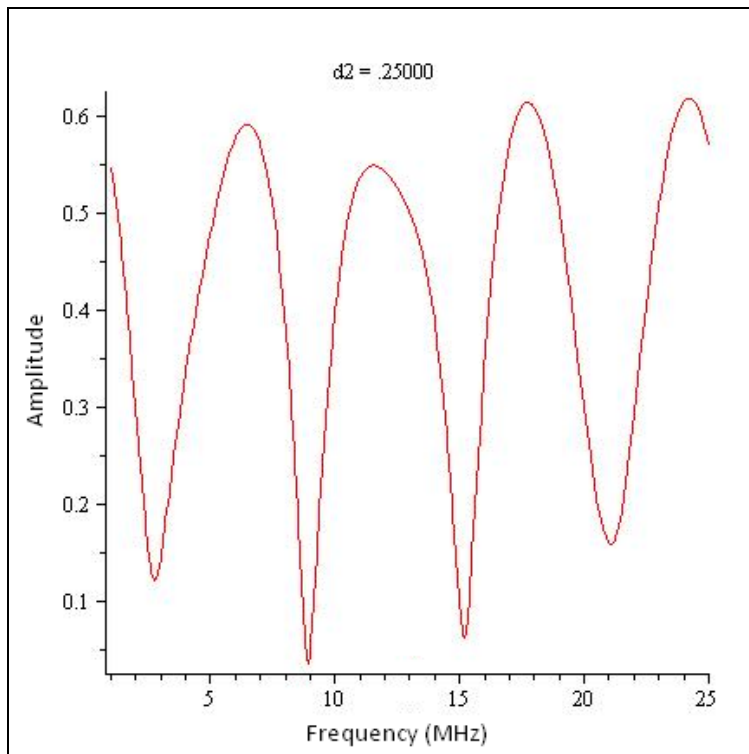
Figure 4.4: Plot of amplitude versus frequency for d2 = 0.25

The second type of plot using the model was a three-dimensional plot. In this plot, the frequency was held constant and the reflection coefficient was calculated by changing the values of d_2 and d_3. In this plot, the thickness of d_3, the product layer, was not restricted by the consumption of d_2, the zinc anode; hence the behavior was more realistic. The model was used to analyze the effect on the received signal based on different combinations of thicknesses of the zinc and zinc product layers.

Figures 4.5 - 4.7 show plots of model results for frequencies of 25, 15 and 7 MHz, respectively. Similar results were observed when compared to the first analysis. The three-dimensional plots indicate drastic changes in the amplitude of the reflection coefficient. These changes can be identified by the valley like dips in Figures 4.5 - 4.7. Results from this model therefore indicate that ultrasonic techniques could be a viable process to analyze the condition of TS zinc anodes on CP systems.
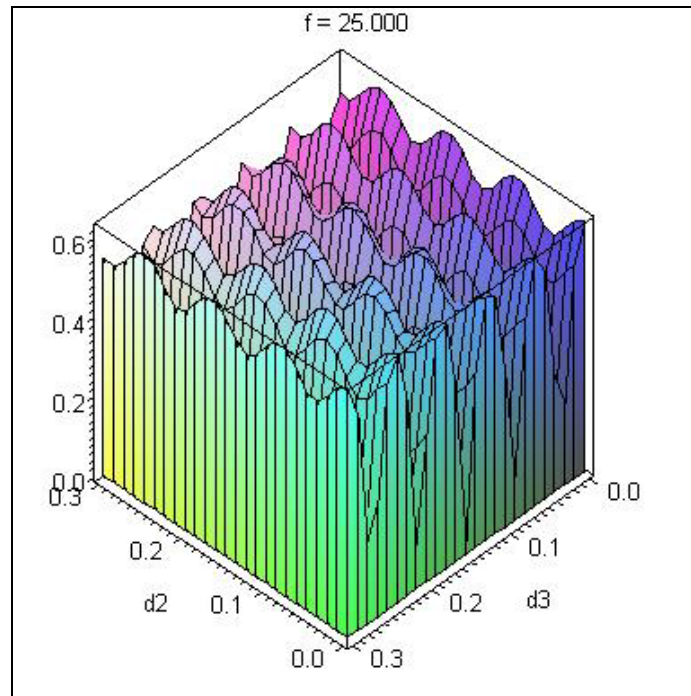
Figure 4.5: 3D plot of amplitude vs. d2 and d3 (in mm) for f = 25 MHz
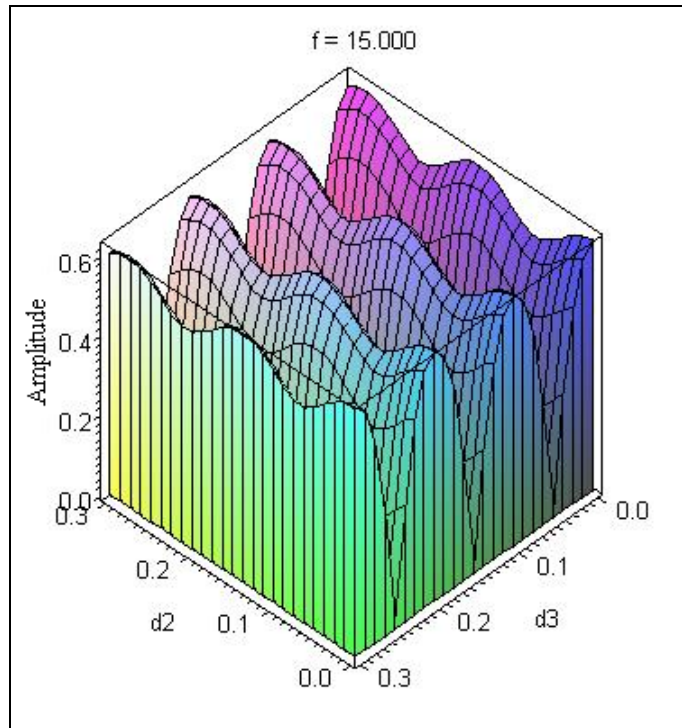
Figure 4.6: 3D plot of amplitude vs. d2 and d3 (in mm) for f = 15 MHz
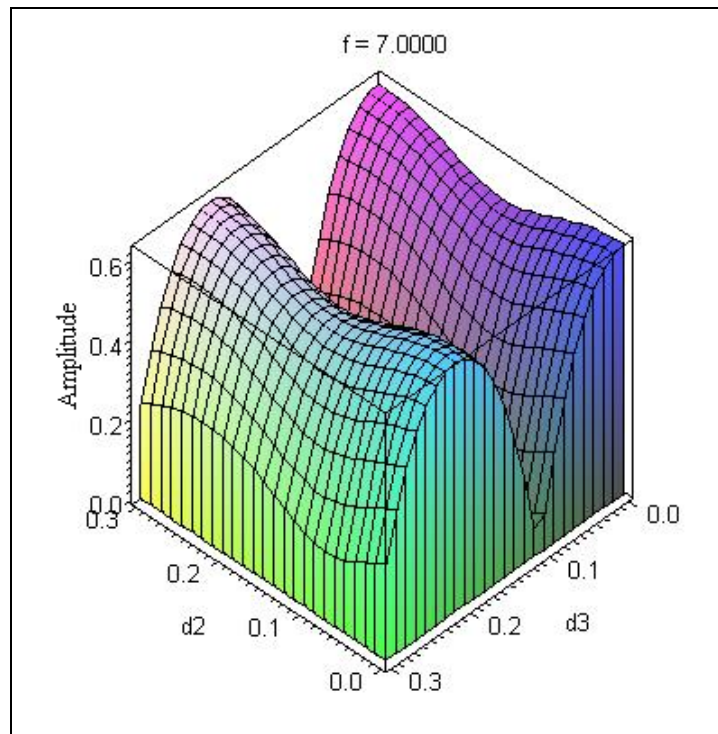
Figure 4.7: 3D plot of amplitude vs. d2 and d3 (in mm) for f = 7 MHz

A schematic of the experiment is shown in Figure 4.8. Note that this schematic is not drawn to scale but used as a representation of the experimental conditions. Using an ultrasonic transducer, an incident pulse is transmitted into the titanium wear plate. When the ultrasonic pulse reaches the titanium/zinc interface a portion of the pulse is transmitted and reflected. This is indicated by the red and blue arrows shown in Figure 4.8.

The signal that is transmitted at the titanium/zinc interface travels through the zinc layer until it reaches the zinc/concrete interface (in the case of an unaged sample). The signal is again transmitted and reflected at this second interface. It is assumed that no signal is reflected from the back of the concrete sample, because the thickness of the concrete is assumed to be infinitely thick compared to the thicknesses of the zinc anode or zinc products. In the case of an aged sample, a product layer exists, and an additional refection and transmission of the ultrasonic wave occurs at the zinc-zinc product interface. The time-of-flight (TOF) echo return is used as a basis for evaluation of the data.
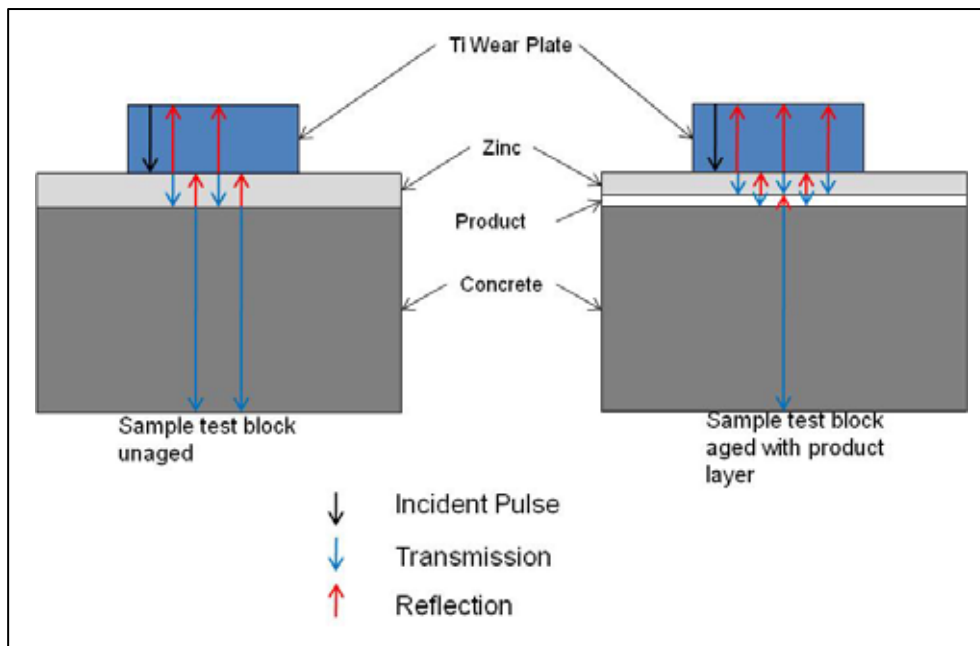
Figure 4.8: Schematic of reflected and transmitted ultrasonic waves in experimental conditions, an unaged sample on the left and an aged sample on the right

4.2 ZINC SHEET SAMPLE DATA

Laboratory experiments were next conducted to confirm the results obtained from the model. Tests were conducted on six different samples summarized in Table 3.2. An example of the raw data collected from sample six is shown in Figure 4.9. Once the transducer was initialized, a 25 ns step function spike pulse was transmitted. The first measured signal was received at about 0.1 µs. The signal prior to 0.1 µs was an internal precursor that occurred within the transducer.

In Figure 4.9, the section labeled "Pre" shows that the signal first expanded in one direction, then expanded in the other direction, and was slowly damped out. As the signal was dampened out, additional signals were received from the titanium wear plate every few microseconds until the pulses started to merge together. These signals represented the ultrasonic wave bouncing back and forth in the titanium wear plate as well as reflected signals from the interfaces of the different layers. It was observed that the amplitude of received signal decreased with each additional set. The decrease in signal was due to the attenuation effect of the medium. Attenuation can be due to internal friction or energy absorption in the material and the geometry of the wave propagation – spherical or cylindrical.
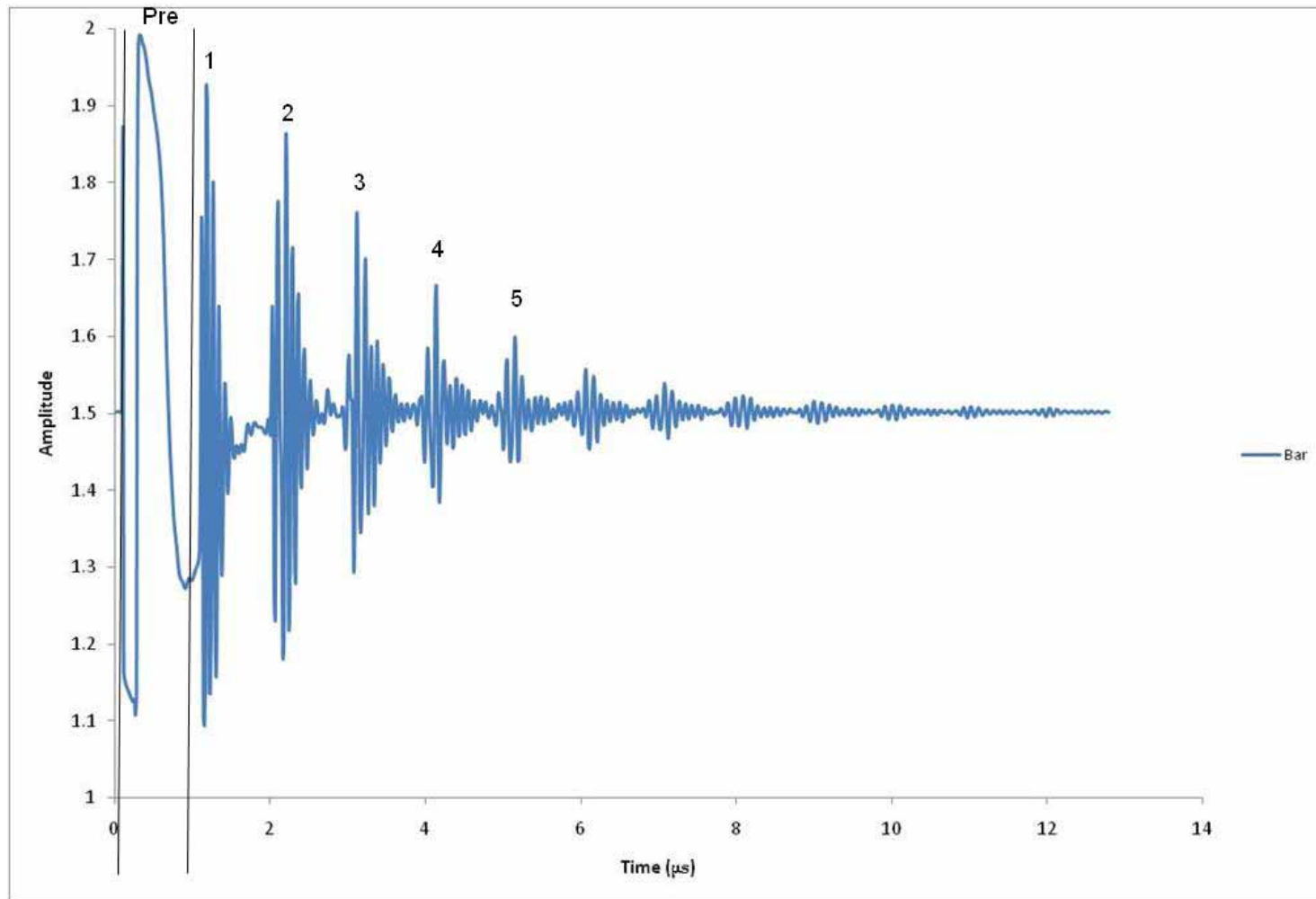
Figure 4.9: Raw data plot of amplitude vs. time of zinc bar

The next step in analyzing the data was to remove the background noise from the data. This signal processing was accomplished by fitting a double exponential to the data. Figure 4.10 shows the fitted background noise to the raw data. Since the precursor signal was not significant in the analysis it was removed, too.
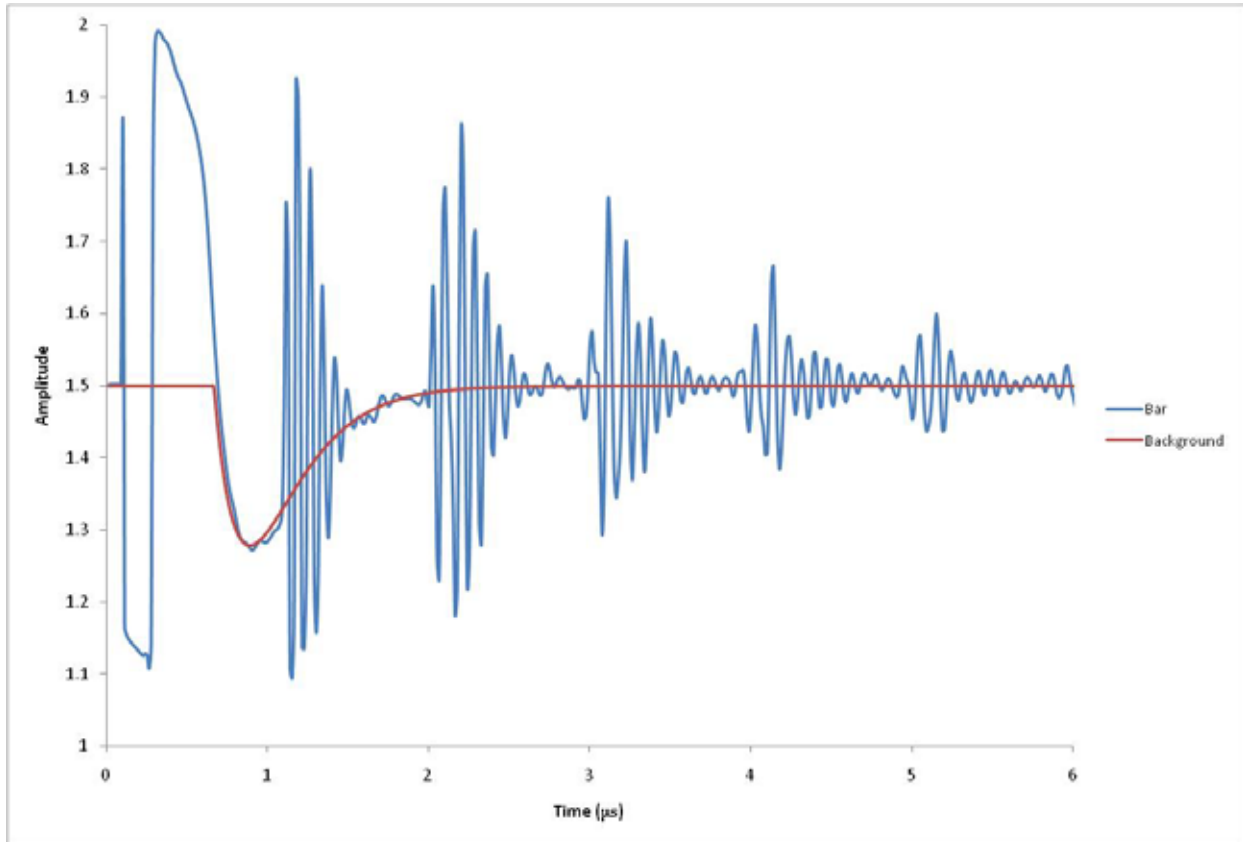
Figure 4.10: Background noise fit to raw data

The fitted background signal was then subtracted from the raw data. It can be seen that the data were centered on an amplitude of 1.5; so after the background was subtracted, the data were shifted down and re-centered on zero, as shown in Figure 4.11. The signal can now be seen clearly. From these data, the thickness of the titanium wear plate could be calculated.
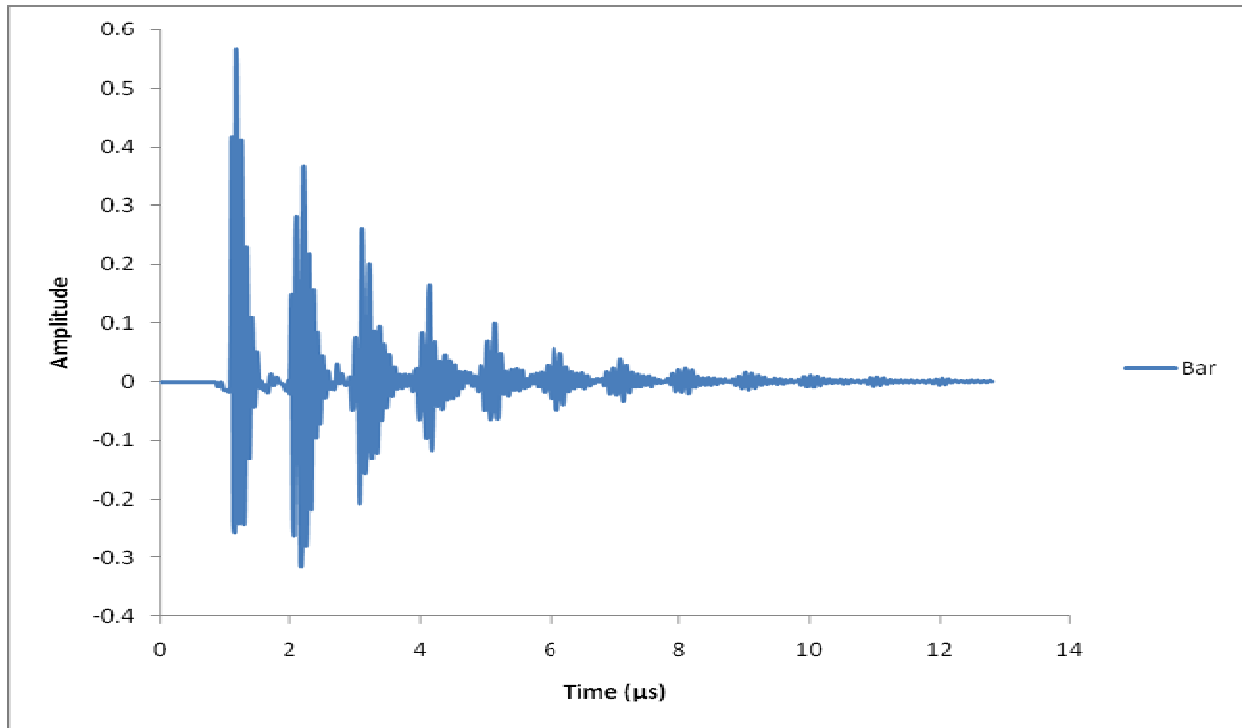
Figure 4.11: Zinc bar data after background noise has been subtracted

These same steps were used to analyze the data obtained from the different zinc sheet samples. Six different data sets were taken and averaged from each sample. Initial analysis began by plotting the raw data obtained by the transducers. Figure 4.12 shows the amplitude vs. frequency of the six different samples. From an initial observation of the graph, it was observed that the signals from the different samples could be separated.
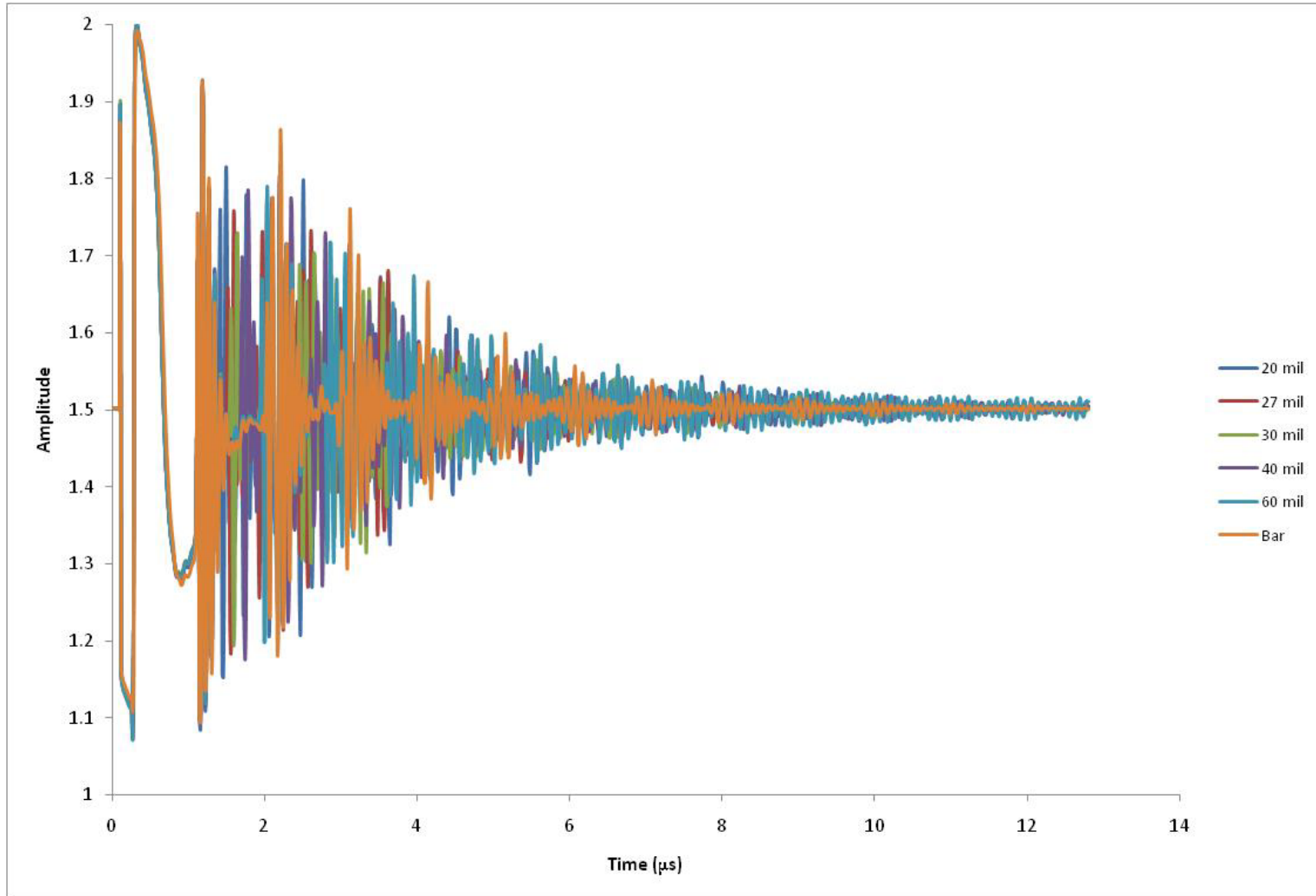
Figure 4.12: Ultrasonic data from all six samples

A zoomed-in plot of the raw data is shown in Figure 4.13. The key information drawn from the plot was that there was a difference between the signals received from the different samples. Further analysis of the data was performed to determine if there were any type of systematic relationship with the TOF and thicknesses of the samples.
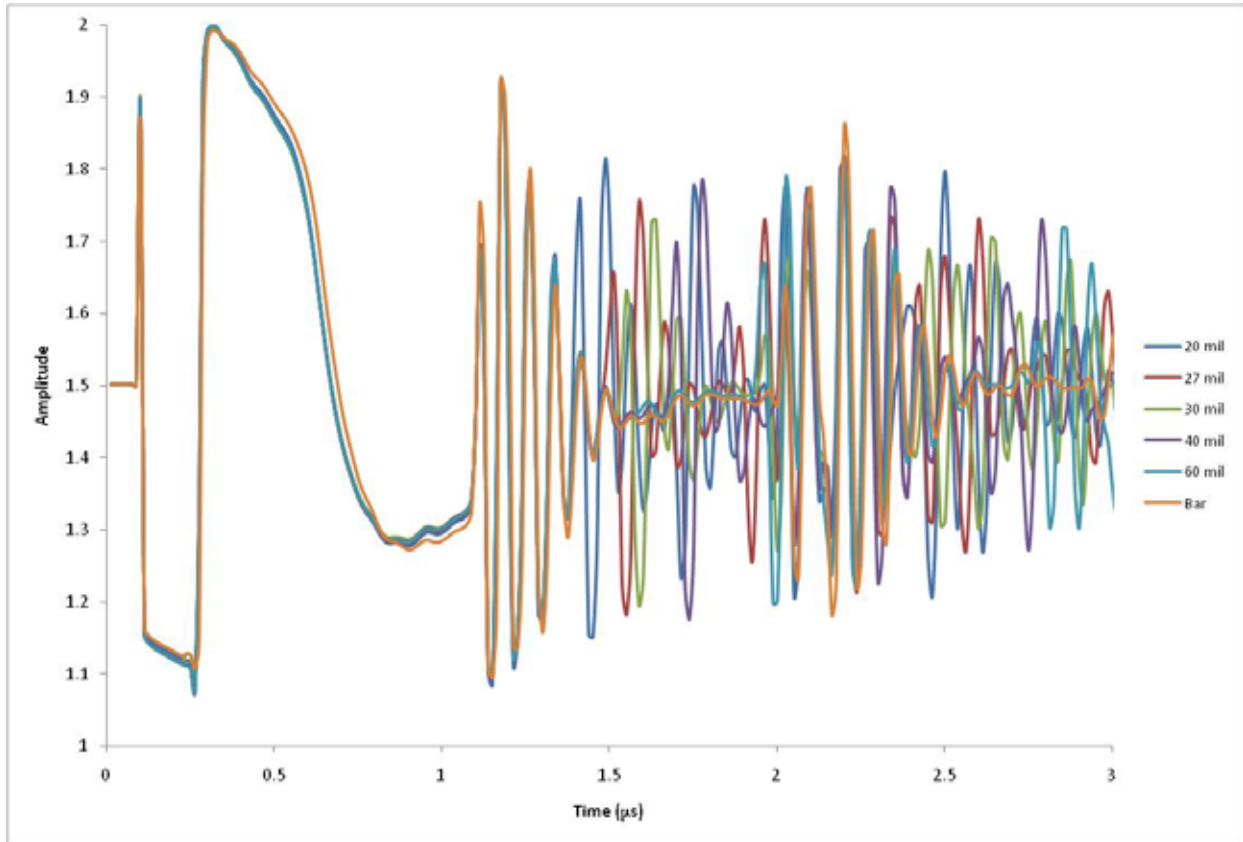
Figure 4.13: Zoomed-in plot of the raw data from six samples

Next the background noise was subtracted from each sample and the data were shifted around zero. Figure 4.14 shows that the first peak, from 1 to 1.4 microseconds, was identical for the six sets of data. This peak represented the signal received from the interface between the Ti wear plate and the zinc surface. To remove this signal, data collected from the zinc bar were used.
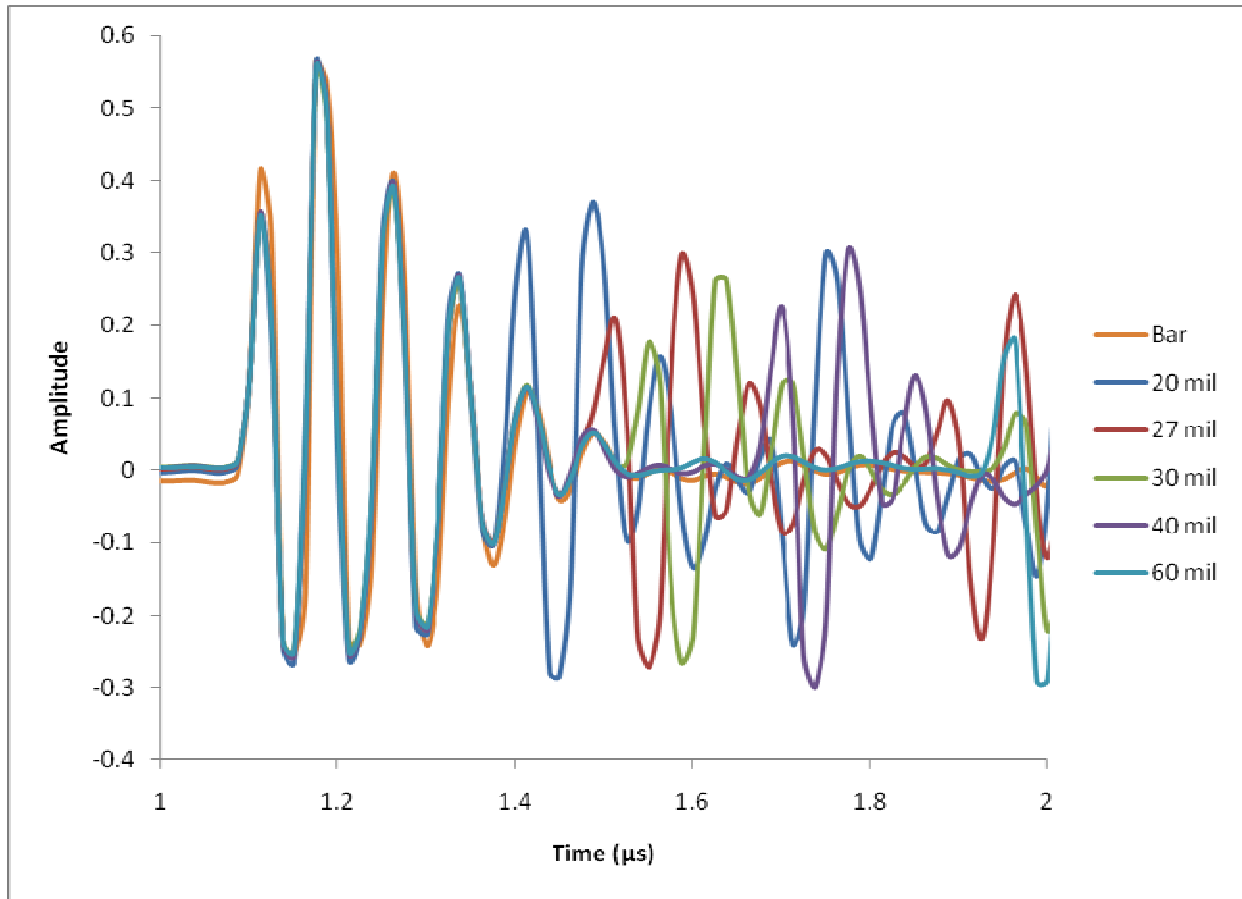
Figure 4.14: Plot of data after background signal has been subtracted

The zinc bar data, sample number six, were subtracted from the raw data. Because the zinc bar was much thicker then the zinc sheets, it was assumed that no signal was reflected from the back side of the sample. By subtracting the zinc bar data from each data set, the remaining signal could be interpreted as the signal received from the back side of the zinc samples. A plot of the data after the zinc bar data were subtracted is shown in Figure 4.15.
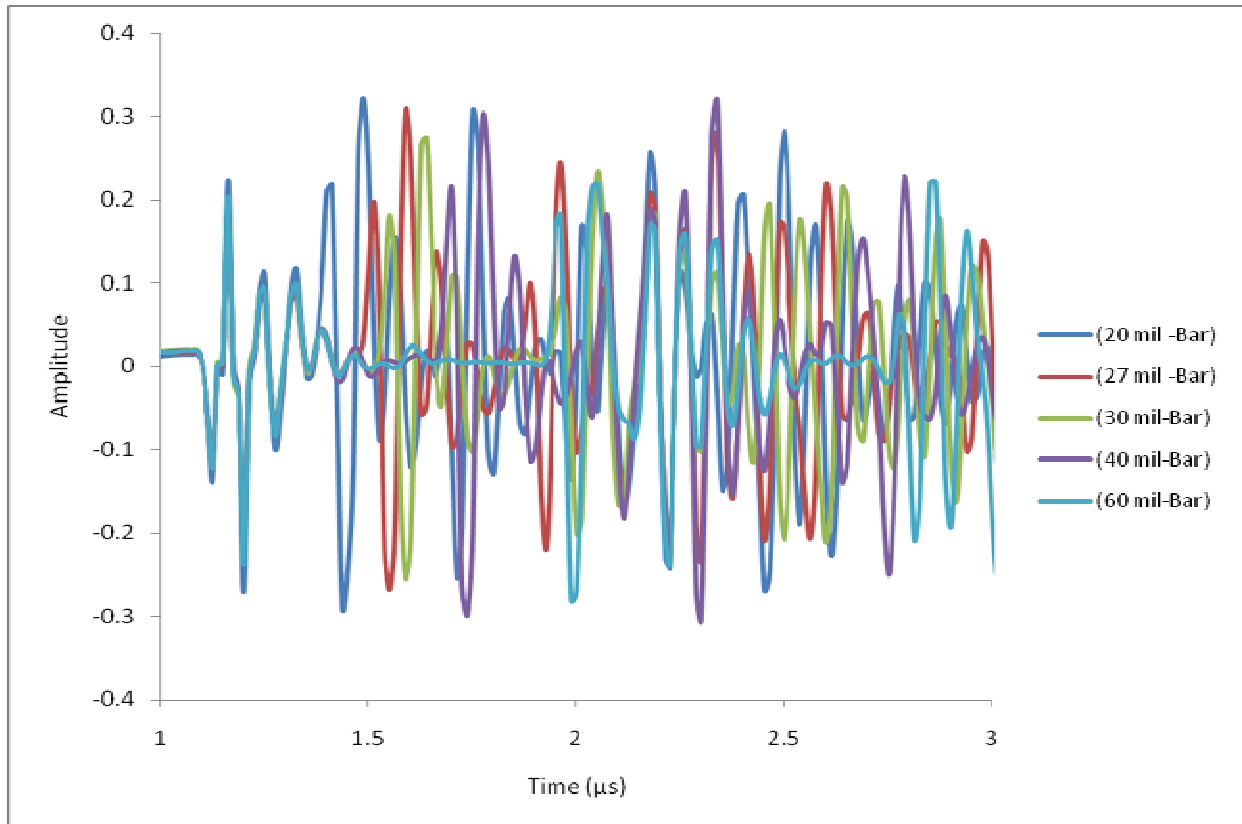
Figure 4.15: Plot of data after the zinc bar data is subtracted

There was still a small signal at the start that could be subtracted out by allowing for a small time shift in the start of the signal. The key observation was that the time at which the new signal was received increased with the increase in thickness of the samples. From this plot the thicknesses of the zinc samples could be calculated.

In the final plot, shown in Figure 4.16, the data from each sample were shifted on the y-axis to better interpret and read the return pulse times. From this plot a technique called time-of-flight (TOF) was used to determine the thickness of each sample. TOF can be used a couple of different ways. It can be used to measure the time it takes for a pulse to reach the detector while traveling over a known distance. This time can then be used to determine the wave velocity of different materials. In these experiements, however, TOF was used in the opposite way, to determine an unknown distance. By measuring the time of the return pulse and using known wave velocities for zinc, the thicknesses of the samples could be calculated.
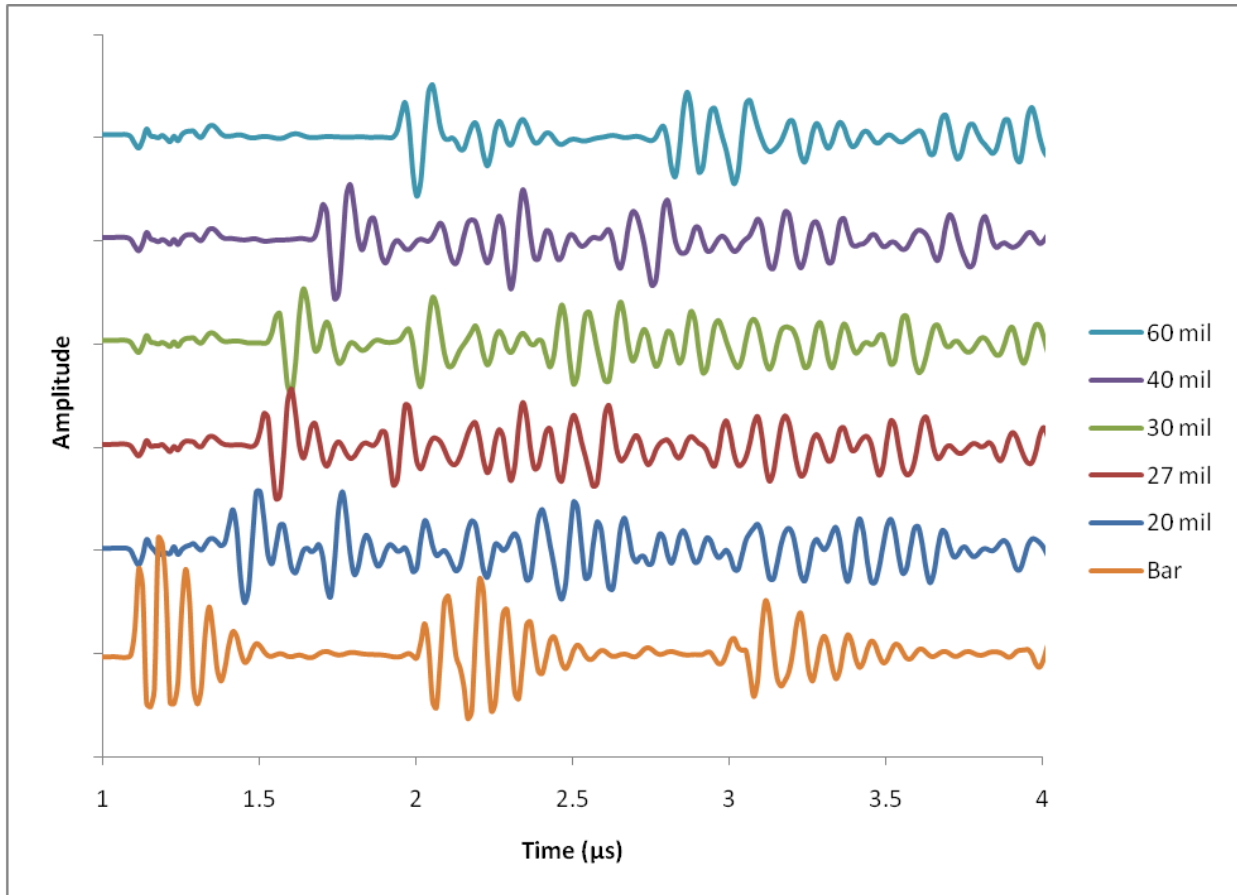
Figure 4.16: Final plot of data shifted up to allow ease of analysis

It can now be seen clearly in Figure 4.16 that, as the samples became thicker, the time it took the signal to arrive at the receiver increased. The zinc bar was assumed to be infinitely thick in comparison to the other samples, so no signal was reflected from the backside of the zinc bar in the time scope of the pulse. The first step in determining the thicknesses of the samples was to record the time it took for the first pulse to return to the transducer. Table 4.1 summarizes the data obtained from Figure 4.16.

Table 4.1: Summary of the pulse return times for each sample

Sample	Pulse Return (μs)	Time Diff. (μs)
Bar	1.1000	0.0000
20 mil	1.3875	0.2875
27 mil	1.4875	0.3875
30 mil	1.5250	0.4250
40 mil	1.6750	0.5750
60 mil	1.9375	0.8375

51

The zinc bar's data represent the time it took the pulse to reach the surface of the zinc samples. To calculate the thicknesses of each of the other samples, each pulse return was measured relative to the zinc bar pulse return. The difference in time represented the time it took the pulse to travel twice the distance of the sample. Because the transducer was also the receiver, the pulse signal needed to travel twice the distance for the signal to return to the transducer. Table 4.2 shows the calculated thicknesses using two different wave velocity values for zinc and a wave velocity calculated by fitting a linear regression to the data.

Table 4.2: Comparison of calculated thickness values of zinc using wave velocity of 4,170 m/s (*Rose 1999*), 3,700 m/s (*Pilgaard 2009*), and a calculated value of 3,592 m/s

Sample Thickness (mils)	Time Diff. (µs)	Thickness (mils) Rose	Thickness (mils) Pilgaard	Thickness (mils) Calculated	Percent Error
20	0.2875	23.63	20.94	20.33	1.649
27	0.3875	31.85	28.22	27.40	1.485
30	0.4250	34.93	30.95	30.05	0.176
40	0.5750	47.26	41.88	40.66	1.649
60	0.8375	68.83	61.00	59.22	1.297

It was assumed that the longitudinal wave velocity of zinc could range anywhere from 3,700 - 4,170 m/s (*Pilgaard 2009; Rose 1999*). An experimental wave velocity in the zinc samples was calculated by plotting the sample thicknesses versus the time differences. By using a best fit line to the data, an experimental wave velocity of 3,600 m/s was calculated (Figure 4.17). Using the calculated wave velocity, calculated thicknesses were within about a 1-1½ percent error of the known values.

It was initially assumed that the ultrasonic wave was longitudinally polarized, but in reality there was a transverse or shear component, because the wear plate was not an infinite plate but a cylinder. The lower wave velocity can be attributed to this mix of longitudinal and transverse components. The transverse wave velocities are generally much lower than the longitudinal wave velocities (*Rose 1999*). It was concluded from this initial set of experiments that the transducers were capable of differentiating between different thicknesses of zinc.

$$T = 3592.2t$$
$$R^2 = 0.999$$
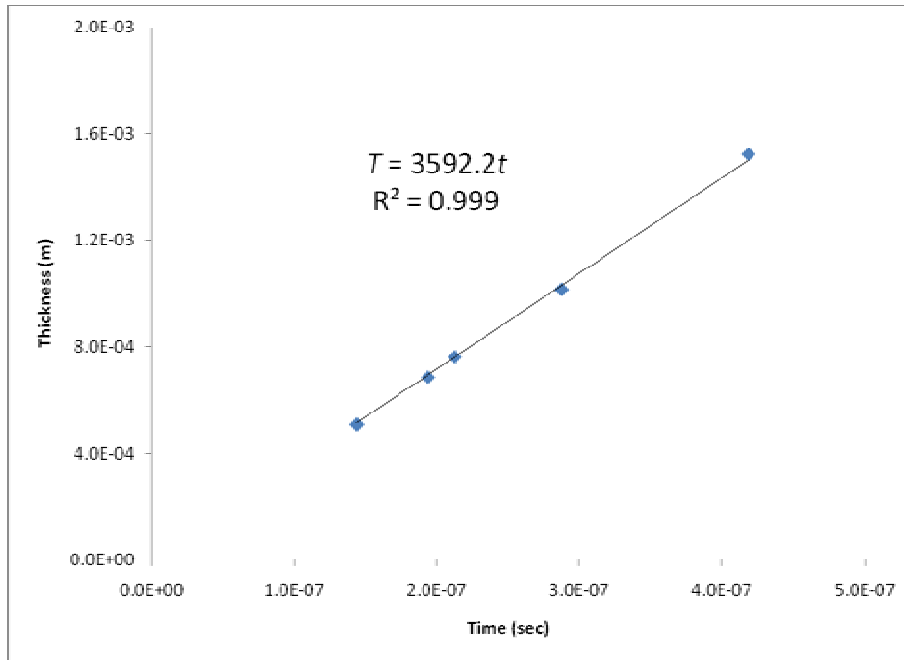
Figure 4.17: Experimental wave velocity plot

4.3 ELECTROCHEMICALLY AGED SAMPLE DATA

In the next step, data were collected from three samples that had been electrochemically aged. Table 3.3 contains general information about these zinc-coated concrete slabs. These samples were constructed with concrete that closely resembled the concrete used in Oregon bridge structures. About 0.5 mm zinc was then thermally sprayed onto each slab, and they were electrochemically aged with a current density of 3 mA/ft^2, approximately 15 times the average current density used on Oregon coastal bridges (*Covino, et al. 2002*). See Chapter 3 for a more detailed description of the electrochemically aged samples.

The same techniques as described in the preceding sections were used to analyze the data collected from the electrochemically aged samples. Figure 4.18 shows the averaged raw data collected for the three different electrochemically aged slabs. Only the 20-year sample is visible in Figure 4.18 since the data sets overlap one another. Unlike the raw data in Figure 4.12, there was no noticeable difference from sample to sample. Another difference between the electrochemically aged samples and the zinc sheet samples was the number of peaks. There were only about three signal peaks before the signal was lost due to attenuation. The amplitude of the signal was also noticeably weaker in the electrochemically aged samples.

An enhancement of Figure 4.18, with the background subtracted, is shown in Figure 4.19. Here it can be seen that there was a slight difference in a few of the peaks, but it was uncertain if the difference was significant enough to draw any conclusion. Based on the results from the model, however, the amplitude versus frequency plot should show some sort of difference between the samples.

53
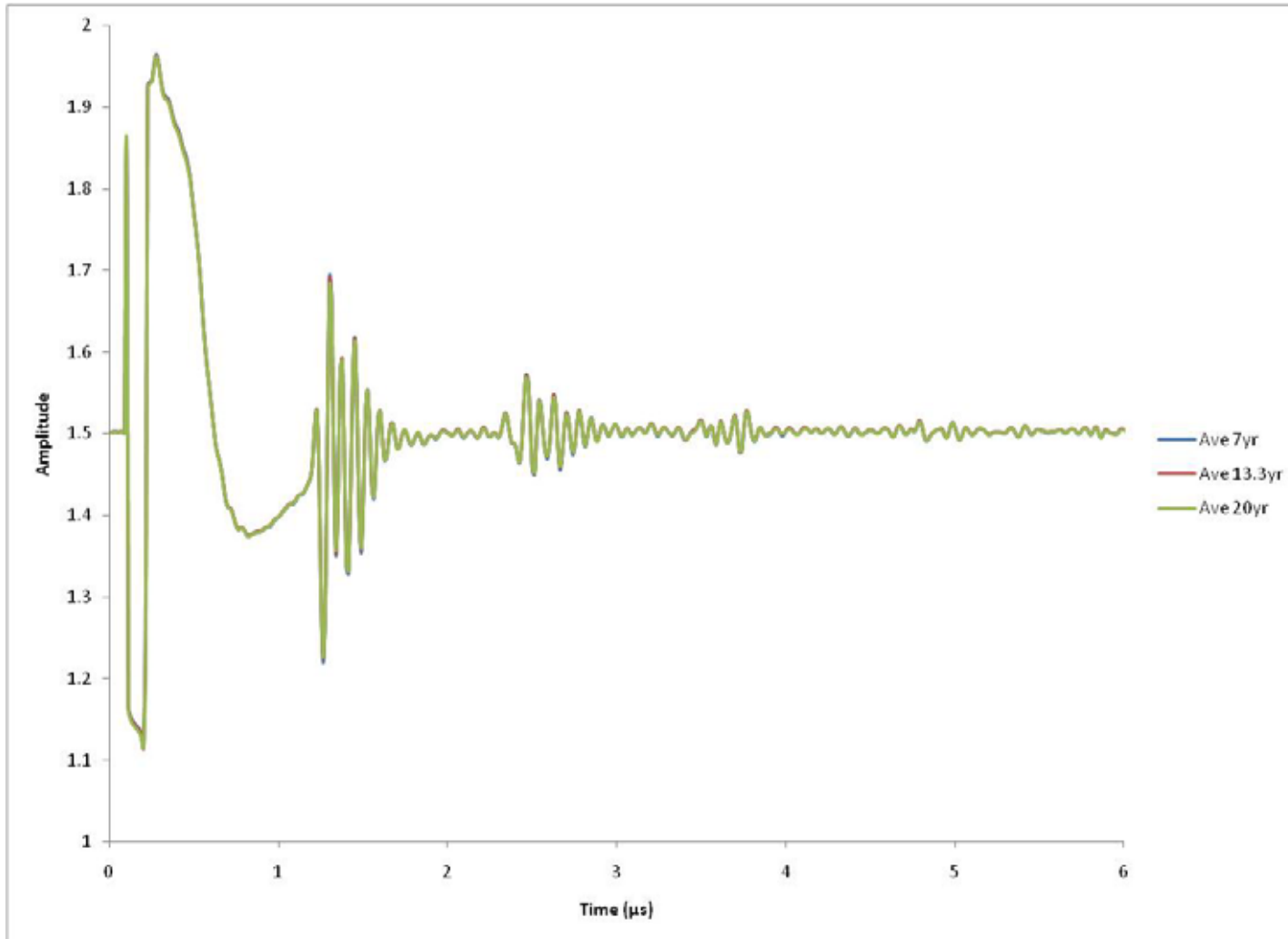
Figure 4.18: Averaged raw data plot of amplitude vs. time of three different electrochemically aged slabs
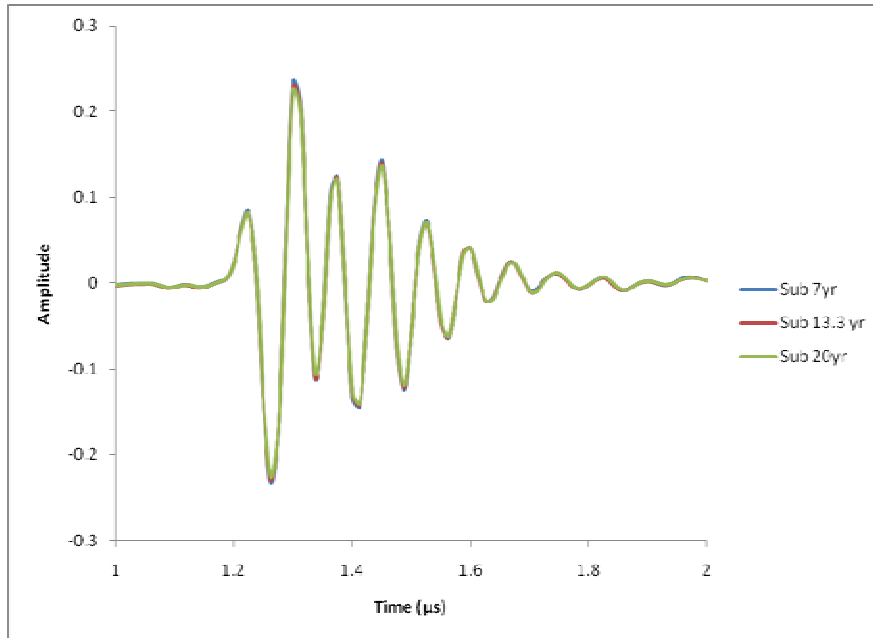
Figure 4.19: Enhanced image of the first peak after the background is subtracted

To convert amplitude vs. time plots to frequency plots, a Fast Fourier Transform (FFT) was performed on the data. This method of analysis was used to decompose a sequence of ultrasonic data into components of different frequencies. The different thicknesses of zinc should result in a change in amplitude at different frequencies. The FFT plot of the background subtracted data is shown in Figure 4.20.
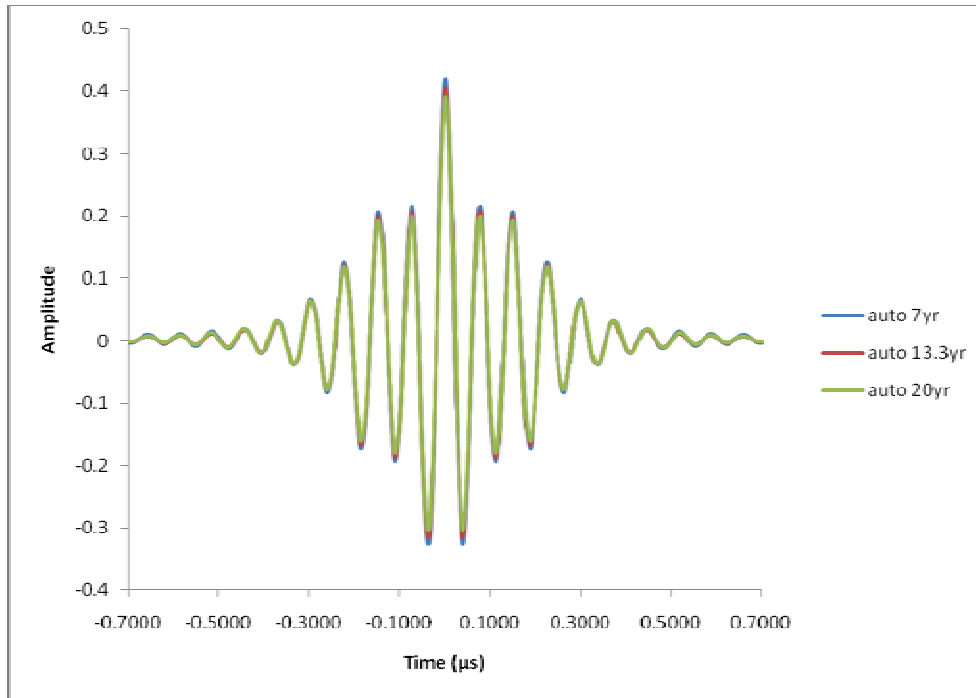
Figure 4.20: FFT of subtracted raw data

At this point in the research, it appeared that the transducer could not tell any difference from one electrochemically aged slab to another. To the transducer each block was identical. It was expected that the FFT plot would show a shift in frequency dependence, a change in amplitude, or a combination of both, but all three samples showed the same frequency dependence. There were slight differences in the amplitude, but this could have been due to poor subtraction of the background signal or the difference in the surface roughness of the samples.

In order to reduce noise an autocorrelation method was applied. Autocorrelation is a mathematical tool used to analyze signal processing data. It is a correlation of the signal with itself and is used to find repeated patterns in a signal, even when such a periodic signal is hidden because of noise. The autocorrelation of the subtracted data, as well as the FFT of the autocorrelated data, are plotted and shown Figure 4.21 and 4.22.
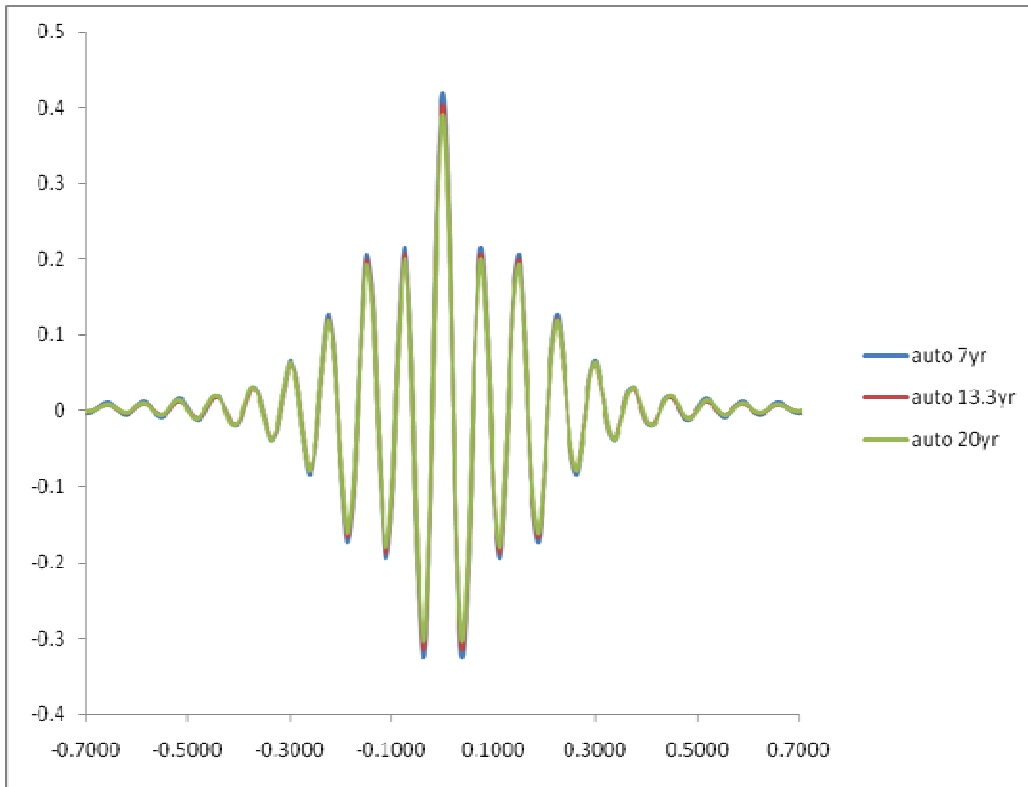
Figure 4.21: Plot of subtracted data after autocorrelation
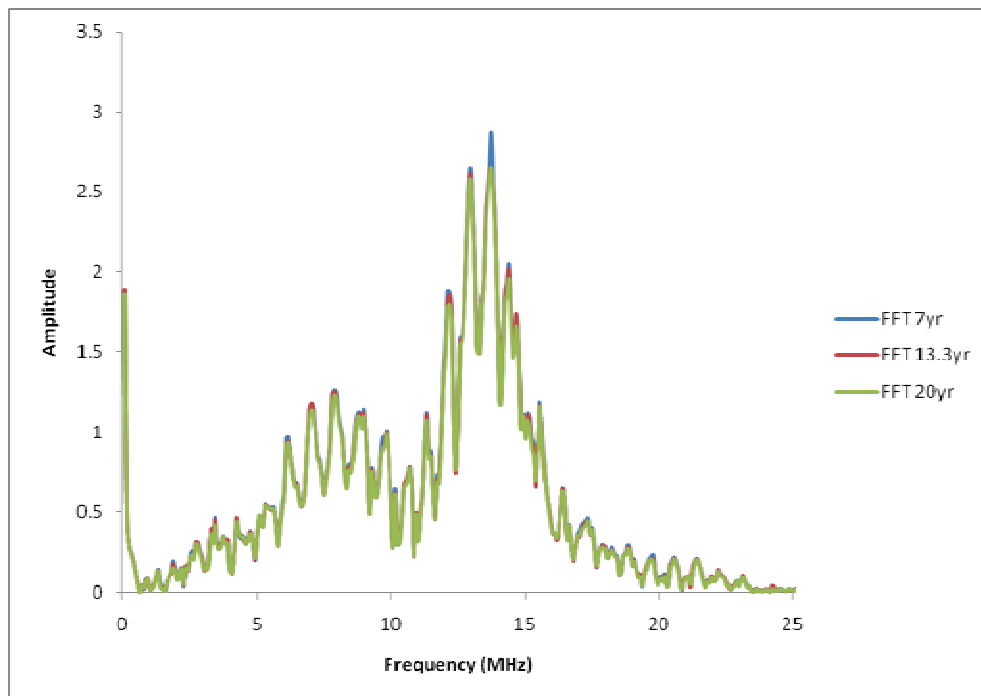
Figure 4.22: Plot of autocorrelation data after FFT

Even after using these analysis techniques, the data showed very little difference from slab to slab. Figure 4.21 shows that after the autocorrelation a lot of excess noise was removed, and it can be seen that the main frequency response for all three samples was from 13 to 14 MHz.

The tests on the electrochemically aged slabs and the subsequent analysis led to the conclusion that no signal was reflected back from the slabs; the waveform shown as output by the instrumentation was the characteristic ringing of the transducer. The signal that was transmitted into the slabs was most likely scattered due to the roughness of the zinc surface, the irregularities of the zinc concrete interface, and the inhomogeneities of the zinc and reaction layers. No attempt was made to investigate further the scattering mechanism.

4.4   UNAGED SAMPLE DATA

The structure of the aged samples was more complex due to the presence of a product layer. In addition, it was unclear if the zinc and the zinc product layer could be distinguished. To eliminate these complicating factors, data were collected from four unaged slabs with zinc anode thicknesses of 10, 20, 30, and 40 mils. The averaged thickness applied to the electrochemically aged samples was 20 mils. First 10 sets of data were collected at a given location and averaged for each block. The background signal was then fit to each unaged sample and subtracted. A plot of the subtracted data is shown in Figure 4.23.
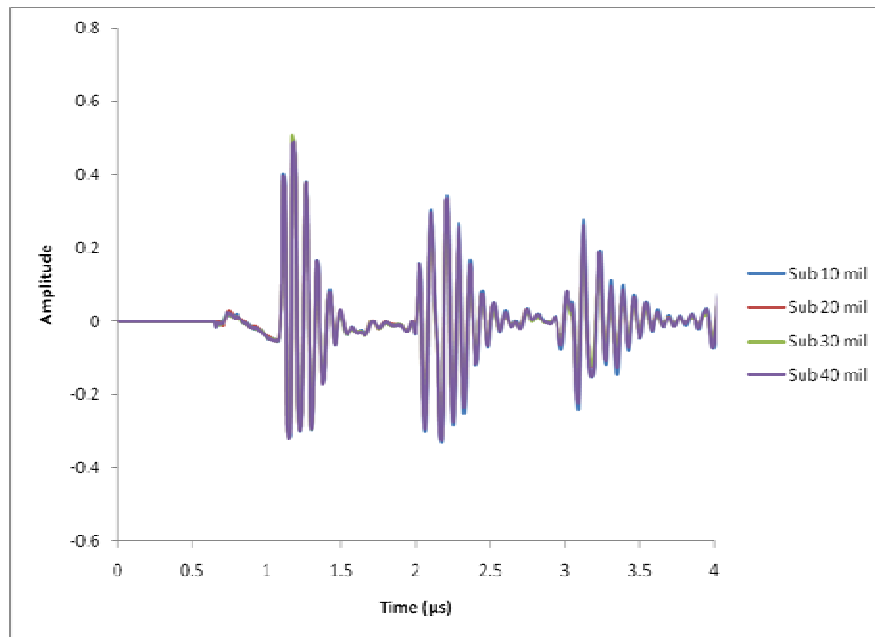
Figure 4.23: Plot of unaged samples after background subtraction

Even with thicknesses of zinc which varied by a factor of four on the samples, the plot showed no difference from sample to sample. With the 40 mil sample it would be expected that the

return signal would be received at a later time compared to the other samples, but all peaks were identical. This finding was contrary to the expectations based on the study of the zinc sheets. Further analysis using the FFT was performed on the subtracted data (Figure 4.24), but the results again showed no significant difference from sample to sample. There were slight differences in the amplitude, but no systematic correlation could be made from it. A comparison of these results to the FFT plot for the electrochemically aged samples showed there was a slight difference in the frequency of the main peak. For the unaged slabs the frequency shifted back and centered around 13 MHz.
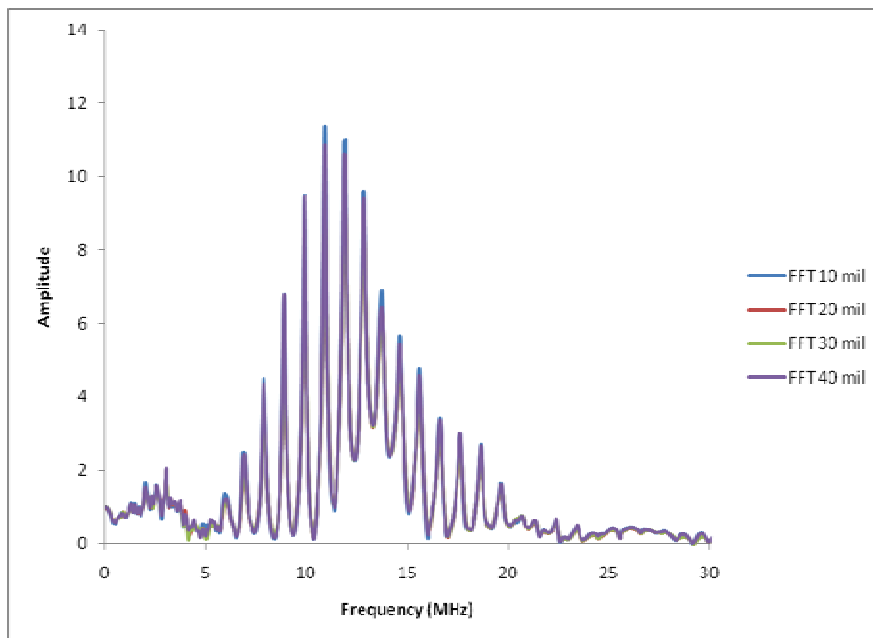
Figure 4.24: Plot of unaged samples after FFT of subtracted data

The next step in analyzing the data was to perform an autocorrelation and an FFT on the autocorrelated data. As shown in Figure 4.25, in the autocorrelated plot there were small differences in the amplitude of the signal. The problem was that the 10 and 40 mil samples resembled one another, and the 20 and 30 mil samples resembled one another. There was no systematic relationship that could be seen as the zinc anode became thicker.
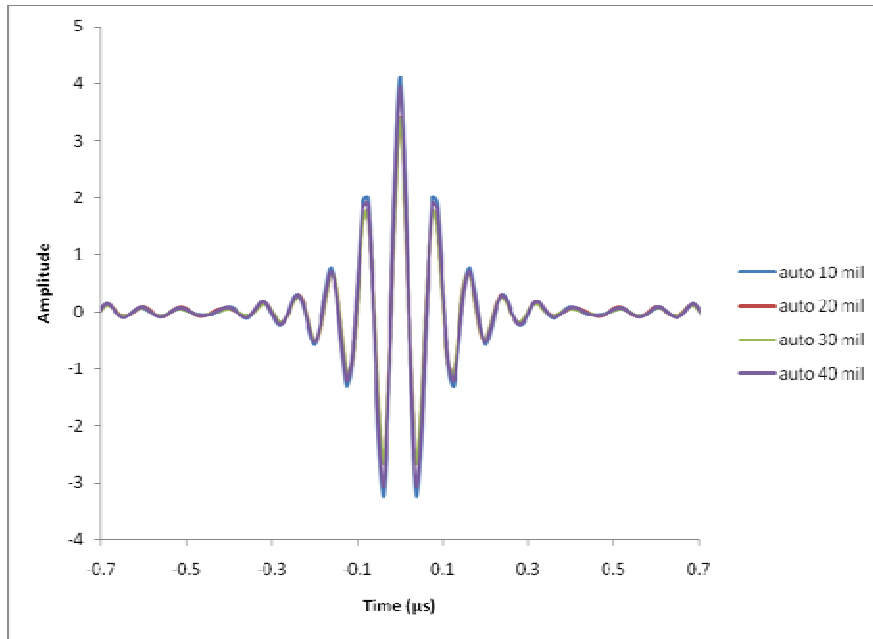
Figure 4.25: Plot of autocorrelation data for unaged samples

The FFT of the autocorrelated data (Figure 4.26) showed that the unaged samples had their main frequency response around 13 MHz. The problem was that all of the samples had the same frequency response and that the difference in thickness had no effect on the FFT plot.
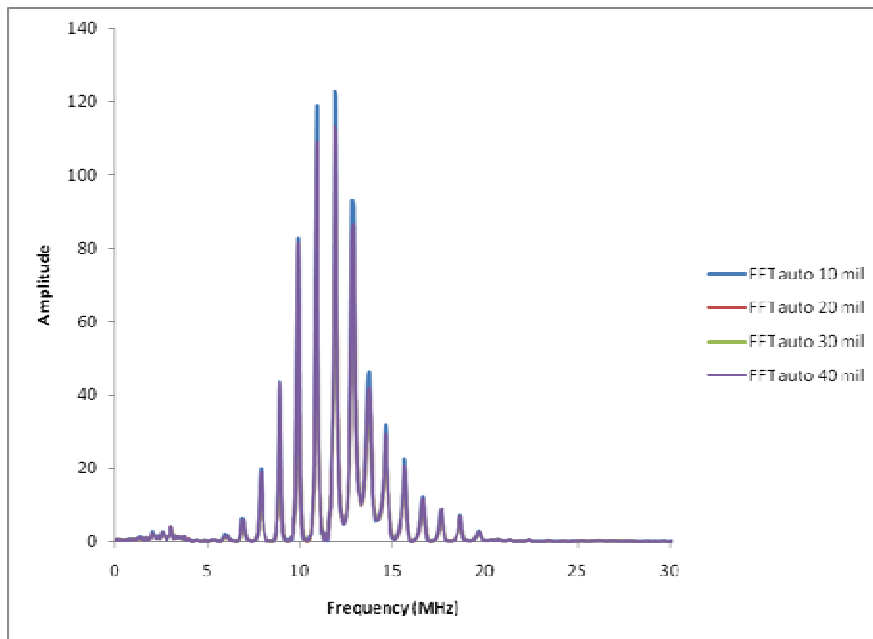
Figure 4.26: Plot of FFT of the autocorrelation for the unaged samples

A comparison between the 40 mil zinc sheet, 40 mil unaged slabs, and the zinc bar is shown in Figure 4.27. Each data set showed a signal from 1 to 1.5 microseconds, representing the signal reflected at the zinc surface. It was expected that the signals for the two 40 mil samples would be similar, but there was a clear difference between these two samples. The 40 mil zinc sheet sample had an addition signal that was received by the transducer at about 1.7 microseconds. This part of the signal was the return signal from the back side of the zinc sheet. It was noted, however, that the 40 mil unaged block closely resembled the zinc bar. From this finding it was assumed that there was no return signal from the back of the zinc layer in the unaged samples, which would explain why all the unaged samples were similar. The signal that was transmitted into the surface of the zinc was believed to have been lost or deteriorated due to scattering of the signal. It is hypothesized that the signal was scattered due to the interface roughness of the samples or their microstructure, and that the scattering occurred at either the zinc-to-concrete interface or within the zinc itself.
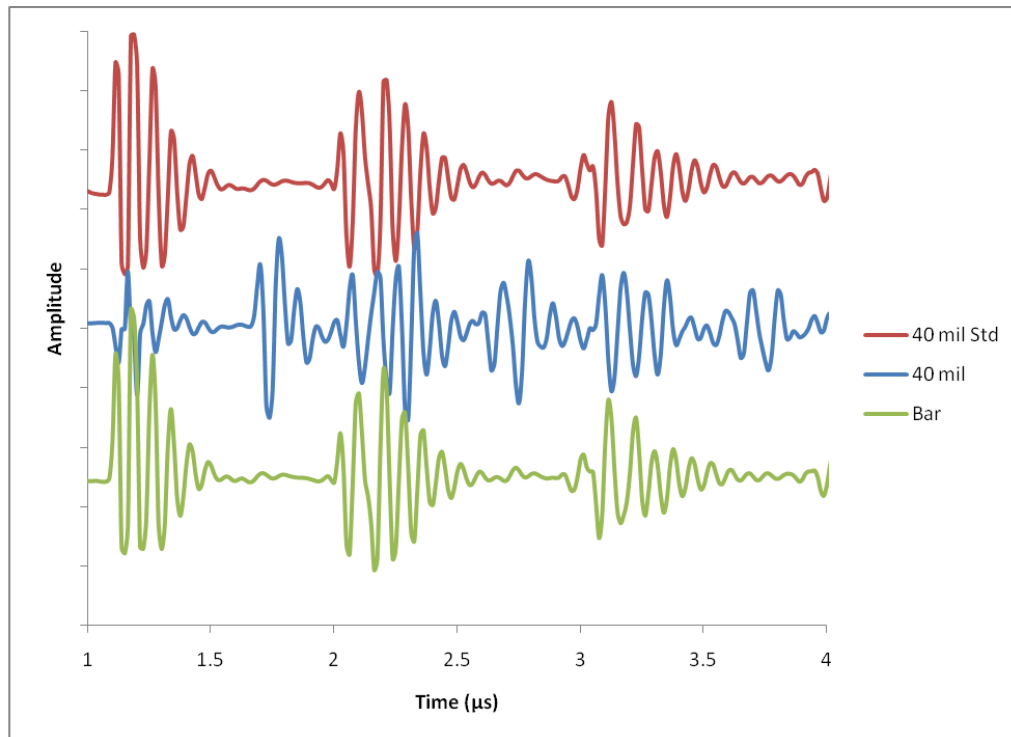
Figure 4.27: Comparison plot of three different samples

It was concluded that the transducers were only capable of distinguishing the difference in the zinc sheet samples.

To try to determine where the signal was lost, the outer surface of an unaged thermal sprayed zinc sample was sanded/polished to try to decrease the roughness. The same types of analysis were used on the sanded sample data and are shown in Figures 4.28 and 4.29. The three sets of data were collected after three successive rounds of sanding/polishing at the same location. Each

61

set is of data was an average of four separate runs. The goal in polishing the zinc surface was to reduce scattering at the transducer-to-zinc interface and to allow more signals to be transmitted to the back side of the zinc anode. In theory, as more and more zinc was removed by sanding, the time it took for a signal to return from the back side would shorten, and additional signals would be received by the transducer.
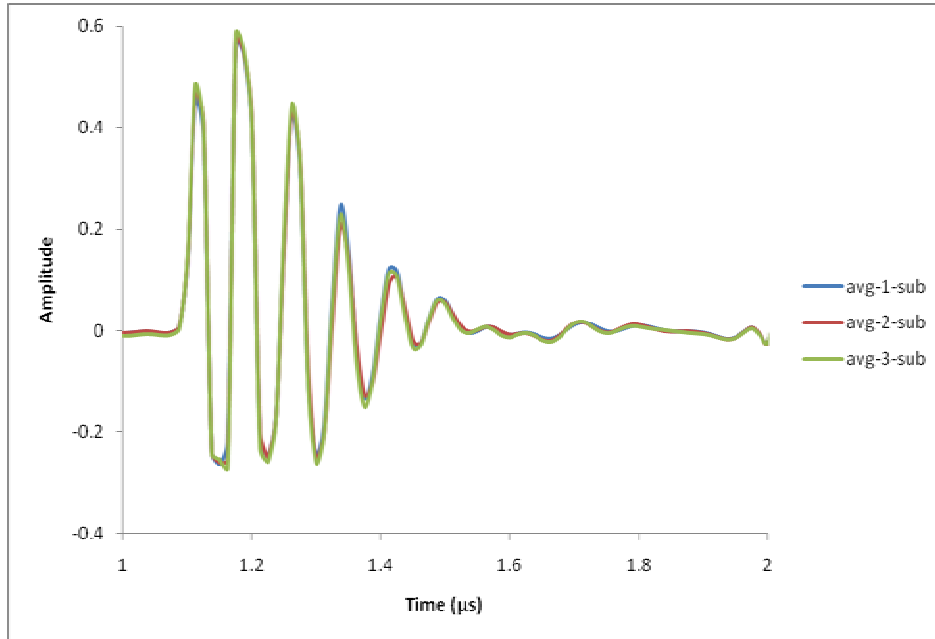
Figure 4.28: Plot of unaged samples after each polishing step
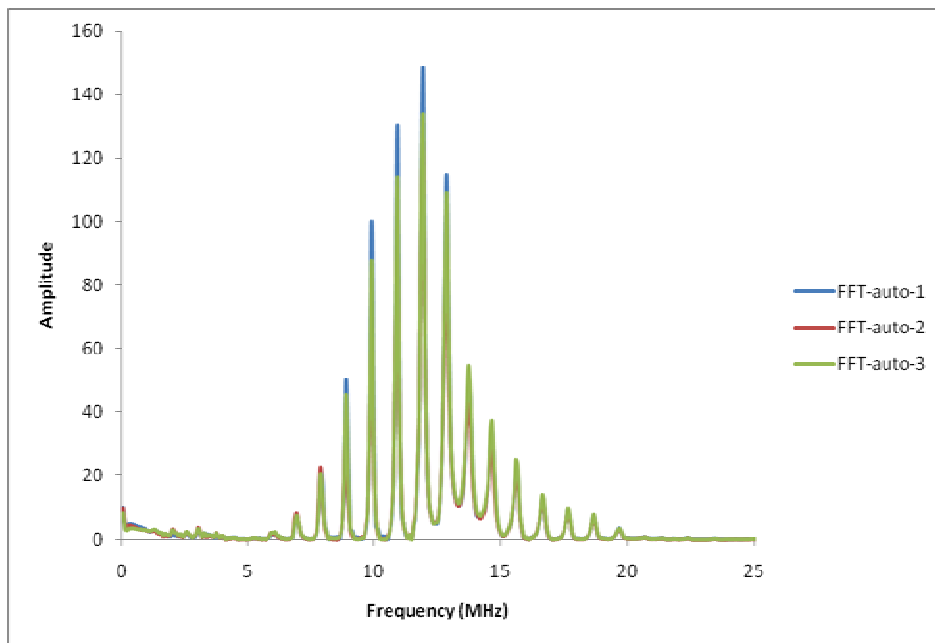
Figure 4.29: Plot of FFT after autocorrelation for the polished sample

There were slight differences in the amplitudes, but no additional signals were seen after 1.5 microseconds. Even after polishing the surface of the unaged samples, the data still resembled the data collected from the zinc bar. The ultrasonic signal was still lost. Therefore, it was concluded that the major scattering occurred at the zinc/concrete interface. The roughness of the concrete surface was believed to cause the ultrasonic pulse to be reflected in different directions. Figure 4.29 shows a schematic of the interface of the zinc/concrete interface.
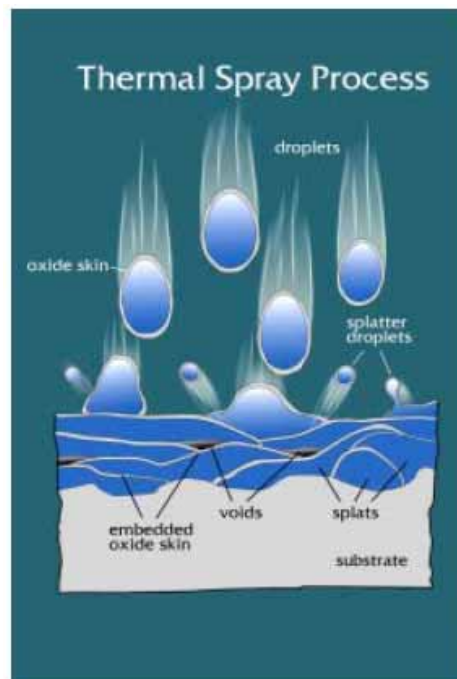
Figure 4.30: Schematic representation of thermal spraying showing the splat (droplet) impact and coating formation processes (*Covino, et al. 2002*)

A alternative cause for the signal being scattered could be what ODOT refers to as "splat." The zinc anode is constructed by the application of multiple zinc droplets. As the schematic shows, numerous interfaces form as each droplet solidifies. While TS zinc is not believed to form an embedded oxide skin, micro-voids are also formed during the application of the zinc anode. These imperfections in the zinc anode can cause the signal to be scattered soon after it is transmitted by the transducer. Because the signal is scattered, it would be similar no matter what the conditions of the samples were.

 At NTT Access Network Service Systems Laboratories, ultrasonic techniques are being used to inspect cracking, voids, and other defects in reinforced concrete structures (*Irie, et al. 2008*). They have developed a macroscopic ultrasonic method that suppresses noise by sequentially irradiating pulses from the transducer as it is moved along the test sample. The desired waves of interest can be isolated after using a frequency filter to detect arbitrary component waves and using an averaging procedure that averages several thousand pulses. A schematic of the system

is shown in Figure 4.31. The frequency of the transducer, the sampling rate and the techniques used are not known.

The NTT work shows that scattering in the layer can be averaged out to show the signal reflected from the back surface. Since the authors of the current research did not see any signal at all from the back surface, however, averaging of the signals observed would not have improved the data. If the interface roughness were reduced, a similar method could be developed for analyzing the zinc anode, and scattering issues inside the zinc layer could be resolved.
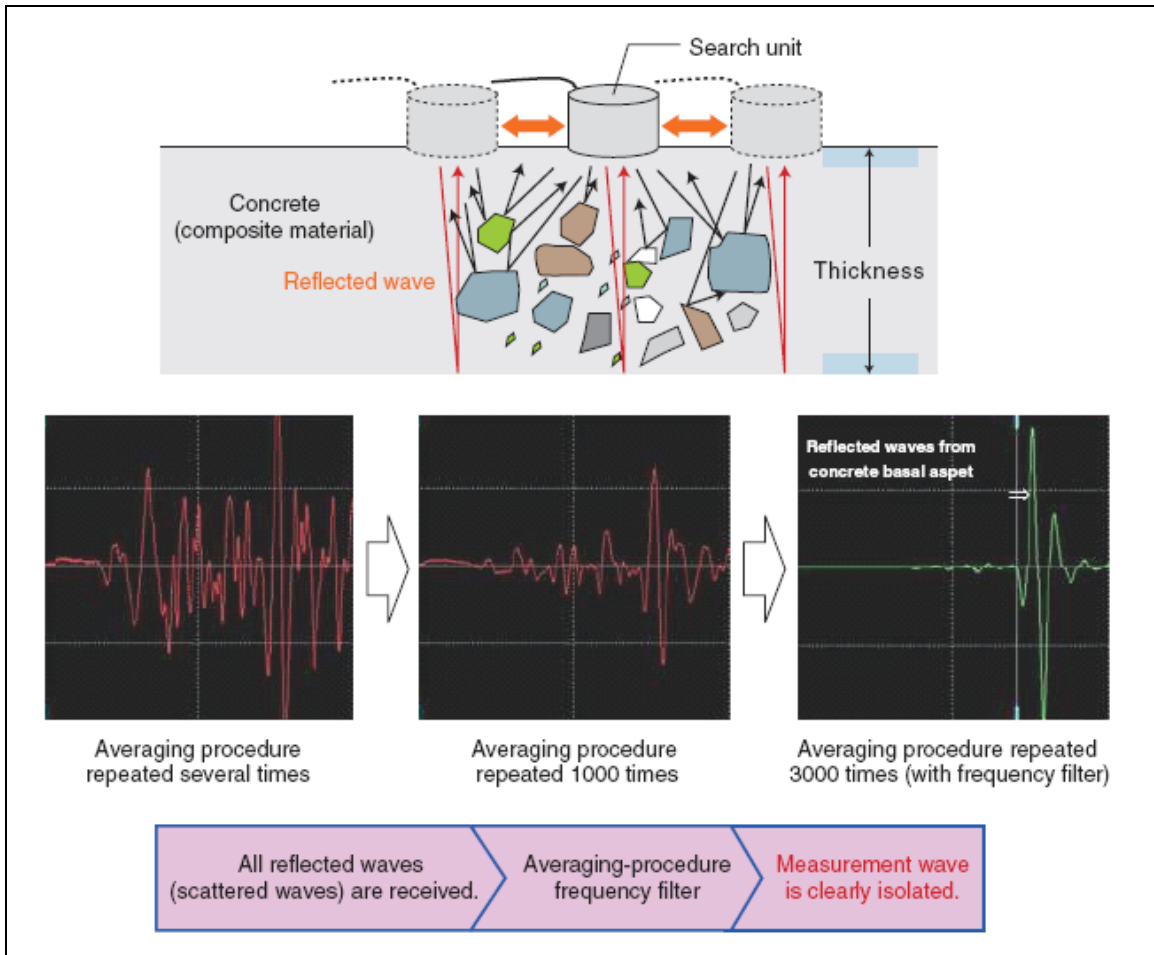
Figure 4.31: Overview of macroscopic ultrasound method and example of waveform obtained during concrete thickness measurement (*Irie, et al. 2008*)

Figure 4.32 shows a Fourier transform from the reflected ultrasound waves in the NTT system. The graph indicates that as the amount of corrosion on the reinforcing bars increases, the amplitude of the reflected wave is weaker across a specific frequency band. It should be noted, however, that the sample sizes are on the order of 200 millimeters compared to the TS Zn 0.5 millimeter samples in this research. This allows for a higher wavelength and lower frequency

transducer. Also, because of the difference in wavelength, what may be interpreted as a rough surface by the ultrasonic measurement system in this research may not be interpreted as rough by the NTT system.

Fig. 5.   Ultrasound spectra of sound waves reflected off reinforcing bars.
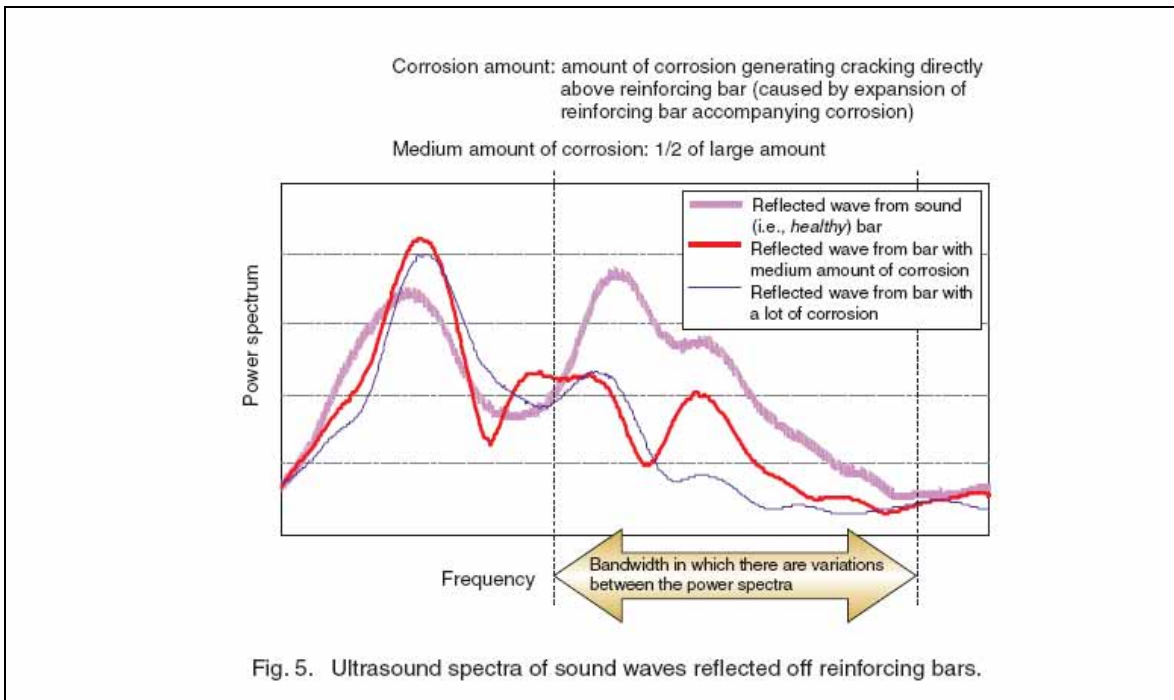
Figure 4.32: Ultrasound spectra of sound waves reflected off reinforcing bars (*Irie, et al. 2008*)

5.0   RESISTANCE/PERMEABILITY TESTING

In this chapter, results of dry and wet resistance measurements using cyclic voltammetry are presented. The samples, described in Chapter 3, contained 3 kg NaCl added per m^3. Accelerated aging was performed by NETL in a different project with a constant current density of 32 mA/m^2 (*Covino, et al. 2002*). Dry samples were tested to determine if a relationship could be found between the circuit resistance and the electrochemical age of the sample. Measurements were conducted on the electrochemically aged samples of 0, 1.8, 3.2, 8.2 and 14.3 bridge years. The second method of testing, a resistance/permeability hybrid, was performed to determine the dynamic electrical response after water was applied to the zinc surface. Samples of 1.8 and 7.4 bridge years were tested.

The rationale for pursuing these dynamic measurements follows. In previous work, it has been observed that with accelerated electrochemical aging the interfacial layer between zinc and the concrete begins to dominate the CP circuit resistance (*Orlova, et al. 1999*), and that it may contain two phases, a phase with high water solubility and a phase with low water solubility (*Rehani 2000*). It is hypothesized that the resistance of the blocks is proportional to the extent of product layer that forms at the zinc/concrete interface. As the concrete blocks are aged, more products are formed, resulting in an increase in resistance. Moreover, the resistances of the soluble and insoluble phases can be modeled by parallel resistances, as shown in Figure 5.1. For simplicity, the reactive component of the circuit in Figure 5.1 has been omitted. Figure 2.6 shows that the Fe vs. Zn potential reaches its most positive value (i.e., smallest in magnitude) after the block is sprayed, presumably when the soluble phase is dissolved. As the interfacial layer dries, the absolute value of the potential increases. The basis for the wet resistance/permeability hybrid is on the dynamics of the dissolution of the soluble product layer. The response of the product layer should be characteristic of the amount of zinc that has oxidized and reacted in the interfacial region, and may, therefore, be used to characterize the condition of the zinc anode.
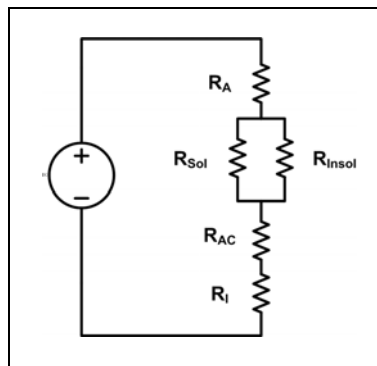
Figure 5.1: Equivalent circuit of the electrochemical system, where R_A is the anode, R_{Sol} is the soluble portion of the product layer, R_{Insol} is the insoluble portion of the product layer, R_C is the concrete, and R_I is the iron mesh

The dry resistance testing was performed on a set of five different electrochemically aged blocks. Cyclic voltammetry was used, with each block undergoing three cycles between a maximum potential of E_{OCP} +30 mV and a minimum of E_{OCP} −30 mV, where E_{OCP} was the open circuit potential. Unless otherwise stated, scan rates of 5 mV/s were used.

A representative plot of current vs. potential is shown in Figure 5.2, with potential reported as Zn vs. Fe and positive current representing an anodic process on the zinc electrode. The data from the part of the cycle where the voltage was decreasing, i.e., becoming more negative, was recorded as blue diamonds and labeled "down." Conversely, measurements made as the voltage increased was recorded as red squares and labeled "up." Best fit lines for these parts of the cycle are also shown. This result was typical of all responses recorded, with the current for the up cycle being slightly more positive than the down cycle. From these data the resistance of the concrete block was calculated by taking the inverse of the slope of the best fit line. For example, the resistance in the block in Figure 5.2 was 270 kΩ.

To explore the variability of resistance measurements, data were collected daily for approximately two months. Each day, three voltammegrams were collected on each of the five aged blocks, at approximately 9 AM, 12 noon, and 3 PM. Temperature and relative humidity were also recorded.
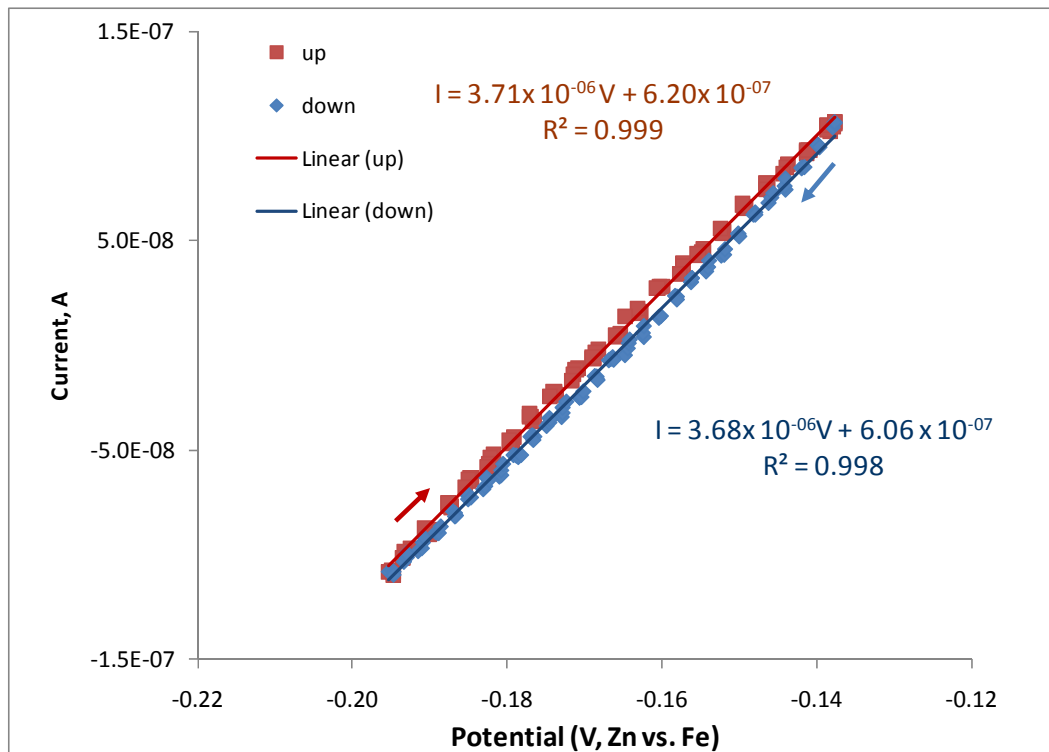
Figure 5.2: A general current versus voltage plot acquired from cyclic voltammetry. This block is unaged.

Figure 5.3 plots the resistance vs. time for the 5 samples. Generally the unaged sample (0 bridge years) had the lowest resistance, and the measured resistance increased with electrochemical age. For a given block, there was noticeable variability in the resistance with time. However, the change in resistance of any given block followed that of the other blocks; therefore, it is believed that environmental factors were the primary cause of the variability.
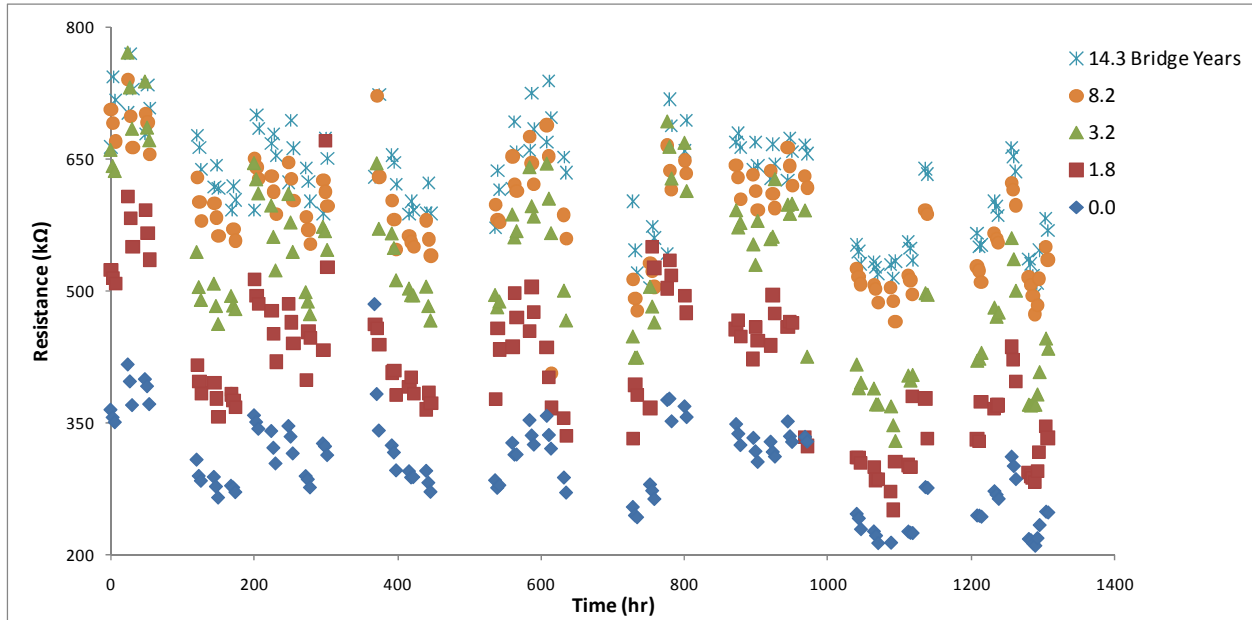
Figure 5.3: Daily resistance data vs. time collected for five different electrochemically aged blocks

Figure 5.4 shows a plot of the average of the resistance data collected over the course of the experiment (shown in Figure 5.3) vs. electrochemical age. Also plotted are bond strength measurements from these blocks (collected by *Covino, et al. 2002*). There were two regions observed in the response for the dry blocks. Initially, up to about 5 bridge years, the resistance increased rapidly, followed by a much more gradual increase, or a plateau. The transition between the two regions occurred roughly around the maximum bond strength.
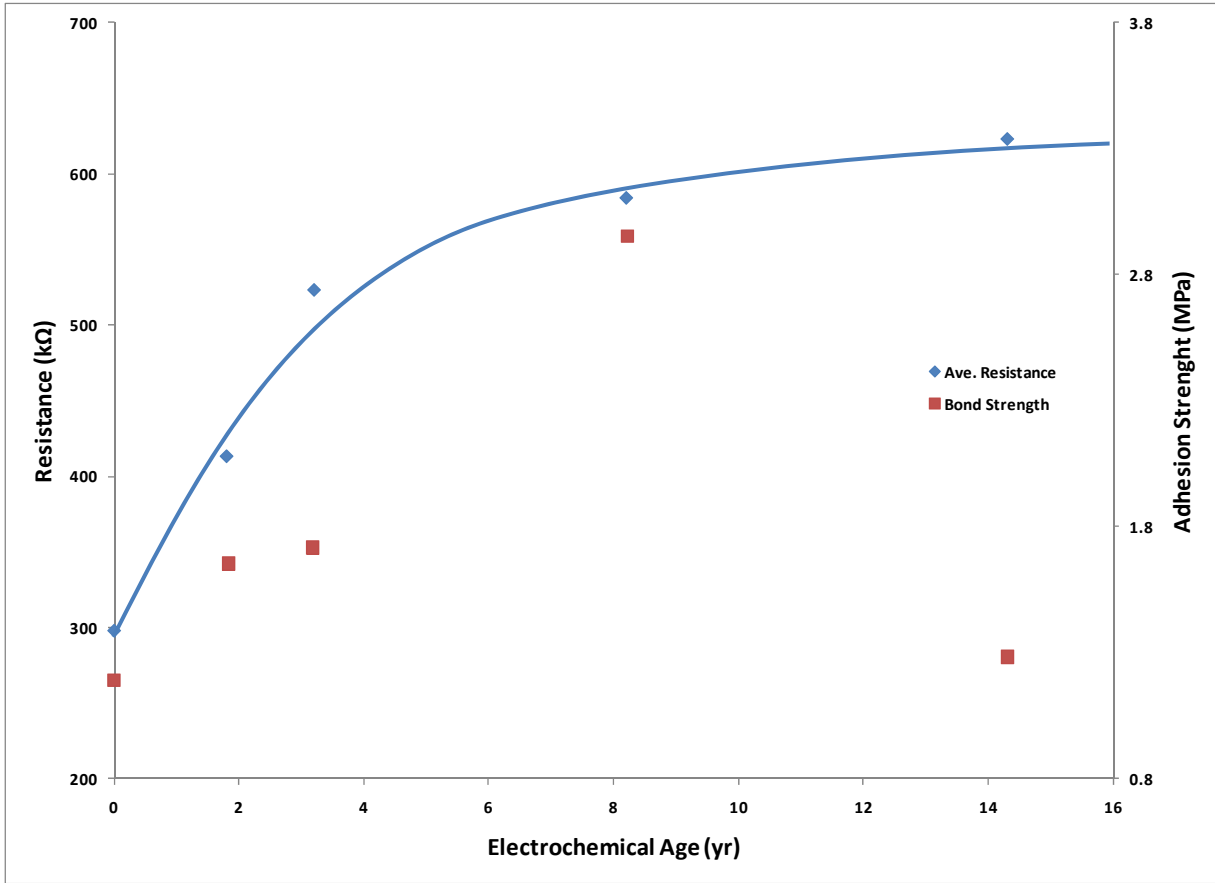
Figure 5.4: Plot of average resistance (left axis) and bond strength (right axis, from Covino, et al. (*2002*) vs. electrochemical age of the samples

The anodic reaction at the zinc concrete interface is a series of complex chemical processes which are spatially heterogeneous and can be thought of in several different ways. One simplified reaction sequence is as follows. Zinc metal oxidizes at the anodic interface to form zincate:

$$Zn^0 \rightarrow Zn^{2+} + 2e^-$$
(5-1)

Zincate reacts with hydroxide ions to from a solid.

$$Zn^{2+} + 2OH^- \rightarrow Zn(OH)_2(s)$$
(5-2)

While Reaction 5.2 is shown as solid zinc hydroxide for simplicity, there can be varying degrees of hydration leading to a mixture of oxides and hydroxides. To a lesser degree other anions can also react with Zn^{2+}. The Zn reaction products can undergo secondary mineralization reactions such as the following:

$$Zn(OH)_2(s) + CaSiO_3(s) \rightarrow ZnSiO_3(s) + Ca^{2+} + 2OH^-$$

$$\text{(5-3)}$$
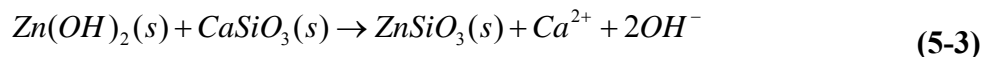
If Reactions 5.1, 5.2 and 5.3 are added together, the following overall reaction is obtained:

$$Zn^0 + CaSiO_3(s) \rightarrow ZnSiO_3(s) + Ca^{2+} + 2e^-$$

$$\text{(5-4)}$$
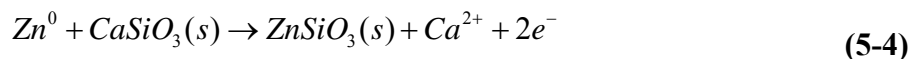
The increase in average resistance shown in Figure 5.4 correlates to the growth of the zinc product layer, and more specifically to the NETL-defined "zone 1" where the zinc oxide hydroxide layer is formed. On the other hand, if Reaction 5.4 is viewed as the oxidation half reaction, with an electrode surface that grows with aging, then the increase in resistance can be viewed as part of an electrode process.

It was observed that the daily resistance changes of the blocks tended to decrease through the day. For example, representative values of resistance from three days during the experiment for the unaged block are shown in Figure 5.5 (red squares). Figure 5.5 also plots the corresponding laboratory temperature (blue diamonds). As the temperature increased during the day, the resistance decreased. This trend was consistently observed on all blocks throughout the experiment. To investigate the temperature dependence further, blocks with electrochemical ages of 1.8 and 0 bridge years were placed in a refrigerated unit. Data were collected at different temperatures, as measured on the block surface when it was removed from the refrigerator. Figure 5.7 shows a plot of resistance vs. temperature (squares) for cooled blocks. Resistance data from Figure 5.3 (not cooled) are plotted for comparison. As the temperature lowered, approaching the freezing point of water, the resistance noticeably increased.
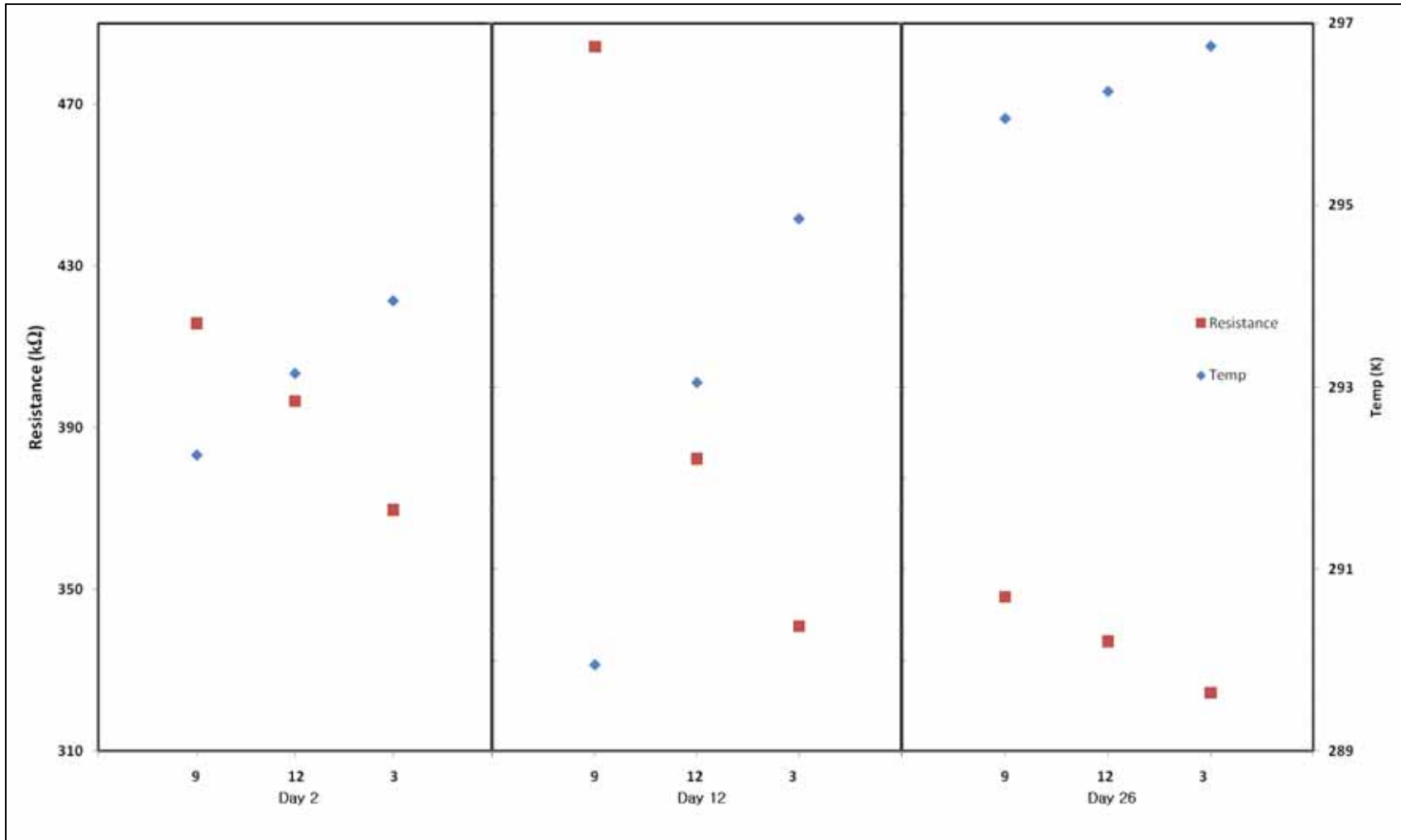
Figure 5.5: Daily resistance and temperature versus time
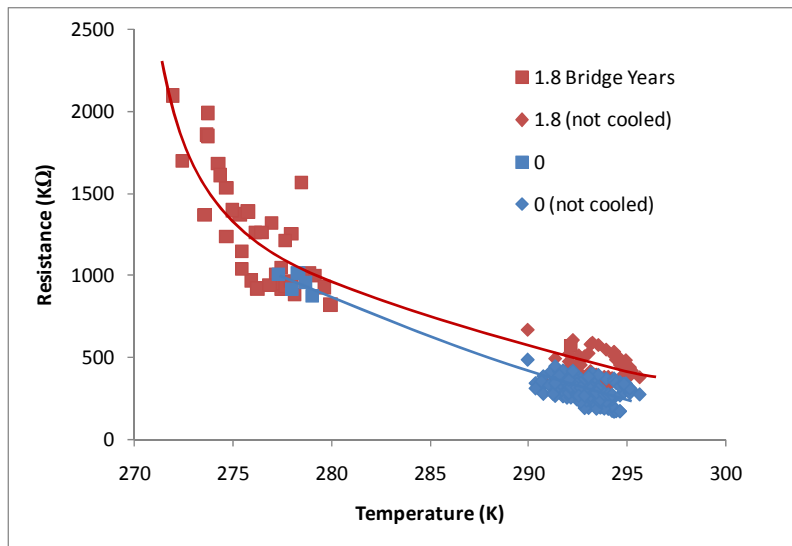
Figure 5.6: Resistance vs. temperature for blocks of 0 and 1.8 bridge years

The circuit resistance tended to decrease as temperature increased. This trend was consistent with the transport of ions in the electrolyte in the pores controlling the current. As the temperature increases, the viscosity of the electrolyte decreases. This decrease in viscosity correlates to an increase in conductivity, and consequently a decrease in resistivity (*Robinson and Stokes 1959*). However, other mechanisms can also lead to the observed behavior. For example, if an electron transport surface reaction were controlling, a similar temperature dependence could be realized.

Figure 5.7 shows the open circuit potential, E_{OCP} (Zn vs. Fe), for the different blocks. The open circuit potential was the most positive for the unaged sample, around -160 mV, and it decreased with age until 8.2 bridge years. The block that had aged 14.3 bridge years then showed an increase in E_{OCP}. The variation was considerably less than in the resistance data shown in Figure 5.3.

To determine the influence of each metal electrode on E_{OCP}, a three electrode configuration was used, with a saturated calomel reference electrode mechanically attached to the concrete through a sponge. The sponge was wetted with 1 M NaCl solution and squeezed to remove excess water. The potential was measured with the reference electrode placed in several regions where the zinc had been pulled from the concrete surface. This measurement was made with the SCE placed in four locations on the concrete surface and repeated over three days. Figure 5.8 shows a plot of the average potential of each electrode vs. electrochemical age. The potential of the Fe increased with age while the Zn decreased initially through a minimum and then increased. The minimum appeared to occur approximately at the maximum in bond strength. The measurements of the Fe electrode had a good repeatability and reproducibility with standard deviations ranging between 6 and 33 mV for the 5 blocks. The variability of the Zn was much greater, with a standard deviation as high as 161 mV.

73
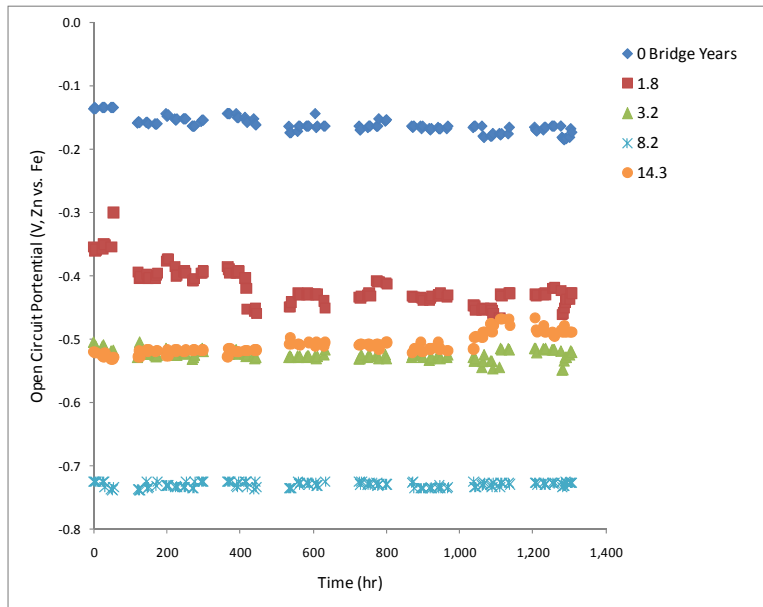
Figure 5.7: Open circuit potential vs. time for different aged blocks
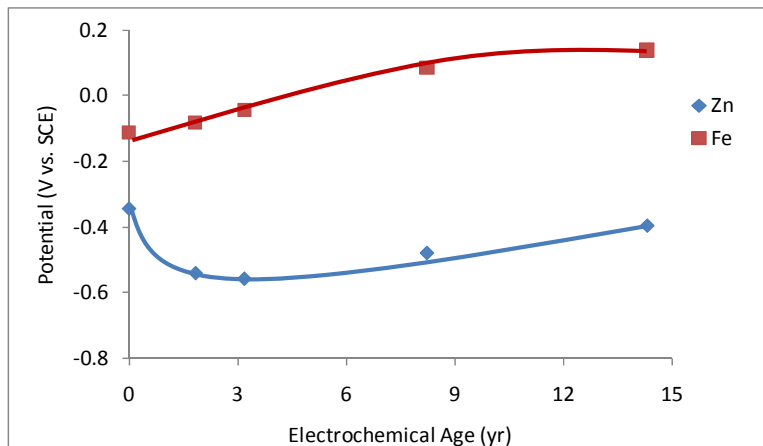
Figure 5.8: Average potential of Zn (blue diamonds) and Fe (red squares) vs. a SCE

Figure 5.2 is well represented by a straight line, i.e., a simple resistance. Upon investigation of the deviations from the response, it was found that the deviation was systematic and was similar for all blocks studied. The magnitude was small, and the phenomena observed may or may not have been physically significant. Figure 5.9 shows the deviation from the current voltage curve shown in Figure 5.2. The values for current on the y-axis were obtained by subtracting the best fit line of Figure 5.2. The 0.5 Hz sinusoidal component of the response, showing 5 or 6 periods per sweep direction, was believed to be a measurement artifact and could have resulted from a lower frequency sampling of a 60 Hz signal. The amplitude of the sinusoid varied throughout

74

the experiment from very pronounced, i.e., larger than shown in Figure 5.9, to barely noticeable, i.e., much smaller than shown in Figure 5.9.
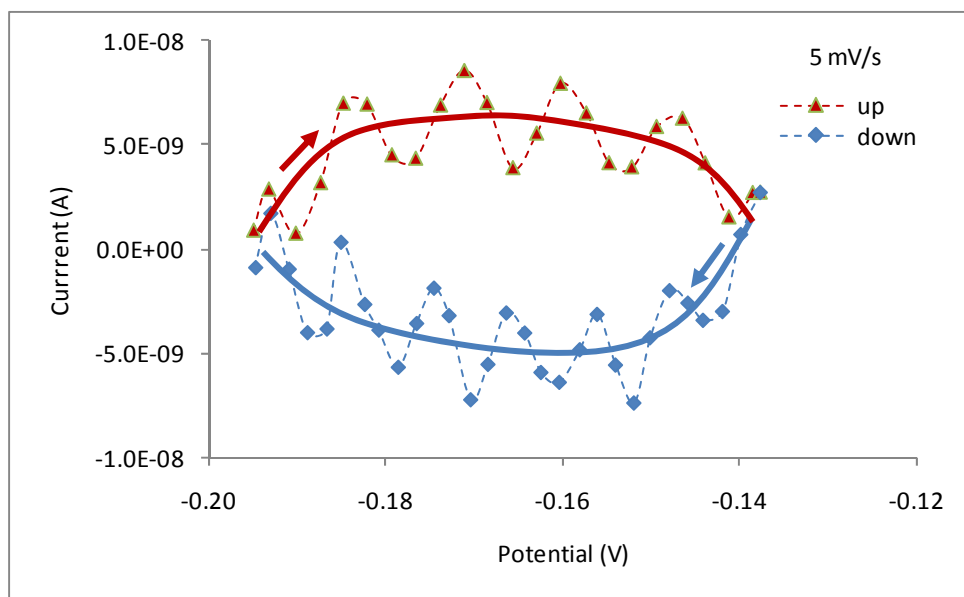
Figure 5.9: Capacitive portion of the IV curve shown in Figure 5.2

The average of the deviation (solid lines) looked similar to a capacitive signal seen in cyclic voltammetry. The sweep toward higher potentials, in the "up" direction (red arrow), resulted in a higher current than the "down" direction.

This portion of the cyclic voltammegram begins during a reduction processes on the zinc (probably mostly the reduction of water) and oxidation at the iron surface. Conversely, the process represented by the blue diamonds begins with an oxidative process at the zinc, and the response shows a lower current. The magnitude of the deviation current is on the order of 20 times less than the resistive current (see Figure 5.2).

This experiment was repeated with a scan rate of 500 mV/s with the current not appreciably changing. If the source was capacitive collecting of charge, it would be expected that the current would be two orders of magnitude greater $\left(i = \dfrac{dq}{dt} = C\dfrac{dE}{dt} \right)$ (*Brett and Brett 1993*).

Figure 5.10 shows plots similar to that described in Figure 5.9 for the scan of the differently aged blocks. The magnitude of the current is roughly the same in all cases but decreases slightly with electrochemical age.
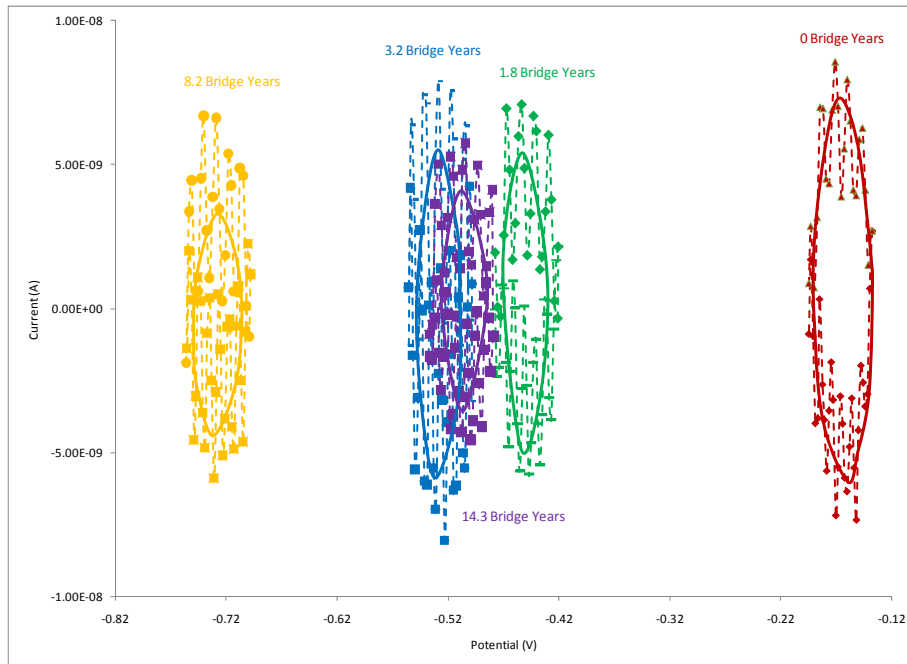
Figure 5.10: Capacitive portion of the IV curve for the 5 differently aged blocks

The next experiments were performed to determine the dynamic electrical response after water was applied to the zinc surface. The dynamic response could then be related to anode condition. Dynamic resistance measurements were completed on electrochemically aged blocks of 1.8 and 7.4 bridge years. These ages corresponded to values of intermediate and large resistance from the dry measurements (Figure 5.4). The same test procedure was used on these blocks as described above, with the exception of the addition of water. Before the water was added, a dry resistance measurement was taken as a basis. One or four milliliters of water were then placed directly around the wire that was soldered to the zinc anode. Resistance measurements were taken every half hour after water was placed on the sample.

Figure 5.11 shows the results of resistance vs. time for the two blocks. The 1 mL addition of water was repeated four times on the block aged for 7.4 bridge years. In most cases, a significant decrease in resistance was not detected after the water had been applied. The overall decrease in resistance for the experiment averaged about 60 kΩ over a period of six hours, which was on the same order as the resistance drop for the dry resistance experiments for a given day (Figure 5.5). Data collected from the experimental runs containing 4 mL of water showed no consistent difference compared to the data with 1 mL of water. There were changes in the resistance from run to run, but this was also observed during the dry resistance testing and occurred on a day-to-day basis.

76
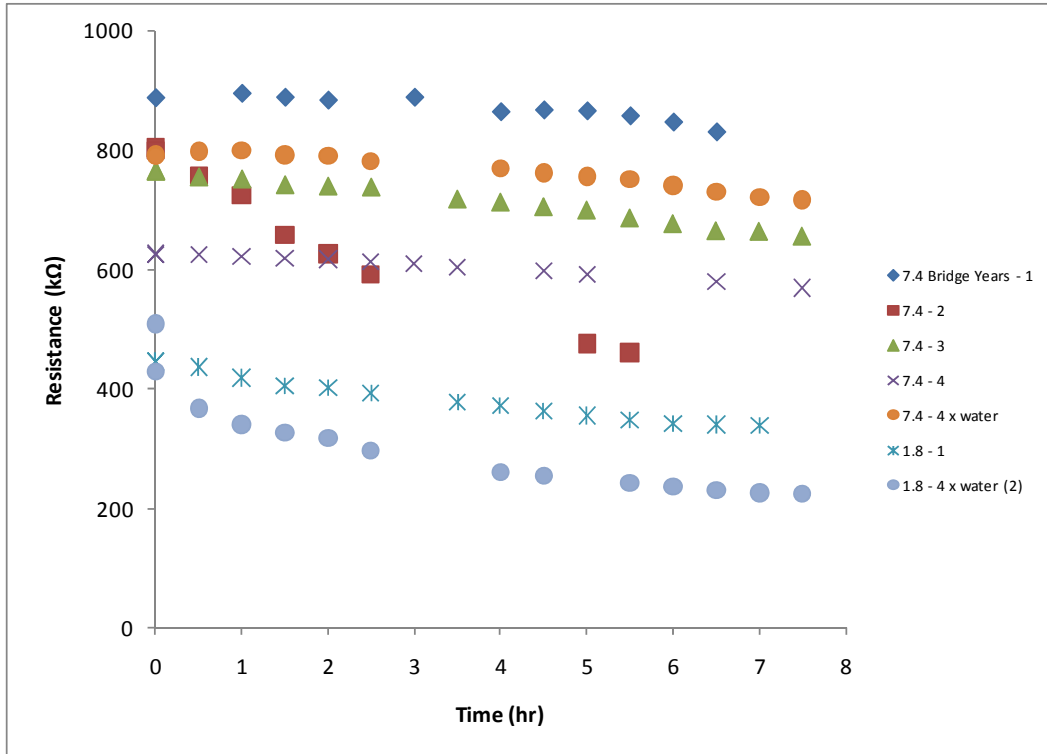
Figure 5.11: Dynamic response of resistance with wetting the anode surface

An interesting observation was made on the second experiment with the 7.4 year block. Labeled, 7.4-2. The resistance dropped significantly compared to the other three runs. After testing was complete and the water evaporated from the test site, a small pin hole was noticed in the Zn anode at the site where the test was performed. It is believed that the pin hole allowed the water a direct path to the concrete-zinc interface, reducing the resistance. To attempt to verify this hypothesis, a new lead was soldered at the edge of the zinc layer adjacent to an adhesion test site. Water was then intentionally applied to the concrete and zinc surface. Figure 5.12 compares the change in resistance for three different tests on the same block. Immediately after the water was applied the resistance dropped by almost 50 kΩ. The resistance continued to drop significantly over the period of six hours. The change in resistance was the same order of magnitude as the second run on the 7.4 year block (7.4-2). This suggested that the presence of water at the zinc-concrete interface may have significantly decreased the resistance.
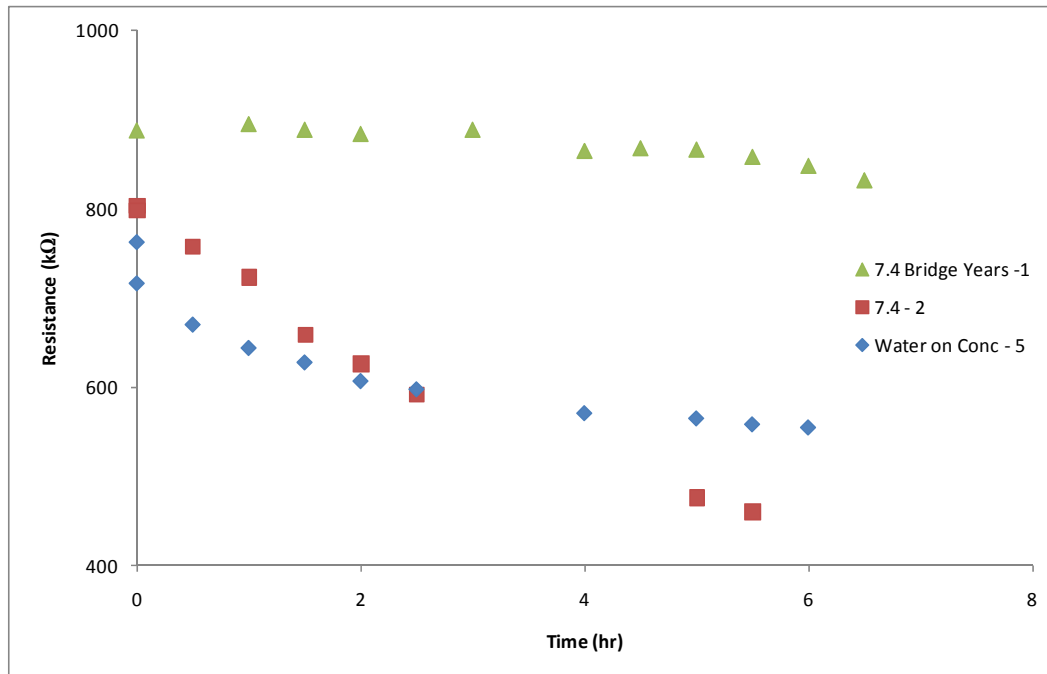
Figure 5.12: Comparison of data collected by wetting concrete and pin hole

It was believed that the absorption of water through the sprayed zinc into the sample would decrease the resistance. In a previous study (*Rehani 2000*) it was noticed that the potential difference of zinc vs. iron changed dramatically soon after wetting the sample (Figure 2.6). These measurements were made during the course of an accelerated aging experiment. However, it has also been observed that the fluid permeability of a sample decreases as it is aged, and this decrease has been attributed to the growth of zinc products in zones 2 and 3 (*Covino, et al. 2002*).

It is possible that the water was not absorbed through the zinc layer due to the effect of the product layer. Referring to Figure 1.5a, it can be seen that the permeability of the zinc anode is essentially zero when the anode reaches an age of four years. The data from the 7.4 year block were consistent with this model. If the product layer hindered the water from reaching the concrete, there would be no major change in the resistance of the sample, with the exception of the location with the pin hole.

The same explanation cannot be used for the 1.8 year aged block. However, data from Figure 5.12 illustrate that the overall resistance drop for the two samples was similar. These blocks had been stored approximately 15 years between experiments. Thus it is possible that ionic transport and reaction processes occurring over a longer time scale changed the nature of the zinc-concrete interface in the 1.8 year block, reducing its permeability.

After evaporation of the water, a white powder-like substance formed on the surface of the zinc anode, as shown in Figure 5.13. It was noticed that the majority of white powder formed in the vicinity closest to the pin hole. A similar white powder-like substance was noticed on Cape

Creek Bridge in Oregon at surface holes and voids two years after the CP system was implemented (*Brousseau, et al. 1995*). White powder has been observed at the concrete interface and was shown to be primarily composed of the crystal structure of zincite, ZnO (*Weale 1992*). This interfacial product was also observed by Covino, et al. from samples that had undergone "substantial electrochemical aging" (*Covino, et al. 2002*). Presumably, the white powder at the surface was leached by the wetting and drying cycles from this experiment.
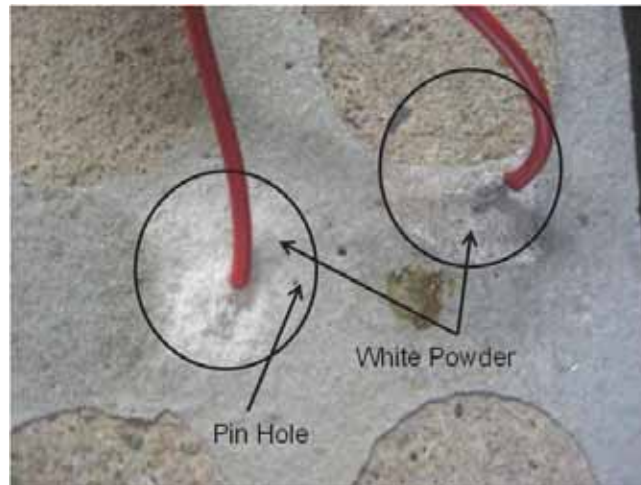
Figure 5.13: White powder-like substance formed on block 14 (7.4 Bridge years) after wet resistance testing

6.0   CONCLUSION AND RECOMMENDATIONS

Two separate technologies, ultrasound and resistance/permeability, were studied to assess their potential for determining the condition of zinc anodes in cathodic protection systems in the field. Requirements of a suitable field technology include the following: that it is non-destructive or minimally destructive testing; that it provides quick and easy operation with little or no technical background needed for field personnel; and that it provides information to assist ODOT in planning zinc anode repair and/or replacement.

Three different sets of samples were tested with the ultrasonic measuring system. Based on time-of-flight analysis, this system was able to detect well the difference in thicknesses of zinc sheet samples. The measured thickness values were essentially the same as the nominal thicknesses. On the other hand, the input acoustic pulse was scattered by the thermal sprayed zinc-concrete slab samples, whether aged or unaged, resulting in no detected signal from the samples. It is believed that the ultrasonic waves were scattered due to the many irregular interfaces inherent in the thermal sprayed zinc-concrete specimens.

It is recommended that a different ultrasound testing configuration using surface (Lamb) waves be investigated. This technique is more complex than the approach described in this report, since it requires a detector separate from the transducer, and the analysis involves more factors. Such configurations are used in aerospace and automotive industries. Scattering mechanisms similar to those observed in thermal sprayed zinc-concrete specimens could potentially impede these measurements. It is therefore also recommended that the fundamental source of scattering be further studied.

Using cyclic voltammetry, the resistances of thermal sprayed zinc-concrete-iron electrochemical cells were measured. Unaged as well as accelerated aged samples were tested. The average resistance increased monotonically up to approximately five bridge years, which corresponded, generally, to the maximum bond strength. Individual resistance data varied substantially over time, but these changes in resistance between measurements were consistent among the blocks. This effect was shown to inversely correlate with temperature and is believed to result from other environmental factors as well. The open circuit potential (Zn vs. Fe) showed less variation than the resistance with time. Its magnitude increased up to 8.2 bridge years and then decreased. A three electrode configuration showed individual potential changes at each electrode, with the potential of Zn generally tracking the resistance and bond strength trends with aging, and the potential of Fe increasing with age.

The change in resistance with wetting was impeded by the lack of permeability of the zinc, even in a sample aged 1.8 bridge years. However, when water had a path to the zinc-concrete interface, either through a pin hole or by being placed on bare concrete adjacent to the zinc, resistance decreased noticeably with time.

It is recommended that a simple field test may be developed where the response in applied voltage is monitored as a zone is sprayed with water and the CP system is controlled at constant current. Such a test may be aided by systematic creation of pin holes in the thermal sprayed zinc anode. It is therefore recommended that the creation of pin holes be systematically studied in an experiment using thermal sprayed zinc-concrete slabs that have been subjected to accelerated aging. In such a study the electrical response of blocks without pin holes could be compared to those with pin holes distributed systematically in different geometries. The preliminary findings from this study suggest that not only will the creation of pin holes facilitate characterization of anode condition through electrical response, but it may also significantly decrease the circuit resistance of the electrochemical cell, and thereby increase the service life of the anode. Such a strategy would be similar to the use of humectants to decrease the resistivity of the interfacial zinc product layer (*Holcomb, et al. 2002*).

Finally, synthesizing the results from both technologies, it is recommended that ultrasonic tests be performed on systems with pin holes to see if the soluble component from the zinc product layer is scattering the signal.

7.0   REFERENCES

Ahmad, Z. Principles of Corrosion Engineering and Corrosion Control. Butterworth, United Kingdom, 46. 2006.

Aziz, M.A. and M.A. Mansur. Deterioration of marine concrete structures with special emphasis on corrosion of steel and its remedies. Corrosion of reinforcement in concrete construction. Society of Chemical Industry, London, England, 91-99. 1983.

Berkeley, K.G.C. and S. Pathmanaban. Cathodic Protection of Reinforcement Steel in Concrete. Butterworth, United Kingdom. 1989.

Bertolini, L., P. Pedeferri, E. Redaelli, and T. Pastore. Repassivation of steel in carbonated concrete induced by cathodic protection. Materials and Corrosion. WILEY-VCH, 54, 163-175. 2003.

Bertolini, L., B. Elsener, P. Pedeferri, and R. Polder. Corrosion of Steel in Concrete, WILEY-VCH, Federal Republic of Germany. 2004.

Brett, C.M.A and A.M.O. Brett. Electrochemistry Principles, Methods, and Applications. Oxford University Press, Oxford, United Kingdom. 1993.

Brousseau, R., M. Arnott, and B. Baldock. Laboratory Performance of Zinc Anodes for Impressed Current Cathodic Protection of Reinforced Concrete. Corrosion Engineering. NACE International, 51, 639-644. August 1995.

Cao, P., W. Chen, N. Karkhanis, and K. K. Shung. Accurate corneal thickness measurement using ultrasound. Proceedings of SPIE. 4687, 430-437. 2002.

Covino, Jr., B.S., S.D. Cramer, G.R. Holcomb, S.J. Bullard, G.E. McGill, and C.B. Cryer. Thermal-sprayed zinc anodes for cathodic protection of reinforced concrete structures. Materials for the New Millennium. ed. K. P. Chong, American Society of Civil Engineers, New York, NY, 2, 1512-1521. 1996.

Covino, Jr., B.S., S.D. Cramer, S.J. Bullard, G.R. Holcomb, J.H. Russell, W.K. Collins, H.M. Laylor, and C.B. Cryer. Performance of Zinc Anodes for Cathodic Protection of Reinforced Concrete Bridges. Final Report, SPR 364. Report No. FHWA-OR-RD-02-10. Oregon Department of Transportation, Salem OR, and Federal Highway Administration, Washington DC. March 2002.

Cramer, S.D., S.J. Bullard, and B.S. Covino, Jr. Zinc Anode Delamination on Arches Section of Yaquina Bay Bridge. Interim Report to Bridge Section, Oregon Department of Transportation, Salem, OR. May 2006.

Cramer, S.D. and M.D. Anderson. Zinc Anode Aging on the Arches and South Approach Sections of the Yaquina Bay Bridge. Final Report, Oregon Department of Transportation, Salem, OR. April 2009.

Daily, S.F. Understanding Corrosion and Cathodic Protection of Reinforced Concrete Structures. Corrpro Companies Inc., 2000, 1-5. 1997.

Dempsey, Robert J., Daron G. Davis, Robert G. Buice, Jr. and Robert A. Lodder. Driven To Depth: Biological and Medical Applications of the Near-Infrared Spectrometry. Retrieved September 7, 2006 from the World Wide Web: http://www.pharm.uky.edu/ASRG/Papers/Depth/depth.html#back14.

General Dynamics. Nondestructive Testing, ultrasonic testing, General Dynamics, Convair Division, San Diego, California. 1967.

Hime,W. and B. Erlin. Some Chemical and Physical Aspects of Phenomena Associated with Chloride-Induced Corrosion. *Corrosion, Concrete, and Chlorides*, ACI SP-102, F.W. Gibson Ed., American Concrete Institute, Detroit, 1. 1987.

Hobbs, D.W. Chloride Ingress and Chloride-Induced Corrosion in Reinforced Concrete Members. Corrosion of Reinforcement in Concrete Construction, ed. Page, C.L., Bamforth, P.B., and Figg, J. W., The Royal society of Chemistry, Cornwall, United Kingdom, 124. 1996.

Holcomb, G.R., B.S. Covino, Jr., S.D. Cramer, J.H.R. Russell, S.J. Bullard, W.K. Collins, J.E. Bennett, S.M. Soltesz, and H. Laylor. Humectants To Augment Current From Metallized Zinc Cathodic Protection Systems on Concrete. Final Report, SPR 384. Report No. FHWA-OR-RD-03-08. Oregon Department of Transportation, Salem, OR. 2002.

Innerspec Technologies. Products and Services. Retrieved September 22, 2006 from the World Wide Web: http://www.innerspec.com/site/products.asp#3.

Irie, H., Y. Yoshida, Y. Sakurada, and T. Ito. Non-destructive-testing Methods for Concrete Structures. NTT Technical Review, 6, 1-6. May 2008.

Koretsky, M.D., F. Abooameri, and J.C. Westall. Effect of Concrete Pore Saturation on Cathodic Protection of Steel-Reinforced Concrete Bridges. The Journal of Science and Engineering, 55, 52-64. 1999.

Lanstaff, Sarah. Coating Characterization and Interface Properties Under Service Conditions. 1998. Retrieved October 2, 2006 from the World Wide Web: http://www.physics.queensu.ca/wwwhome/assg/katia.htm.

McLaughlin, K. A Beginner's Guide to – Wall Thickness Measurement Using Ultrasound. British Journal of Non-Destructive Testing, 31, 196-198. 1989.

Micro Photonics. Nanovea Series scratch and adhesion testing. Retrieved October 3, 2006 from the World Wide Web: http://www.microphotonics.com/scratchmenu.html

Mudd, C.J., G.L. Mussinelli, M. Tettammanti, and P. Pedeferri. Cathodic Protection of Steel in Concrete. Materials Performance, National Association of Corrosion Engineers, 27**,** 18-24. 1988.

Muehlenkamp, E.B., M.D. Koretsky, and J.C. Westall. Effect of Moisture on the Spatial Uniformity of Cathodic Protection of Steel in Reinforced Concrete. Corrosion 61, 519. 2005.

NDT Resource Center. Basic Principles of Ultrasonic Testing. Retrieved April 20, 2009 from the World Wide Web: http://www.ndt-ed.org/EducationResources/CommunityCollege/Ultrasonics/Introduction/description.htm.

NDT Resource Center. Introduction to Thermal Testing. Retrieved September 20, 2006 from the World Wide Web: http://www.ndt-ed.org/EducationResources/CommunityCollege/Other%20Methods/IRT/IR_index.htm.

Oregon Department of Transportation (ODOT). Personal communication with Steven Soltesz, ODOT Research Section. 2009

Orlova, N.V., J.C. Westall, M. Rehani, and M.D. Koretsky. The Study of Chloride Ion Migration in Reinforced Concrete under Cathodic Protection. Final Report, SPR 357. Report No. FHWA-OR-RD-00-03 Oregon Department of Transportation, Salem, OR. September 1999.

Osgerby, S., S. Saunders, and J. Banks. Scale and Coating Adhesion: A Procedure for Laboratory Tests. National Physical Lab. Teddington (United Kingdom). Centre for Materials Measurement and Technology. Report # CMMT(MN)026. Crown Copyright: Controller of HMSO. 1998.

Panossian, Z., L. Mariaca, M. Morcillo, S. Flores, J. Rocha, J.J. Pena, F. Herrera, F. Corvo, M. Sanchez, O.T. Rincon, G. Pridybailo, and J. Simancas. Steel cathodic protection afforded by zinc, aluminum and zinc/aluminum alloy coatings in the atmosphere. Surface and Coatings Technology. Elsevier, 190, 244-248. 2005.

Pathak, L., V.R. Seshadri, C. Kumaravadivelu, G. Sreenivasan, and V.S. Raghunathan. Profiling a Reactor component Using Ultrasonics. IEEE Transactions on Nuclear Science. **42**, 110-114. April 1995.

Pilgaard, Michael. Pilgaard Solution, Zinc, Retrieved April 20, 2009 from the World Wide Web: http://www.pilgaard.info/Elements/Zn.htm.

Polychromix. Digital Transform Spectroscopy (DTS^{TM}). Retrieved September 11, 2006 from the World Wide Web: http://www.polychromix.com/details_spectroscopy_bluebox.php?ID=1.

Popovics, S., Y. Simeonov, G. Bozhinov, and N. Barovsky, Durability of reinforced concrete in sea water. Corrosion of reinforcement in concrete construction. Society of Chemical Industry, London, England, 19-38. June 1983.

Qualitest. Concrete Rebound Hammer. Retrieved September 6, 2006 from the World Wide Web: http://www.qualitest-inc.com/concretehammer.htm.

Quality Network Inc. Ultrasonic and EMAT testing. Retrieved September 26, 2006 from the World Wide Web: http://www.qnetworld.com/ultrasonic_testing/ultrasonic_testing.htm.

Rehani, Manu. Transport of Chloride Ions during Accelerated Cathodic Protection of Reinforced Concrete Structures. Corvallis, OR: Oregon State University, Master's Thesis. June 2000.

Robinson, R.A. and R.H. Stokes. Electrolyte Solutions. Butterworth, United Kingdom, 465. 1959.

Rose, Joseph L. *Ultrasonic Waves in Solid Media*. Cambridge University Press, Cambridge, United Kingdom, 40. 1999.

Rose, Joseph L. A Baseline and Vision of Ultrasonic Guided Wave Inspection Potential. *Journal of Pressure Vessel Technology*. 124, 273-282. 2002.

Schumacher, J., W. Eichler, O. Bauer, and K.F. Klotz. Perioperative Tissue Thickness Measurement by a New Miniature Ultrasound Device. Journal of Clinical Monitoring and Computing. Kluwer Academic Publishers, 14, 471-476. 1998.

Scientific Optical Solutions. FieldSpec® spectroradiometers. Retrieved September 5, 2006 from the World Wide Web**:** http://www.lab-sos.co.uk/field_spec.htm.

Sagüés, A.A., and R.G. Powers. Sprayed-Zinc Sacrificial Anodes for Reinforced Concrete in Marine Service. Corrosion. 52, 508. 1996.

Shibata, T. and M. Ishihara. Ultrasonic signal characteristics by pulse-echo technique and mechanical strength of graphite materials with porous structure. Nuclear Engineering and Design. Elsevier, 203, 133-141. 2001.

Spectroscopic and Analytical Developments. Hand Held, Battery Powered Spectrophotometer. Retrieved September 7, 2006 from the World Wide Web: http://www.spectroscopic.co.uk/manufactured-products/hand-held-spectrophotometer.html.

Toronto Surplus and Scientific Inc. Kyoritsu 4102 Earth Tester. Retrieved October 31, 2006 from the World Wide Web: http://www.torontosurplus.com/redirect.php?middleframe=http://www.torontosurplus.com/tes/tes54.htm.

Vindium Engineering. New England Research TinyPerm Portable Permeameter. Retrieved September 12, 2006 from the World Wide Web: http://www.vindum.com/Probe%20Permeameters.html.

Weale, C.J. Cathodic protection of reinforced concrete anodic processes in cements and related electrolytes. Thesis no. DX 185652. West Yorkshire, UK: The British Library. 1992.

Whiting, D.A., M.A. Nagi, and J.P. Broomfield. Laboratory Evaluation of Sacrificial Anode Materials for Cathodic Protection of Reinforced Concrete Bridges. Corrosion. NACE International, 52, 472-479. 1996.

Yee, B.G.W. and J.C. Couchman. Application of Ultrasound to NDE Materials. IEEE Transactions on Sonics and Ultasonics. 23, 299-305. September, 1976.

APPENDICES

APPENDIX A: TECHNOLOGY REVIEW

APPENDIX A – TECHNOLOGY REVIEW

A review of possible technologies that could potentially determine the condition of the TS Zn anode was completed as Task 1 for this project. This review was discussed at a TAC meeting on February 6, 2007 and the intermediate report was submitted in March 2007. A summary of the report contents is provided below.

The TAC decided that the technologies to receive further consideration in order of preference are guided wave ultrasonics, near infrared, and a hybrid permeability and resistivity method. The technologies will be evaluated on a proof of concept basis. The technologies will be tested sequentially only going to the next choice if the initial evaluation shows that the technique is not viable.

A.1   Fluid Permeability Testing

A.1.1 Fundamental Operating Principles

Fluid permeability is the measure of a material or porous media to transmit fluids. Specifically in pressurized or vacuum permeability testing, it is the measure of the transmitted fluid related to the pressure gradient applied over the porous media. This is a property of the material only, not the fluid.

Fluid (air and water) permeability testing has been done by (NETL) on the Yaquina Bay Bridge and their testing blocks used for bridge condition simulations on the CP systems. The air permeability testing showed no significant trends with the bond strength over the tested ages of the blocks or CP zones on the bridge. In periodically-wetted slabs a direct correlation with age and permeability was discovered using water permeability testing early in the aging process, but did not show a trend in the later ages. As discussed in Section 1.1, the graphs in Figure 1.4 show that the water permeability at the pressure gradient used approaches zero well before the delamination period and at approximately the same time as the Zn concrete interface reaches its maximum bond strength. Also, it is assumed that for the un-wetted slabs, due to the nonexistence of zones 2 and 3, there would still be high fluid permeability at very low bond strengths. This result is contradictory to the trend of the periodically-wetted slabs; therefore fluid permeability is not a practical technology for characterization of local anode conditions.

A.1.2 Advantages and Disadvantages

Advantages:
1. Portable
2. Nondestructive
3. Easy to use with little training
4. Commercially available devices

The main disadvantage is unlikelihood of success. There is significant evidence that concludes there is no correlation between fluid permeability and anode lifespan.

A.1.3 Commercially Available Devices

There are some commercially available devices for air permeameters already in use to determine concrete and rock permeability's. ODOT uses a permeameter that uses a rubber gasket that forms a vacuum seal between the measuring head and concrete surface shown in Figure A.1.

a)   b)
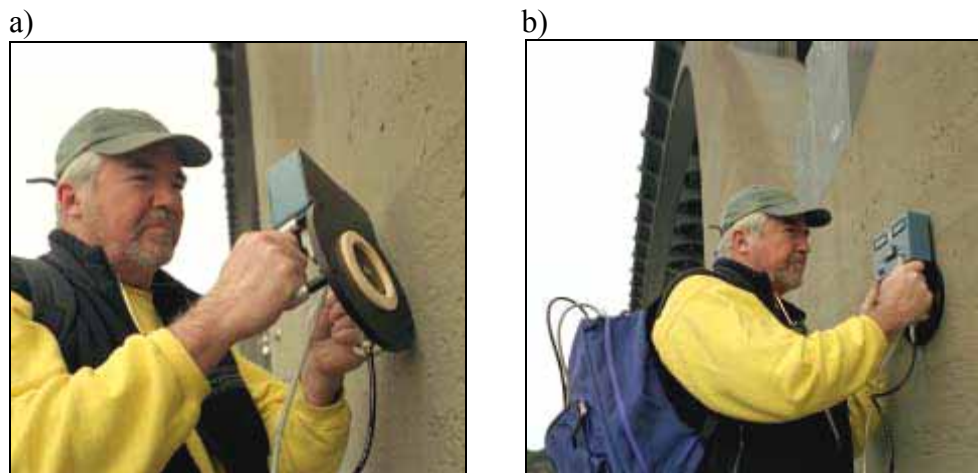
Figure A.1:   **a) Close-up of measuring head for surface air permeability instrument showing the flexible rubber gasket; b) portable surface air permeability instrument in use (*Covino, et al. 2002*)**

There is also the TinyPerm by NER's which is a portable hand-held air permeameter, shown in Figure A2, which is used for measurement of rock matrix permeability or effective fracture apertures on outcrops and at the core scale.

The operator pressures a rubber nozzle against the specimen and withdraws air from it with a single stroke of a syringe. As air is pulled from the sample, a micro-controller unit simultaneously monitors the syringe volume and the transient vacuum pulse created at the sample surface. Using signal processing algorithms the micro-controller computes the response function of the sample/instrument system. Key characteristics of this response are displayed on the liquid crystal display (LCD) (*Vindium 2006*). There are many other very similar devices from other manufacturers also available.

Figure A.2:   **The TinyPerm can be operated by one person and easily carried in a small backpack. The unit is weather and dust resistant and comes in a rugged case for transportation and shipping. The micro-controller and electronics are enclosed in a sturdy weatherproof case with LCD display, operating continuously for several hours on a single 9-volt alkaline battery (*Vindium 2006*).**

All of the liquid permeability testing devices that were found for field use are a vertical falling-head type measurement, which is impractical for the CP protection analysis. There are lab based pressurized fluid permeability devices, which are mainly used to measure cement based and stone construction materials. There have been little advancements in a field pressurized permeability device for the field.

A.2   Resistance/Impedance

A.2.1 Fundamental Operating Principles

Circuit resistance is one of the primary measurements that have been made in the electrochemically aged (EA) Zn CP research. The circuit resistance of each zone is representative of the overall zone working condition. Due to the varying environmental conditions each zone is exposed to, the Zn anode may display a range of local conditions, which cannot be detected by the overall circuit resistance. The results from the NETL report showing the Zn circuit resistance relative to charge for un-wetted and periodically-wetted slabs are shown in Figure A.3.
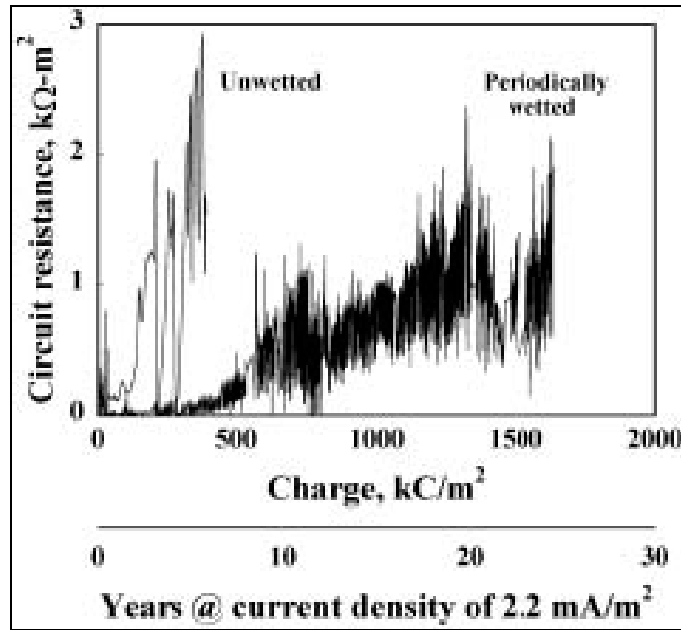
Figure A.3:   TS Zn anode circuit resistance versus electrochemical age for both periodically-wetted and un-wetted concrete slabs. Reproduced from Covino, et al. (*2002*).

These data indicate that there is an increase in circuit resistance with electrochemical age. The saw-toothed pattern shown in the data for the periodically wetted slabs is a result of the decrease in resistance when the wetting occurs and an increase in the resistance when the slab is drying. NETL research also shows that over time there is an increase in the system voltage decay during the wetting period and a decrease in system voltage rise during the drying period. All of the trends shown here are supported by research conducted by others (*Rehani 2000*). These concepts were a main motivator in one of the hybrid technology options, which is discussed in Section A.9.

The zinc anode resistance taken for the EA blocks in the NETL research also shows an increase in resistance with time. These data were obtained by taking anode surface resistance measurements as shown in Figure A.4a. Although the anode resistance is considered a local measurement, there is little correlation of the readings to the local anode condition.

a)

b)
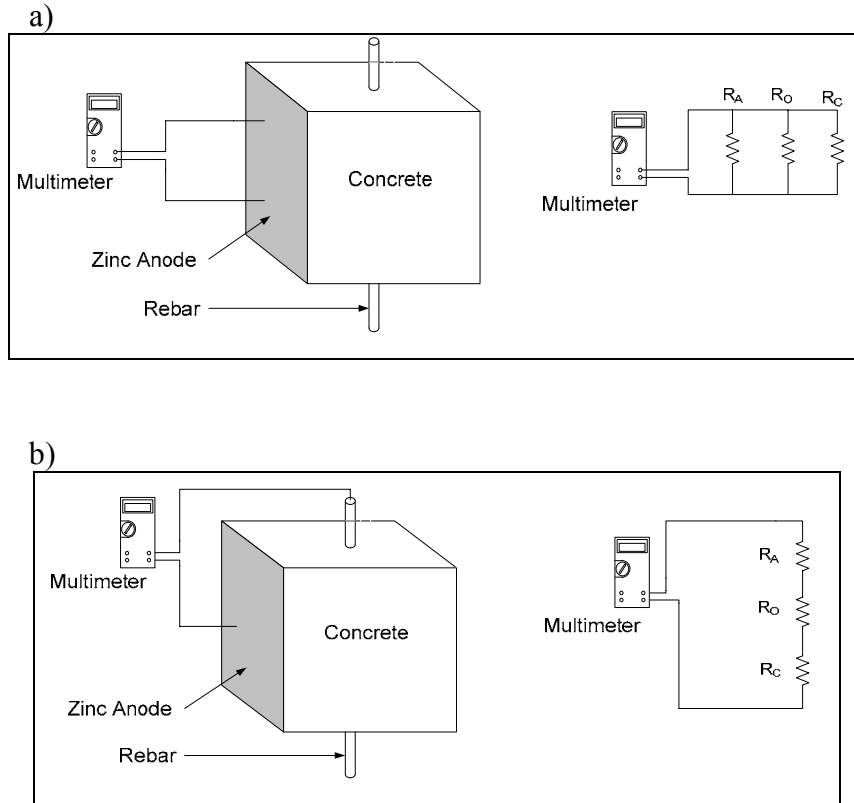
Figure A.4: **Resistance measuring techniques: a) Anode surface b) between zinc anode and rebar reinforcement**

The reported value is an equivalent parallel resistance of the Zn anode, oxide layer, and concrete:

$$\frac{1}{R_E} = \frac{1}{R_A} + \frac{1}{R_O} + \frac{1}{R_C} \qquad \text{(A-1)}$$

where R_E is the equivalent resistance and R_A, R_O, and R_C are the anode, oxide layer and concrete resistance, respectively. Since the oxide layer and concrete resistance are much larger than the anode resistance the equation can be simplified to:

$$R_E \approx R_A \qquad \text{(A-2)}$$

This result means that the resistance of the concrete or the oxide layer will not affect the measured equivalent resistance. Thus, only the anode resistance is determined by this measurement. These data become very useful in determining the Zn anode thickness, which is discussed in further detail in the NETL report (*Covino, et al. 2002*). Since delamination typically occurs much earlier than the consumption of the anode, this is not a good representation of anode condition, or time to delamination.

A-5

In order to obtain a good representation of the growth of the oxide layer the resistance in series between the Zn anode and the rebar reinforcement must be measured, as shown in Figure A.4b.With the resistance being measured in this manner the equivalent resistance is represented by the sum of the Zn anode, oxide layer, and concrete resistance:

$$R_E = R_A + R_O + R_C \qquad \textbf{(A-3)}$$

With the resistance of the concrete and the anode being known quantities, their contribution to the equivalent resistance can be calibrated and data for the oxide layer resistance are possible to obtain. As the oxide growth at the interface increases, the resistance will increase and the bond strength will decrease, resulting in a correlation between the bond strength of the anode and the oxide layer resistance. However, the percentage of the oxide layer in the three zones will change relative to the environmental conditions that area is exposed to, and this must be accounted for. Although determination of the resistance of each of these layers is not possible through this form of resistance measurement, it may still be useful in characterizing anode lifespan when used with another measurement (Section A.9).

A.2.2 Advantages and Disadvantages

Advantages:
      1) Easy to use with little experience
      2) Fairly portable
      3) Quick measurements
      4) Non-destructive
      5) Minor changes to commercial devices
      6) Low development time
      7) Low cost of production

Disadvantages:
      1) The need to tie into the rebar reinforcement for each zone
      2) Differences in Oxide layer chemistry will change results
      3) Distance away from rebar will change results

A.2.3 Commercially Available Devices

There are many commercially available multimeters on the market, which are used for a variety of different applications. One multimeter shown in Figure A.5 is used for earth testing. Any available multimeter with slight modifications would be suitable for oxide layer resistance measurements.

Figure A.5:   Kyoritsu 4102 Earth Tester, Resistance and Voltage Meter (*Toronto 2006*)

A.2.4 Possible Device Modifications

The only device modification needed for this type of resistance measurement would be to adapt a typical multimeter with an extended lead that would tie into the rebar reinforcement. For field measurements of the local anode conditions, one of the leads must tie into the rebar so the resistances are in series. Typically, there are limited areas to tie into the rebar in each zone; therefore an extended lead is needed that would allow measurements to be made anywhere within the zone.

A.3   Near-IR Testing

A.3.1 Fundamental Operating Principles

Infrared (IR) radiation is electromagnetic radiation that falls between the wavelength of visible light (750 nm) and radio waves (1 mm), as shown in Figure A.6. This range is usually divided into 5 sections with near IR falling in the range of 0.75-1.40 μm and short IR falling between 1.40-3.00 μm in wavelength. Near and short wavelength IR is usually grouped together and called the near-IR region. This region is the most promising for molecular spectroscopy.
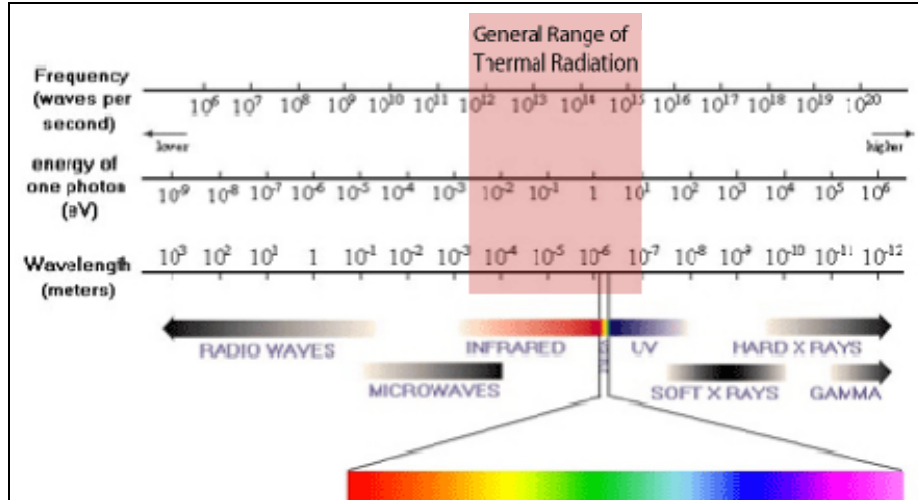
Figure A.6: Wavelength of electromagnetic radiation. Reproduced from NDT (*2006*)

IR spectroscopy can be used to help determine the composition of a material based on its absorption of IR radiation. Different frequencies of radiation are absorbed by different stretches and bends of the molecular bonds in the sample. Near-IR spectroscopy is used mainly for identifying or quantifying molecules based on bonded hydrogen atoms. Near-IR spectrometry is thus routinely used for quantitative analyses of water, alcohols, amines, and any compounds with C-H, N-H, and/or O-H groups (*Dempsey, et al. 2006*).

A skin depth calculation was performed, using Equation 4, to determine the distance an IR wave can penetrate into Zn, where δ is the skin depth in [μm], ρ is resistivity in [Ω*m], μ_R is relative permeability, and f is frequency in [Hz].

$$\delta = 503 * \sqrt{\frac{\rho}{\mu_R f}}$$ (A-4)

Assuming that Zn acts as a diamagnetic solid ($\mu_R = 1$), the IR waves have a skin depth in Zn of approximately 5.5-11.5 μm. The anode thickness on the testing blocks and bridges are around 430-500 μm, and is much larger than the skin depth. Thus, in order to use this technology, some sort of modification must be made to the surface to achieve the penetration required. This surface modification would cause increased destructiveness relative to typical near-IR testing.

If the needed penetration depths could be achieved, there is a strong possibility that the oxide layer in each measurement location could be characterized. Since the 3 zones consist of different concentrations of compounds, the approximate thickness of each zone could be determined and correlated to their effect on the bond strength and service life of the anode.

A.3.2 Advantages and Disadvantages

Near-IR spectrometry has many advantages. This process conserves time and materials in comparison to many more conventional analytical methods because:

1. Analysis times under 1 second are possible.

2. Simultaneous multi-component analysis is the norm.

3. No sample preparation is usually required for liquids, solids, or gases.

4. Noninvasive and nondestructive analysis is possible.

5. Cost per analysis is very low (no reagents are used).

6. Physical properties and biological effects can be calculated from spectra of   samples.

7. Automated correction of background and interferences is performed in instruments using computer algorithms.

8. Detection limits can be very low.

9. Samples sizes ranging "from picograms to planets" can be analyzed.

10. Molecular structural information can be derived from spectra (*Dempsey, et al. 2006*).

The main disadvantage is the inability for IR to penetrate the Zn layer. Due to this lack of penetration a more destructive test would be required in order obtain accurate readings at the test sites.

A.3.3 Commercially Available Devices

There are many of commercially available devices that are in use for near IR spectroscopy in the field. One example is DTS model spectrometers from Polychromix shown in Figure A.7.

a)

b)

Polychromix

30 Upton Drive, Wilmington, MA 01887
Tel: (978) 284-8000   Fax: (978) 284-8080

www.polychromix.com

DTS™ NIR Product Family
Near Infrared Spectrometers

Polychromix's DTS™ NIR Spectrometer product family uses an innovative MEMS spatial light modulator to deliver Digital Transform Near Infrared Spectrometers. DTS™ NIR Spectrometer products provide highly cost effective spectrometer solutions featuring excellent performance using a single InGaAs detector and no moving parts.

Device Specifications

Features
- Low price
- Multiple wavelength ranges available
- Low power consumption
- Measurement method automatically corrects for stray light effects
- No moving parts
- Compact and lightweight

Applications
- Laboratory analysis
- Industrial Process control
- Quality Control
- Portable in-field use
- Educational and academic

Order Information
For additional information please contact:

Mouli Ramani
VP of Marketing and Business Development
Polychromix
30 Upton Drive, Wilmington, MA, USA
Tel: +1 (978) 284-6007
Fax: +1 (978) 284-6060
salesdept@polychromix.com
www.polychromix.com

Specifications	DTS™ 1700	DTS™ 2500	DTS™ NB
Spectral Range	~930-1690 nm	~1710-2460 nm	1100-1350 nm
Absolute Wavelength Accuracy	±0.6nm fixed temperature (with parabolic fit)		
Resolution			
Pixel Spacing	8 nm	8 nm	2 nm
Optical Resolution	12 nm	22 nm	4 nm
Stray Light	<0.01% transmission of 10mm water at 1450 nm using Tungsten lamp & RGT 850 filter		
Signal to Noise Ratio	10,000 single acquisition with optimum light levels		
Photometric Stability	<0.05% over 6 hrs.		
Measurement time	<10 millisec. per spectral mask: ,<1 sec. per spectrum		
Input fiber	for optimum performance use ≥500 um diameter low OH fiber with SMA-905 connector.		
Module Size (w/electronics)	105 x 85 x 145mm (4.2x3.3x5.7")		
Weight	1.8 KG (4 lbs.)		
Hardware Interface	mini USB for both power and communications.		
A/D Converter	24 bit		
Power consumption	0.75W	1.25W	0.75W
Detector	single InGaAs	single InGaAs	single InGaAs w/2 stage cooler
Software included:	SpectralCode™ ; Contact Polychromix for: "my instrument", Labview driver, Excel plugin or API		
Operating Systems	Windows Me, 2000, & XP		
Operating Temp Range	15 to 35°C. Can operate at other temperatures subject to calibration.		
Storage Temp Range	-40 to +85°C		

Figure A.7: a) DTS-1700 covering the 900-1700 [nm] wavelength range; b) DTS product specifications (*Polychromix 2006*)

Polychromix offers a variety of DTS models that cover the wavelength range of 900-2500 nm and ranging from $7,199-11,999. Another device is the handheld, battery powered spectrophotometer from Spectroscopic Analytical Developments shown in Figure A.8a. It is designed to be easy to use by an unskilled operator, with stainless steel construction and a water tight seal. The handheld spectrophotometer has performance equal to lab spectrophotometers, a USB or RS232 interface to download measurement data, and can be programmed for specific applications (*Spectroscopic and Analytical Developments 2006*). A complete list of specifications is shown in Figure A.8b.

a)

b)

All Components

Stainless steel case
Waterproof to IP67
(For information on use in hazardous areas contact SAD)
Total weight   ~ 1.6 Kg

Battery compartment

Size   1750 mm x 60 mm x 25 mm
Weight   ~ 470 gms
Battery   Nickel hydride rechargeable cells
Rating   1.2 ampere hours x 9 volts
Automatic switch off – Battery save mode
Built in charging control
Charging supply   18 volt 2.2 amp
NOTE Use only the charging transformer supplied with the Authenticator.

Control unit

Size   1750 mm x 920 mm x 70 mm
Weight   ~ 900 gms
Keyboard   5 keys On/Off, Scroll up, Scroll down, Enter, Escape.
Display screen   2 line x 16 character alphanumeric display
Indicator LEDs   Green, Amber, Red
Built in microprocessor
Real time clock for date and time stamping of measurements
External (waterproof) connections   RS230 or USB
Wavelength ranges   190 nm to 450 nm, 380 nm to 750 nm, 190 nm to 750 nm
Absorbance range   0 – 2.0 Abs units

Sample chamber / Lamp units

Lamp   Miniature Deuterium lamp, Tungsten lamp, or both
Flow cell   Path lengths 0.2 mm, 1.0 mm, 6.0 mm, 10.0 mm, 30.0 mm, 50.0mm
Sample entry and exit ports with non return valves
Size   75 mm x 60 mm
Weight   ~ 230 gms

Figure A.8:   a) Handheld, Battery Powered Spectrophotometer by Spectroscopic Analytical Developments; b) detailed specifications (*Spectroscopic and Analytical Developments 2006*)

There are also a variety of spectroradiometers from Scientific Optical Solutions (SOS) that are typically used in the field for similar applications, as shown in Figure A.9.

Figure A.9: **Spectroradiometer options provided by Scientific Optical Solutions (*Scientific Optical Solutions 2006*)**

These devices are used mainly for mineral concentrations, ground truthing, agricultural, vegetation, and forestry analysis. They come complete with a field setup that includes a backpack, computer for analysis and the measuring device. There are many other companies that have comparable technologies for field uses.

A.3.4 Possible Device Modifications

Near IR has many benefits, most importantly, the ease of measurement, cost and non-destructiveness. Near IR tests are capable of detecting the concentration of ZnO and $Zn(OH)_2$ in the zinc oxide layer. This could possibly give a direct correlation to bond strength and delamination time. Very few modifications, if any, would have to be made to the available devices in order to achieve the desired measurements; yet destructive surface altercations are needed to reach the oxide layer for penetration purposes.

A.4   **Acoustic Sensors**

Acoustic emissions sensors use ultrasound time-of-flight echo return as a basis for evaluation. There are many applications of acoustic sensors such as detection of minute traces of dangerous chemicals, 'Tactical Active' Sonar (SOund NAvigation and Ranging), ultrasonic imaging used for security purposes, etc. The most practical type of acoustic non-destructive testing for Zn anode analysis has been determined to be guided wave ultrasonic testing. This topic will be further discussed in Section A.6.

A.5 Rebound Testing

A.5.1 Fundamental Operating Principles

Rebound testing measures the absolute hardness or elasticity of a material. Hardness of a solid is the characteristic that expresses its resistance to permanent deformation. A material is said to be elastic if it deforms under stress, but returns to its original shape when the stress is removed.

This kind of testing is typically used for concreted strength testing and other similar applications in the field. There are many factors in the sample being measured that must be understood to interpret the data provided. The applicability to CP Zn anode testing does not seem very probable for this technology. Rebound testing's main use is not to measure surface strength, but to compare strength with other test samples taken. Depending on the hardness of each zone and their thicknesses, a variety of different bond strengths could be exhibited for the same rebound measurement. Therefore, a correlation between bond strength and rebound would be very difficult to develop.

A.5.2 Advantages and Disadvantages

 The advantages to the rebound testing are that it is cheap to operate, very portable and nondestructive. It is very practical for field use and is already in use for strength testing of concrete, specifically on bridges.

One of the disadvantages is the local variation in the sample. Sometimes the same area can be tested numerous times and have variation in the results. Multiple tests with average values are recommended. Also, a water saturated material will give different results than a dry material, and this may affect the Zn CP measurements in the field due to variation in bridge environments. The measuring device readings will also vary due to gravity if not held in the horizontal position.

A.5.3 Commercially Available Devices

Rebound testing is typically measured by the Schmidt hammer shown in Figures A.10-A.11. The hammer measures the rebound of a spring loaded mass impacting against the surface of the sample. When conducting the test the hammer should be held at right angles to the surface which in turn should be flat and smooth. The rebound reading will be affected by the orientation of the hammer, when used in a vertical position (on the underside of a suspended slab for example) gravity will increase the rebound distance of the mass and vice versa for a test conducted on a floor slab.

Figure A.10:   Schmidt hammer being used in the field to measure the compressive strength of the concrete (*Cement Association of Canada 2006*)

Figure A.11:   Digital Model W-D-1000 which is an advanced, completely automated digital test hammer. Its calculation, memory and recording functions allow for quick, easy and accurate test results (*Qualitest 2006*)

There are a variety of different Schmidt hammers from several companies with different levels of readouts and electronics involved that are all suitable and very practical for field use.

A.6 Guided Wave Ultrasonic

A.6.1 Fundamental Operating Principles

In ultrasonic testing (UT) high frequency sound waves in the range of 0.5 to 15 MHz and occasionally higher are used to characterize material, detect flaws and determine the thickness of a test object (*NDT 2009*). The two modes of propagation in UT are bulk wave and guided wave ultrasonic.

Bulk wave propagation, which includes longitudinal and transverse (shear) waves, refers to wave propagation in infinite media. Guided waves are those that require a boundary for their existence, most commonly consisting of surface waves, plate waves, and interface waves (*Rose 1999*). Surface (Rayleigh) waves are free waves on the surface of a semi-infinite solid. Plate (Lamb) waves are complex vibrational waves that travel through the entire thickness of a material (*NDT 2009*). Interface (Stonely) waves are free waves that occur at an interface between two media (*Rose 1999*). Two techniques for generating guided waves are shown in Figure A.12.
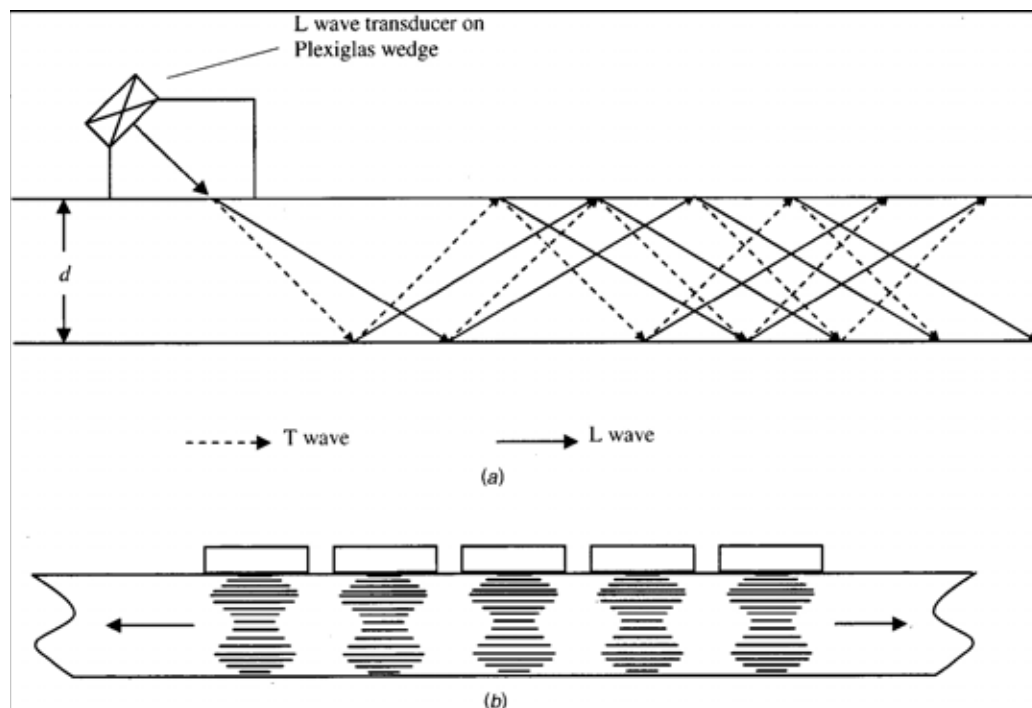

Figure A.12:   Techniques for the generation of guided waves: a) oblique incidence; b) combination transducer. Reproduced from Rose (*2002*).

Guided wave UT has been used in various media including bars, tubes, multiple layers, and anisotropic media. For Zn CP systems, the multiple layer medium would be the most practical.

> Guided waves in multiple layers can be used in a number of different practical situations. Examples include coating problems of plasma spray on a turbine blade, painted structures, aircraft multiple layers (either bonded or with sealant layers), diffusion bonded or adhesively bonded structures in general, and even ice or contaminant detection via multiple layers of solids and fluids (*Rose 1999*).

An example of a lab device using guided waves to inspect a lap joint is shown in Figure A.13.
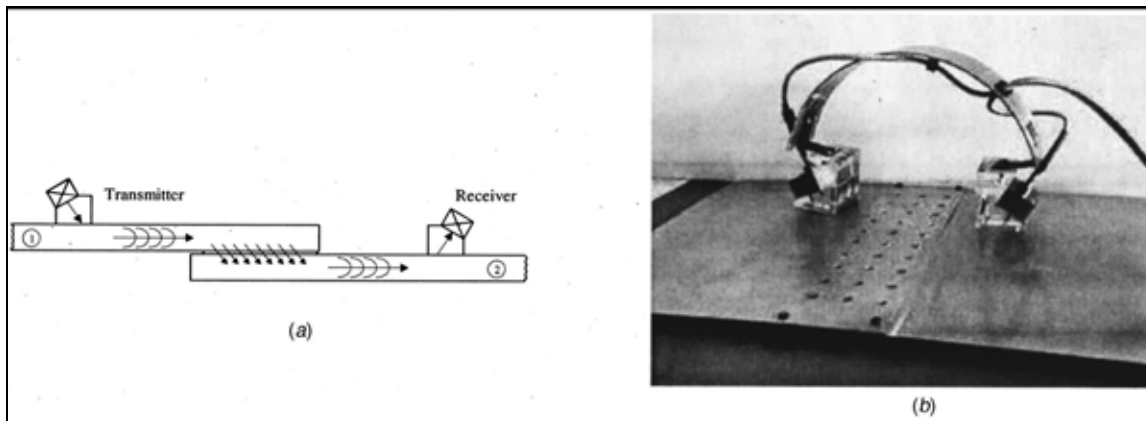
Figure A.13: **A lap splice inspection sample problem: a) ultrasonic through-transmission approach for lap splice joint inspection; b) double spring "hopping probe" used for the inspection of a lap splice joint. Reproduced from Rose (*2002*).**

One example of guided wave UT modeled in "Ultrasonic Waves in Solid Media" is a multilayer model for titanium diffusion bond inspection. In this model, the fine diffusion bonded interface can be viewed as a thin layer. Poor contact can be modeled as a distinct layer with modulus and density degradation values, which can determine excellent, intermediate, or poor diffusion bonding. Therefore dispersion curves for a perfect bond can be compared with degradation models (*Rose 1999*). Another application of guided wave analysis is in a containment structure, where steel is embedded in concrete. It becomes possible to send ultrasonic energy along the steel plate with minimal leakage into the concrete, allowing the ability to locate corrosion and cracking in the steel plate (*Rose 2002*).

Guided wave UT inspection may be able to detect both the growth of the oxide layer thickness and the consumption of the sprayed Zn anode. Additionally, it may be possible to infer the bond strength in a manner similar to the titanium diffusion bond model. The composition of each zone within the oxide layer creates a density gradient between zones. If

the density difference between each zone is sufficient, guided wave UT can distinguish between the individual zones. It can also detect delamination and potential defect areas, such as cracking in zone 1, (as observed in Figure 1.4). With this technique, it is possible to develop a correlation between the oxide layer growth, defects, thickness of each zone and Zn layer consumption to the CP anode lifespan.

A.6.2 Advantages and Disadvantages

Ultrasonic inspection is a very useful and versatile method of non-destructive testing (NDT). Some of the advantages of ultrasonic inspection include:

1. Superior penetrating power and depth compared to other NDT.
2. High sensitivity.
3. One surface needs to be accessible.
4. Ability to inspect structures under water, coatings, insulation, multi-layer structures or concrete with excellent sensitivity.
5. Greater accuracy than other NDT for determining depth of internal flaws and thickness of parts with parallel surfaces.
6. Minimal part preparation is required.
7. Electronic equipment provides instantaneous results.
8. Non-hazardous to operations or to nearby personnel, and has no effect on equipment and materials in the vicinity.
9. Can be portable or highly automated.
10. Cost effectiveness after training because of inspection simplicity and speed.

Some of the disadvantages or limitations of ultrasonic testing include:

1. Skill and training for manual operation is more extensive than with some other methods and may require experienced technicians.
2. Extensive technical knowledge is required for the development of inspection procedures.
3. A coupling medium is usually required to induce the transfer of sound energy into the test media.
4. Materials that are rough, irregular in shape, very small, exceptionally thin or not homogeneous are difficult to inspect.
5. Inspected items must be water resistant.
6. Reference standards are required for both equipment calibration and characterization of flaws.
7. Research and development time and cost would be high for the development of a functional measuring device and field procedure.

A.6.3 Commercially Available Devices

Innerspec Technologies has a variety of electromagnetic-acoustic transducers (EMAT) designed to generate Lamb waves within the material being investigated. One device from Innerspec is the temate® Thickness gage shown in Figure A.14. The temate is used mainly

for thickness measurements perpendicular to the material, but can also determine corrosion, flaw detection such as delaminations and disbands, acoustic velocity measurements and much more (*Innerspec Technologies 2006*).

Figure A.14: **The temate® Thickness Gage basic set and measure device, which provides a hand-held easy-to-use programmable digital interface (*Innerspec Technologies 2006*)**

Quality Network Inc. (Qnet) also has a variety of UT and EMAT equipment. The ISCAN 6, shown in Figure A.15, is a portable all-in-one X-Y scanner for manual or motorized data acquisition in ultrasonic and eddy current inspections. This device is a light-weight scanner useful in a large range of applications for aviation and aerospace, piping, tank shell, vessel and other field or laboratory applications (*Quality Network Inc. 2006*). Further information for the ISCAN 6 is below.
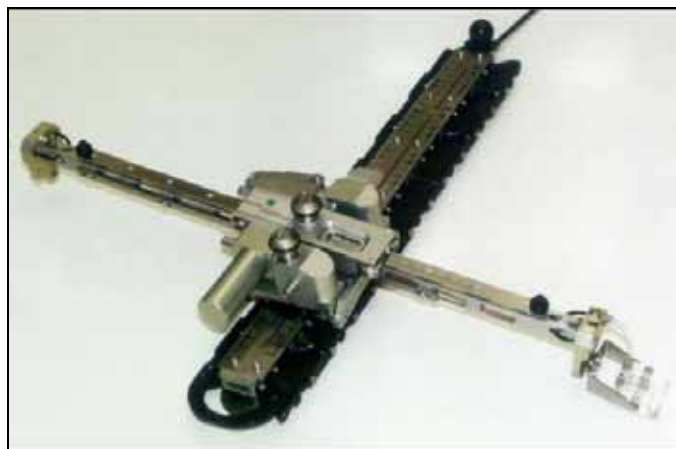
Figure A.15: **ISCAN 6 ultrasonic and eddy current X-Y scanner set up for a flat surface with suction cups to attach the tracks to the surface. Also available with magnetic or straps attachments (*Quality Network Inc. 2006*).**

Features at a Glance

The ISCAN-6 scanner is the first scanner to incorporate miniature 24V DC motors and encoders into an XY manual scanner. This unique capability allows three modes of scanning, XY manual, XY motorized, and XY hybrid. This new hybrid mode allows the operator to guide the transducer through the scan stroke by hand with quick motorized indexing at the end of each stroke. This scanning mode is useful when proper coupling can only be achieved by hand.

A very flexible system can be configured by adding ultrasonic hardware and software, such as the PCUS 10/11 ultrasonic cards and CPS™ or Winspect® data acquisition/analysis software. Eddy current inspections can also be performed by adding suitable (PC-based) eddy current components.

Scanner Characteristics

The scanner is suitable for automated and/or semi-automated scanning of flat or cylindrical components with diameters of 8" and larger.

Scanner tracks are available in lengths of 320mm (12.8") with a usable scanning length of 300mm (12"). Tracks can be delivered as magnetic tracks, suction-cup tracks, or strap-on stainless steel tracks. Scanner arms are available in lengths from 200mm to 500mm.

The motor/encoder/gear-box unit is splash proof.

Specifications:

- Motors:
  24 V, DC servo motors, 3.2W, 7250 RPM

- Encoders:
  Quadrature encoders, resolution 0.037mm/pulse for track (index) direction, 0.024mm/pulse for arm (scan) direction

- Material:
  Anodized aluminum construction

- Weight:
  approx. 2kg (4.4 lbs.)

- Dimensions:
  400 x 140 x 60mm (15.8" x 5.5"x 2.4") without track

Controller/Amplifier:

- Dimensions:
  130 x 100 x 60mm (5.1" x 3.9" x 2.4")

- Interface to Controller:
  Direct connection to the Galil DMC1700 series controller cable or any controller providing a +/-10V servo command signal

- Output:
  +/-24VDC @ 2A protected by current limiting (adjustable) and thermal shutdown

A.6.4 Possible Device Modifications

Further research and testing must be done to determine the best form of measurement and wave propagation for our specific process. Depending on these findings, the level of modification that needs to be made may vary greatly, ranging from little modification with proper calibration, to a highly modified version of the commercially available device.

A.7   Bond Strength

A.7.1 Fundamental Operating Principles

Bond strength testing measures the force required for delamination of the zinc anode layer from the concrete. The two main types of bond strength measurements in use today are the pull test and the scratch test.

Pull test bond strength measurements are already used in the field on the anodes to determine their approximate lifespan. This test is done by attaching an aluminum dolly to the zinc with epoxy to ensure a secure adhesion. Then the force required to delaminate the zinc from the Zn-concrete interface is measured.

The scratch test is currently the most commonly used method of assessing coating adhesion in thin films. A loaded stylus is traversed across the coated surface of a flat specimen with either constant or increasing load normal to the surface (*Osgerby, et al. 1998*). The load is analyzed until the critical load, or load magnitude that induces failure occurs. The vertical force applied to the indenter and the horizontal force required to move the indenter is recorded until the failure occurs (*Lanstaff 1998*).

A.7.2 Advantages and Disadvantages

The advantages of the bond strength measurements are that there is already a field procedure in place and commercially available devices that are being used for the pull testing method. Also achieving the bond strength to anode lifespan correlation is one of the main objectives of the project, and this provides a direct measurement without additional correlations.

The disadvantage to this method is that all direct bond strength measurements are destructive. For pull strength bond testing, the use of a smaller dolly would reduce the destructiveness of the test, but this would introduce a large amount of inconsistency in the measurement. Scratch testing is typically used on thin films (approximately 1 μm) and may not be applicable to the measurement of the zinc adhesive bond strength due to the thickness of the anode layer. Also for the scratch test method there are no commercially available field devices, so one would have to be fully developed.

A.7.3 Commercially Available Devices

The current pull test device used in the field by ODOT is the Proceq Adhesion Tester, shown in Figure A.16.

Figure A.16:   Proceq portable tester used to measure the bond strength of the Zn anode on concrete (*Covino, et al. 2002*)

There are many scratch test devices in a laboratory setting currently being used for many different adhesion applications. One of them is shown in Figure A.17. There are currently no field scratch test devices applicable to the zinc anode testing.

Figure A.17:   Nanovea Series Scratch Tester from Micro Photonics (*Micro Photonics 2006*)

A.8   pH Testing

In pH testing the hydrogen ion concentration (or more precisely, the activity) of a solution is determined. This test would be used to determine the hydrogen ion concentration level at the Zn anode-concrete interface. As the zinc-oxide layer forms, hydroxyl ions are consumed. Consequently the hydrogen ion concentration rises and the pH lowers.

Testing of pH has been performed on electrochemically aged blocks and documented in the NETL report (*Covino, et al. 2002*). These data suggest that the pH falls rapidly, but it stabilizes at a value around 7 well before the delamination period (1500-1800 [kC/m^2]) and closer to the max bond strength period (500- 600 [kC/m^2]), as shown in Figure 1.5. The stabilization of the pH makes it a poor choice to monitor anode bond strength, which would assist ODOT in planning anode repair and replacement, Therefore, pH testing is not considered further.


A.9   Resistance/Permeability Hybrid Technology

A.9.1 Fundamental Operating Principles

When a CP system is wetted, the voltage of a constant-current system decays to a minimum value and then increases, eventually approaching the initial value [1,2]. The minimum voltage that follows the wetting increases with age, as was shown in Figure A.3. Also the rate of decay appears to increase somewhat with age, as shown in Figure A.18, presumably due to the buildup of the oxide layer. The oxide layer consisted mainly of zone 2 and 3 when the decay curves depicted in the graph were obtained.
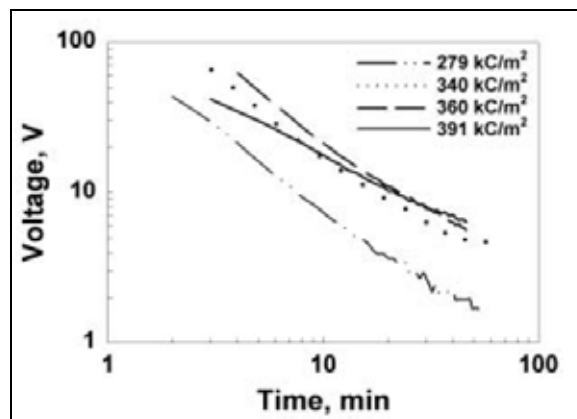
Figure A.18: CP system voltage decay due to wetting of the anode-concrete interface versus elapsed time after wetting for selected electrochemical ages. Reproduced from Covino, et al. (*2002*).
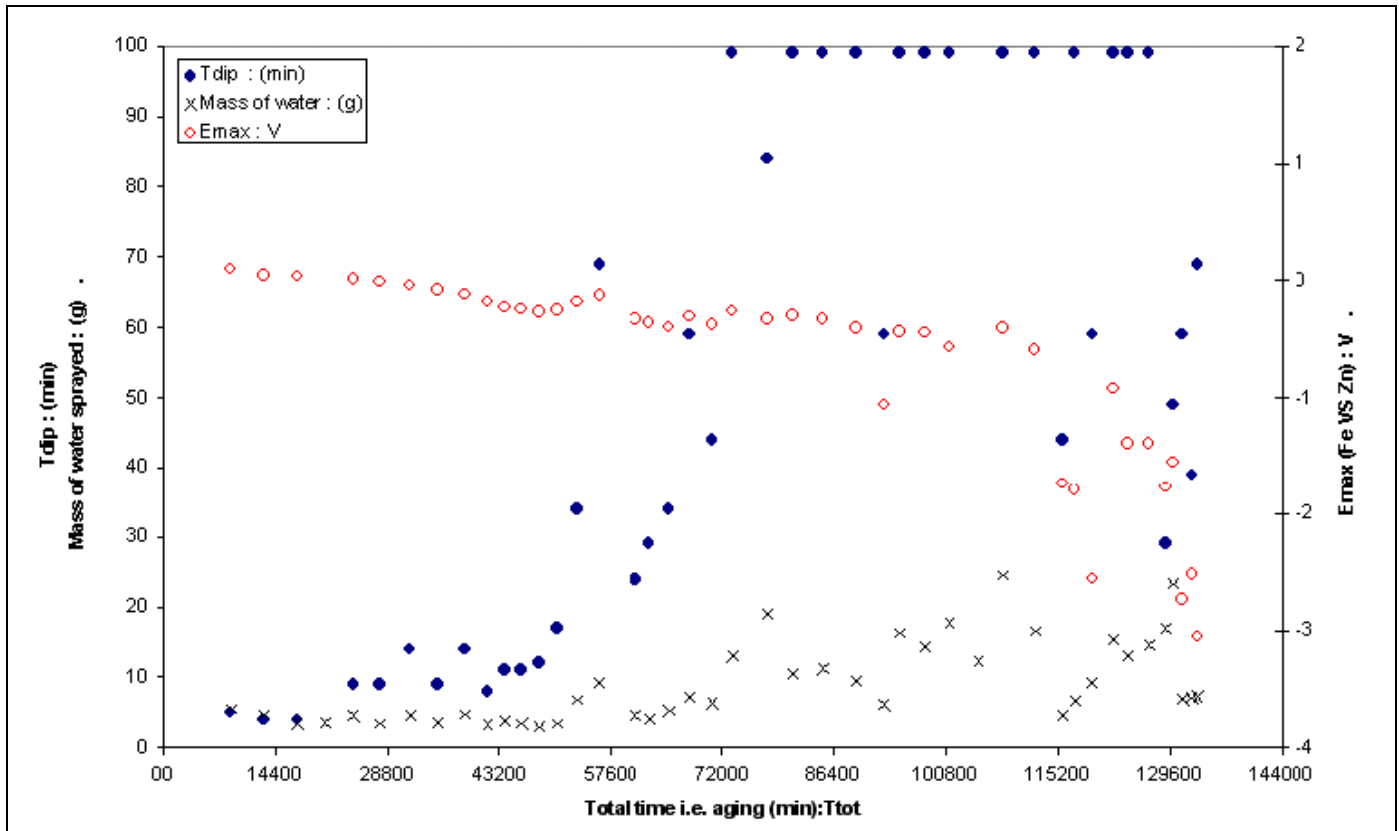
Figure A.19: T_{dip}, E_{max} and mass of water as a function of aging. Reproduced from Rehani (*2000*).

This trend of slower recovery with increasing electrochemical age is also seen in Figure A.19, which shows both E_{max} and the time between application of spray and the onset of the dip in the voltage, T_{dip}, as a function of electrochemical age (*Rehani 2000*).   Interestingly T_{dip} appears to increase as the amount of water present during the wetting increases, as shown in Figure A.20.   Because the interval between successive wettings (Figure A.20) was less than 3% of the lifespan of the test blocks, it can be assumed that the effect of aging over the course of these tests is insignificant (*Rehani 2000*).

a)
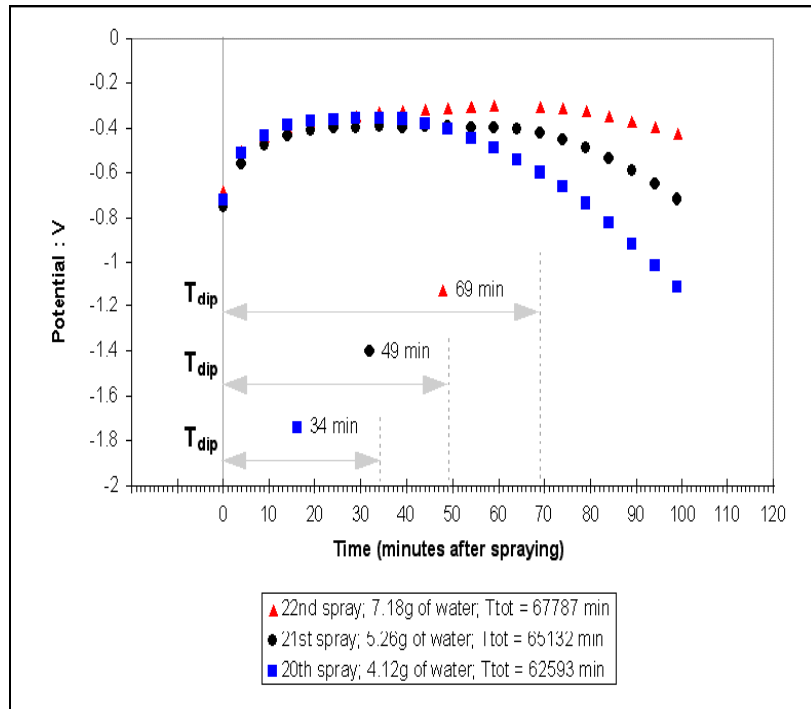
b)
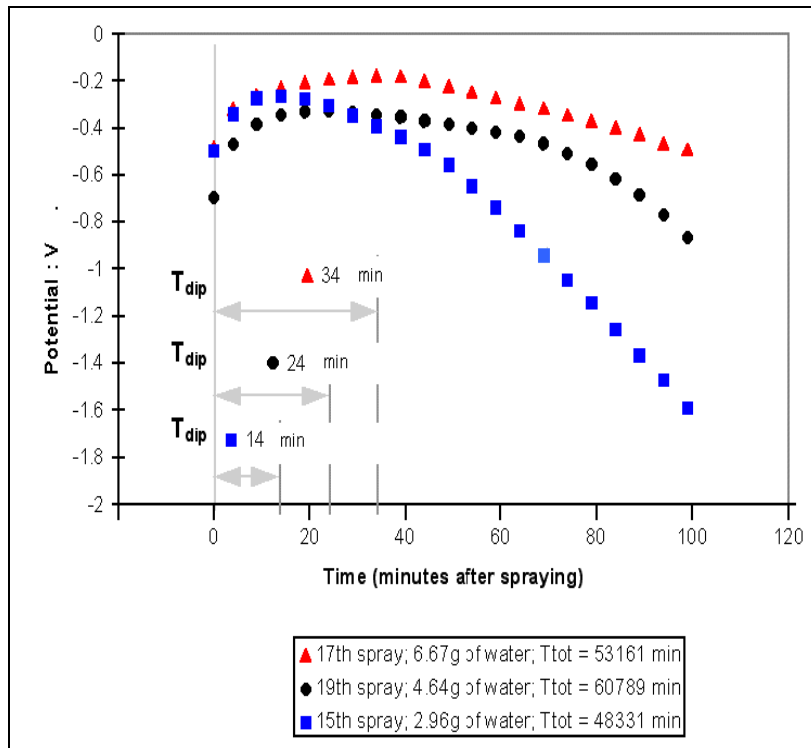
Figure A.20: Potential response with time and variation of T_{dip} for varying amounts of spray water at points close in aging: a) spray numbers 20, 21 and 22; b) Spray numbers 15, 17 and 19. Reproduced from Rehani (*2000*).

To help eliminate the effects of the water volume, a consistent finite amount of water would be applied to a specific area of the zinc anode. The electrical response to this application of water will be compiled and correlated to the anode condition. Electrical response can be measured in many different ways including: resistance, dynamic voltage, cyclic voltage application, and others. A combination of these measurements and the permeability of the fluid may be needed to develop a complete correlation of anode conditions, due to the range of interfacial chemistry and its effect on the electrical response.

Some disadvantages of this measurement technique in the field are the initial measuring conditions, and the time to maximum voltage. The possibility of the presence of water prior to the measurement being made will affect the initial values and electrical response to the finite amount of water applied. Also to be considered is the time to reach maximum voltage after wetting increases to times of over 100 minutes in later aging periods, which may exceed the desired time for each individual measurement.

A.9.2 Advantages and Disadvantages

Advantages:
1) Non-destructive
2) Fairly portable
3) Low cost of production
4) Low development time
5) Minor changes to commercial device

Disadvantages:
1) The need to tie into the rebar reinforcement for each zone
2) Need of a water source for wetting
3) Inconsistent initial measurement conditions
4) Long measurement times
5) Amount of water present affects measurements

A.9.3 Commercially Available Devices

This device would consist of a combination of commercially available devices used to measure resistance (section A.2) and voltage, with the water reservoir and volume displacement measuring apparatus. A device that is capable of acquiring the range of measurements needed is unavailable at this time.

APPENDIX B: MATHEMATICAL MODEL

APPENDIX B – MATHEMATICAL MODEL

```matlab
Reflection Two Film.m (Matlab Code)

clear all
clc

%n = input('Enter the number of mediums (3): ')

%if n==2

%    c1 = input('Speed of sound in medum 1 (c1): ')
%    p1 = input('Density of medium 1 (p1): ')
%    c2 = input('Speed of sound in medum 2 (c2): ')
%    p2 = input('Density of medium 2 (p2): ')

%elseif n==3

%    c1 = input('Speed of sound in medum 1 (c1): ')
%    p1 = input('Density of medium 1 (p1): ')
%    c2 = input('Speed of sound in medum 2 (c2): ')
%    p2 = input('Density of medium 2 (p2): ')
%    c3 = input('Speed of sound in medum 3 c(3): ')
%    p3 = input('Density of medium 3 (p3): ')

%else

%    c1 = input('Speed of sound in medum 1 (c1): ')
%    p1 = input('Density of medium 1 (p1): ')
%    c2 = input('Speed of sound in medum 2 (c2): ')
%    p2 = input('Density of medium 2 (p2): ')
%    c3 = input('Speed of sound in medum 3 c(3): ')
%    p3 = input('Density of medium 3 (p3): ')
%    c4 = input('Speed of sound in medum 3 (c4): ')
%    p4 = input('Density of medium 3 (p4): ')

%end

c1 = 4.35;       %Speed of sound of piezo crystals
c2 = 3.85;       %Speed of sound of zinc
c3 = 3.00;       %Speed of sound of zinc oxide
c4 = 3.40;       %Speed of sound of piezo concrete

p1 = 7.80;       %Density of piezo crystals
p2 = 7.14;       %Density of zinc
p3 = 5.60;       %Density of zinc osice
p4 = 2.30;       %Density of concrete

D12 = (p2*c2 - p1*c1)/(p2*c2 + p1*c1);
D23 = (p3*c3 - p2*c2)/(p3*c3 + p2*c2);
D34 = (p4*c4 - p3*c3)/(p4*c4 + p3*c3);



%d3 = 0.5-d2
```

```matlab
 w = 100;          %Angular fequency
%d2=1
%y= [0:0.5/29:0.5]
for d2 = 1:31;
    for d3 = 1:31;

        k2 = w/c2;        %Wave Number media 2
        k3 = w/c3;        %Wave Number media 3

        e2 = exp(i*k2.*((d2-1)*0.4/30));
        e3 = exp(i*k3.*((d3-1)*0.4/30));

        Rn = D34*e3.*(e2+(D12*D23./e2))+1./e3.*(D23*e2+D12./e2);
%Numerator portion of the Reflection coefficient
        Rd = D34*e3.*(D12*e2+D23./e2)+1./e3.*(1./e2+D12*D23.*e2);
%Denominator portion of the Reflection coefficient
        R = Rn./Rd;
        Output = [d2/100 d3/100 R];
        k = d3 + (d2 - 1) * 31;

        Output1(k,:) = [Output];

        Output2(d2,d3) = R;

    end

end

x=Output1(:,1);
y=Output1(:,2);
z=abs(Output1(:,3));
Output2;

figure(1);
surfl(abs(Output2));
shading interp
colormap(gray);

figure(2);

plot(abs(Output2(2,:)))
a = [1;2;3];
b = [1;2;3];
c = [2;3;2]
```